Characterization of $Be_xZn_{1-x}O$ Thin Films Grown by Pulsed Laser Deposition

Thomas,
Peltier 116121

August 22, 2013

Contents

1 Introduction **3**
1.1 Introduction 4
1.2 Introduction to wide-gap materials 4
1.3 Beryllia: a wide gap insulator 10
1.4 BeZnO: a tunable band gap semiconductor 10
1.5 Purpose of research 15

2 Film growth and characterization methods **17**
2.1 Introduction 18
2.2 Growth set-up and conditions 18
2.2.1 Introduction 18
2.2.2 Pulsed laser deposition system 19
2.2.3 Experimental deposition conditions 21
2.3 Structural and morphology analysis 28
2.3.1 X-ray diffraction 28
2.3.2 Film thickness measurement 29
2.3.3 AFM 29
2.3.4 Plume characterization 29
2.4 Optical and electrical measurement 32
2.4.1 Pyroelectric characterization 32
2.4.2 Reflectivity and transmission measurement 33
2.4.3 Photocurrent measurement 36
2.4.4 High-temperature resistivity measurement 45

3 BeO growth stability **47**
3.1 Introduction 48
3.2 BeO growth optimization 48
3.3 X-ray diffraction analysis 49

3.3.1 Pole figure . . . 55
3.4 Morphology . . . 56
3.5 Growth rate . . . 56
3.6 Plume dynamics . . . 59
3.7 Discussion . . . 63
3.7.1 Room temperature growth . . . 63
3.7.2 BeO growth instability . . . 64
3.8 Pyroelectric measurement . . . 65

4 Band gap tuning by alloying BeO and ZnO 70
4.1 Introduction . . . 71
4.2 Crystallinity and Be content . . . 71
4.2.1 Determination of the concentration . . . 71
4.2.2 Crystal structure . . . 76
4.3 Morphology evolution . . . 83
4.4 Band gap measurement . . . 86

5 Band gap evolution and defects investigations 92
5.1 Introduction . . . 93
5.2 Wavelength dependence of photocurrent . . . 93
5.3 Defect distribution . . . 96
5.3.1 Photocarrier lifetime . . . 96
5.3.2 Trap level distribution . . . 100
5.4 Temperature effect . . . 101

6 Conclusion 103

Acknowledgment 105

List of figures 106

Bibliography 111

Chapter 1

Introduction

1.1 Introduction

Wide-gap semiconductors are used in various optoelectronic, high power and high temperature applications. In optoelectronics, the operating wavelength of light sensors and emitters is determined by the band gap of the semiconductor. New wide-gap semiconductors have therefore brought us blue light-emitting diodes and white-light solid-state illumination.

In high-power and high-voltage switching applications, it is necessary to maximize the on-off ratio and the switching speed of field-effect transistors. Since the intrinsic carrier density in a semiconductor is a function of temperature and the width of the energy gap, there is an advantage in using wide-gap materials in power electronics to reduce leak currents at high operating temperatures. The breakdown fields of wide-gap semiconductors are higher than for silicon, offering another advantage for operating devices at high voltages. The most popular wide-gap semiconductors currently used in power applications are SiC and GaN that have band gaps of 3.27 eV and 3.26 eV[1], respectively.[1]

Wide-gap semiconductors are of prime interest for applications in extreme operating conditions, such as at high temperature. The fields of use include the aerospace industry and deep drilling for oil and gas exploration.

Wide-gap materials with low atomic weight have additional potential advantages in environments with high radiation loads, such as in medical imaging, satellites and deep-space probes, and high-energy physics. The radiation damage in a material is directly proportional to the interaction cross-section with a given type of radiation. In general, low atomic mass materials have lower cross-sections (Table1.1) and thus also suffer less radiation damage under heavy radiation loads.

1.2 Introduction to wide-gap materials

Modern microelectronics is based on semiconductors, mainly Silicon. The key characteristic of semiconductors is the presence of a band gap between the valence band and the conduction band. In an intrinsic semiconductor, no electron levels are present in this energy gap and the material would be insulating under normal operating conditions. As opposed to wide-gap insulators, the conductivity in a wide-gap semiconductor can be changed by impurity doping, which introduces electrons to the conduction band, producing an n-type material. The transport proprieties of n-type semiconductors are determined by the number of electrons

[1]in the 4H-SiC compound

Material	Atomic number	Cross section (barn)
Be	4	$8.5 * 10^3$
C	6	$4.4 * 10^4$
N	7	$7.9 * 10^4$
O	8	$1.2 * 10^5$
Si	14	$7.5 * 10^4$
Zn	30	$1.7 * 10^5$
Ga	31	$2.1 * 10^5$

Table 1.1: X-ray cross sections at the energy E=1keV [2]

in the conduction band. The conduction band shape determines the maximum mobility of the conduction electrons(Tab.1.2), although in most practical systems impurity scattering sets a limit on electron mobility. In practice, the carrier mobility in wide gap materials can be as high as in most 'narrow-gap' semiconductors, such as Si or GaAs.

Material	Band gap(eV)	Mobility(cm^{-2})/Vs	n-type dopant	p-type dopant
Si	1.12	1350	P	B
GaAs	1.4	8500	Si	C/Be
SiC	2.26	720	N on C site	Al on Si site
GaN	3.27	1000	Si on Ga site	Mg on Ga site
Diamond	5.47	1000	N	B

Table 1.2: Band gap, mobility and usual dopant for the main wide bang gap semiconductors.

For most electronic devices, such as field-effect transistors (FET), the conductivity of the semiconductor is changed by altering the concentration of electrons in an active layer by, for example, applying an external electric field. In a typical FET, an applied bias voltage applied on a gate capacitor structure results in an accumulation of charge in the transistor channel region, shifting the Fermi level toward either the conduction or valence band. The electron density in the conduction band can thus be controlled by adjusting the gate bias.

Other extrinsic interactions can also affect the concentration of carriers in the conduction band of a semiconductor. The most common external parameter is

temperature and semiconductor devices therefore always have a maximum operating temperature limit. Another factor that can generate additional carriers is light exposure. Visible light exposure can be prevented by suitable device packaging, but it is impossible to shield electronic components from higher-energy photons, such as x-rays or gamma-rays. A less common problem, mostly limited to space and high-energy physics and nuclear industry applications, is the additional charge generated by high-energy particles.

The carrier concentration in the conduction band is in thermal equilibrium with the valence band. This equilibrium can be expressed as

$$np \propto \exp\left(-\frac{E_{\mathrm{g}}}{k_{\mathrm{B}}T}\right), \tag{1.1}$$

where n and p are the electron and hole concentrations, respectively, E_{g} is the band gap, T is the semiconductor temperature and k_{B} the Boltzmann constant.[3]

In an intrinsic semiconductor, the carrier concentration depends only on the temperature and the band-gap energy. If the temperature is high enough, a significant number of electrons can be thermally excited to the conduction band. In a switching device, this may lead to a permanently 'on' device, where the tuning of the carrier concentration by an applied bias becomes impossible due to the reduced effective on-off ratio. A wider band gap reduces the concentration of thermal carriers. The development of a tunable wide band gap semiconductor is thus a key to constructing transistors or other devices that can operate at temperatures above 300°C.[2]

If a photon has an energy higher than the band gap of a semiconductor, it can be absorbed. The absorption process results in the excitation of an electron from the valence band to the conduction band. A detailed description of the process is discussed in Section 2.4.

A high-energy particle traversing a semiconductor or an insulator loses energy gradually due to elastic collisions with electrons. These collisions result in carrier generation, similar to the photon absorption process discussed earlier. Bohr, Bethe, Bloch, and Landau have developed a theory to describe the process.[4] The energy loss of a particle traveling in a medium is given by

$$\frac{dE}{dx} = 2\pi N_0 r_{\mathrm{e}}^2 m_{\mathrm{e}}^2 c^2 \rho \frac{Z}{A}\frac{z^2}{\beta^2}\left[\ln\left(\frac{2m_{\mathrm{e}}\gamma^2 v^2 W_{\mathrm{max}}}{I^2}\right) - 2\beta^2 - \delta - 2\frac{C}{Z}\right], \tag{1.2}$$

[2] 300°C is the usual temperature limit for commercially available high-temperature transistors based on SiC.

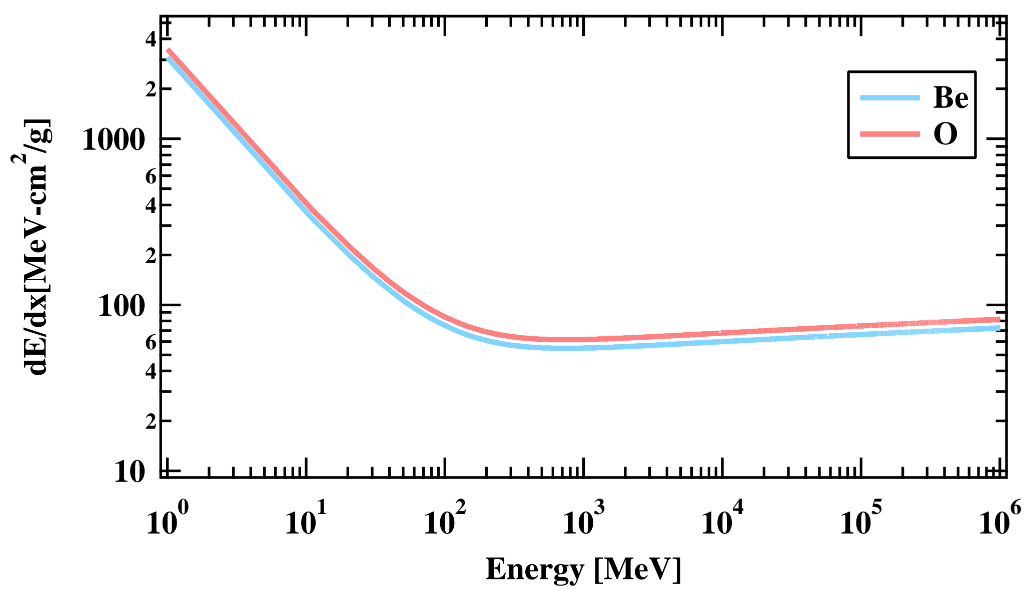

Figure 1.1: Rate of energy loss due to ionization as a function of kinetic energy of a charged particle for Beryllium and Oxygen.

where x is the path length, r_e and m_e are the electron radius and mass, N_0 is Avogadro's number, I is the effective ionization potential over all electrons, Z and A are the the atomic number and mass of the medium, ρ is the density, z is the charge of the particle, $\beta = \frac{v}{c}$ is the relativistic velocity of the particle, $\gamma = \frac{1}{\sqrt{1-\beta^2}}$, δ is a density of correction, C is a shell correction, and W_{max} is the maximum energy transfer in a single collision.

For a non-relativistic particle with a sufficiently low velocity, the energy loss decreases with energy. The minimum loss corresponds to an increase of dissipation due to relativistic effects. The saturation at high-energies results from the polarization of the medium. The rate of energy loss depends on severals parameters, such as the atomic number of the medium and the kinetics energy of the particle (Figure 1.2). For semiconductors, the energy loss necessary for the creation of a electron-hole pair is greater than the band gap. Table 1.3 Indeed, part of the energy lost by a particle is converted to thermal energy and optical phonons[5].

Material	Band gap(eV)	Electron-hole pair creation energy (eV)
Si	1.12	3.625 [6]
C(diamond)	5.47	12 [7]
BeO	10.6	25 [8]
ZnO	3.37	9(theo.) [9]

Table 1.3: Band gap and electron-hole pair creation energy for different materials.

The electron-hole pair generation process is used in particle detectors. A solid state particle detector typically consists of a thin semiconductor sheet between two electrodes. A large applied bias results in a strong electric field inside the semiconductor. A high-energy particle passing through the semiconductor generates electron-hole pairs that are separated by the electric field and the charge is collected at the detector electrodes. The absorption event is then detected as a current pulse in the external circuit.

The choice of the particle detector material is a balance between several incompatible goals. A higher atomic mass material generally results in a larger number of electron-holes pairs for a given particle energy and path length, but also results in larger structural damage. For large-area detectors, it is also important to have semiconductor crystals of sufficient size and with low intrinsic defect density.

In Large Hardon Collider (LHC), for example, two of the main detectors are

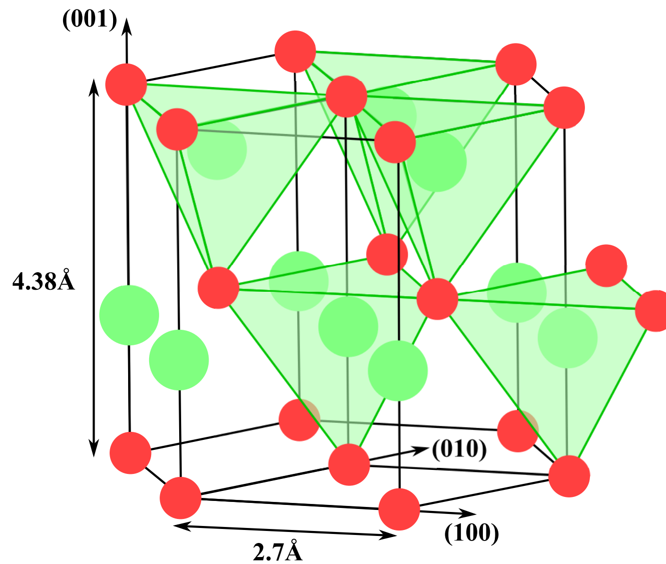

Figure 1.2: Structure of wurtzite BeO. Red atoms are oxygens. Beryllium atoms are shown in green.

silicon based (ATLAS and ALICE). Silicon was selected due to its extensive use in the industry. However, it is not the optimal material for particle detection due to its poor radiation hardness. Although the detection is efficient because of the low electron-hole pair creation energy and high carrier mobility, the low radiation damage threshold is an important factor that limits the lifetime of the device. Therefore, the best material for particle detection should have a lower average atomic number, an intermediate electron-hole pair creation energy, high carrier mobility, and a wide energy gap. Beryllium based semiconductors are therefore potentially useful for detector applications. Beryllium has a very low atomic mass and beryllia compounds have low densities. Since the bandgap of BeO is very large (10.6 eV), it is reasonable to expect to be able to find suitable semiconducting alloy phases with optimal band gaps of around 5 eV, while also offering better radiation hardness than silicon.

1.3 Beryllia: a wide gap insulator

Beryllium oxide is mainly used in the form of bulk ceramic in the nuclear and aerospace industries, but also in microwave electronics. Beryllium atoms have a very low interaction cross-section with all types of ionizing radiation, which makes it less sensitive to radiation damage. The high melting point of 2507°C allows applications in extreme conditions. Beryllia is used as an insulating heat sink material for high-power devices because of its high thermal conductivity and low bulk conductivity. The excellent insulating behavior of beryllia is due to the very large band gap of about $E_{\mathrm{g}} = 10.585$ eV.[10] Most first-principles calculations underestimate the band gap of BeO by several eV [11]. Figures 1.3 and 1.4 present the band structures of BeO and the more familiar ZnO. Both materials have the same wurtzite structure, albeit very different lattice parameters. The efficient thermal conductivity of BeO is caused by the very high energy of phonons as the Debye temperature is $\theta_{\mathrm{D}} = 1270$K.[12] In this aspect, BeO is similar to diamond, although much cheaper as a bulk ceramic.

Bulk BeO has the wurtzite structure (Fig. 1.2) with a cell parameters of $a = 2.698$ Å and $c = 4.3772$ Å. The low diffusion rate of oxygen in BeO is useful in applications of thin BeO layers as oxygen barriers in field-effect transistors (FETs). [15] Figure 1.3 shows a schematic representation of a metal-oxide-semiconductor (MOS) structure with different oxygen barrier layers. BeO has been shown to be more efficient in this application than Al_2O_3. The electrical proprieties, such as resistance, are difficult to probe even in thin films due to the very high resistivity.

1.4 BeZnO: a tunable band gap semiconductor

The possibility of adjusting the band gap between 3.2 eV and 10.6 eV as a function of Be substitution in $Be_xZn_{1-x}O$ has raised a lot of interest.

The Phillips ionicity[16] model can be used to predict the energy band gap of a binary compound. In this model, the band gap is given by $E_{\mathrm{g}}^2 = E_{\mathrm{h}}^2 + C^2$, where C is the ionic contribution and E_{h} is the covalent contribution. The relative ionic and covalent contributions can be estimated from the difference of electronegativities of the atoms. A larger difference of electronegativities indicates a stronger ionic bond. In all the oxide and nitride alloys discussed here, the bonding nature is mainly ionic due to the large value of electronegativities for oxygen and nitrogen. The variation from one cation to another is rather small and does not change the

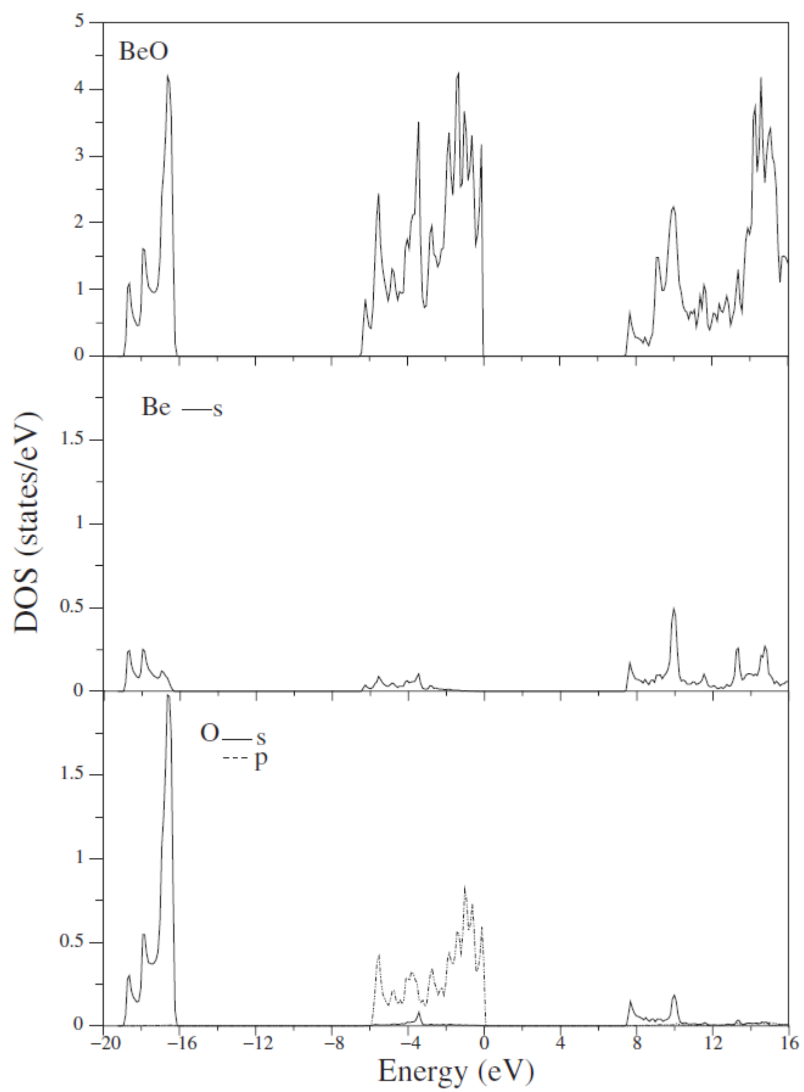

Figure 1.3: Band gap structure and density of states of BeO.[13]

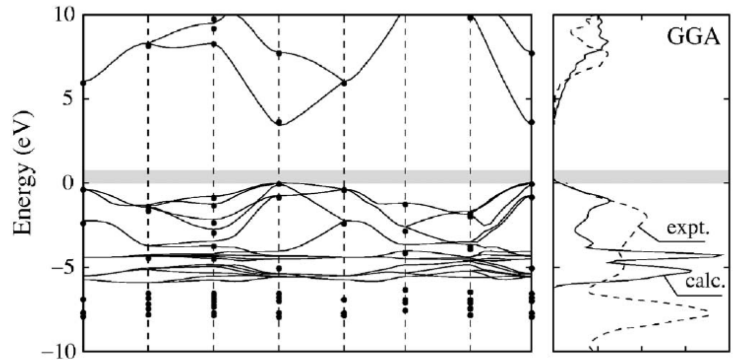

Figure 1.4: Band structure of ZnO.[14]

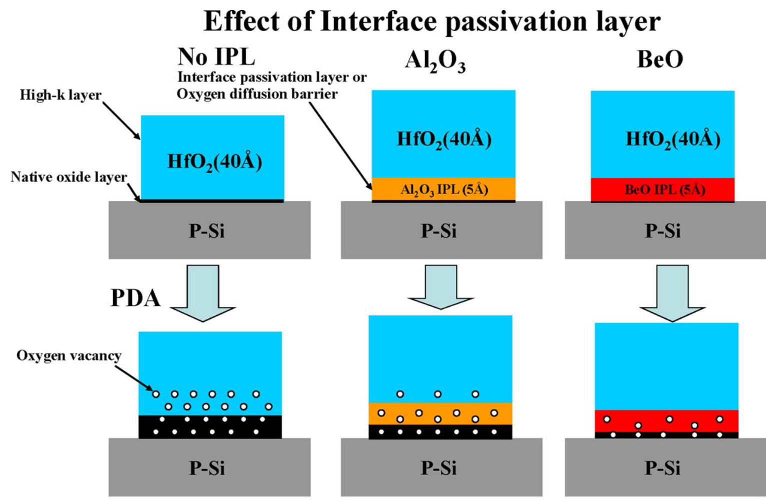

Figure 1.5: Schematic MOS structures with oxygen diffusion barriers.[15]

nature of the bonding. Therefore, the band gap should be mainly determine by the ionic contribution C. Phillips has derived a general expression for a binary compound AB

$$C(\mathrm{AB}) = b[Z_\mathrm{A}/r_\mathrm{A} - Z_\mathrm{B}/r_\mathrm{B}]e^{-k_\mathrm{s}R}, \tag{1.3}$$

where Z_A and Z_B are the valence numbers of the cation and the anion, r_A and r_B are the atomic radii defined by the half-distance of the bond length, R is the average cation and anion radius, and k_s is the Thomas-Fermi screening wave number. It appears that the band gap should be strongly affected by the bond length, which can be estimated from the ionic radii. In a given compound, e.g., ZnO, the band gap should be more strongly affected by the substitution of smaller cations at the Zn site. In case of nitrides, for example, it has been observed that compounds with increasing cation radii show an increase of band gaps: $E_\mathrm{g}(\mathrm{InN}) = 1.9\mathrm{eV} <$ $E_\mathrm{g}(\mathrm{GaN}) = 3.46\mathrm{eV} <$ $E_\mathrm{g}(\mathrm{AlN}) = 6.2\mathrm{eV}$.

For practical applications, BeO has to be alloyed with other materials in order to tune its proprieties. A better conductivity coupled with a wide bang gap is the goal of the alloy studies in this work. A good candidate is ZnO as it has the same wurtzite crystal structure. the band gap of ZnO is 3.3 eV and it is attractive for band gap tuning due to the proposed use of ZnO in light emitting and ultraviolet sensing applications.[18] A wide band gap material with reasonably high mobility would be perfect for use in particle detectors in extreme environments.

BeO and ZnO alloying has been reported recently by Ryu et al.[19] These authors claim that the whole range of alloying is possible and that the alloy phases follow Vegard's law, indicating that the alloying is substitutional. The band gap appeared to be tunable between 3.3 eV and 10.6 eV as a function of the Be/Zn ratio.

In contrast to the experimental report, first-principles calculation by density functional theory have predicted that only some compositions in the alloy phase diagram should be meta-stable, implying that BeO and ZnO should normally have rather low solubility limits.[20]

Later publications have shown that even when alloy phases are obtained, the alloying is coupled with a strong decrease of crystal quality as the Be content is increased.[21] The band gap shift has also been observed in amorphous films.[22] A mobility of about $6\mathrm{cm}^{-2}$/Vs has been reported for the BeZnO alloy phase. [23]

Figure 1.7 shows a schematic view of the alloying between ZnO and BeO. From the ZnO end, the Zinc atoms are progressively substituted by the Beryllium atoms. As the substitution level increases, the unit cell of the crystal decreases and the band gap increases from 3.37 eV to 10.6 eV. The alloying of II-IV

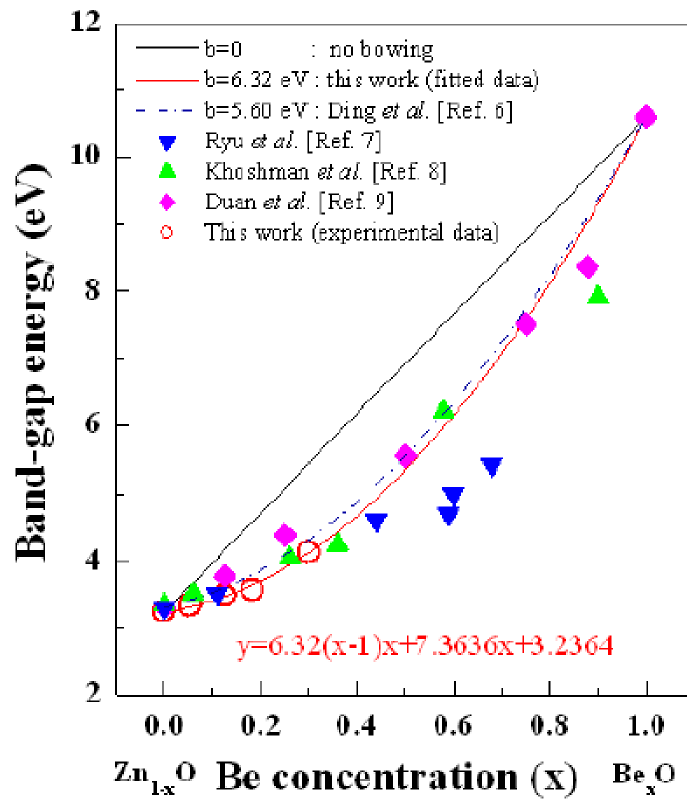

Figure 1.6: Evolution of the band gap as a function of beryllium content in $Be_xZn_{1-x}O$.[17]

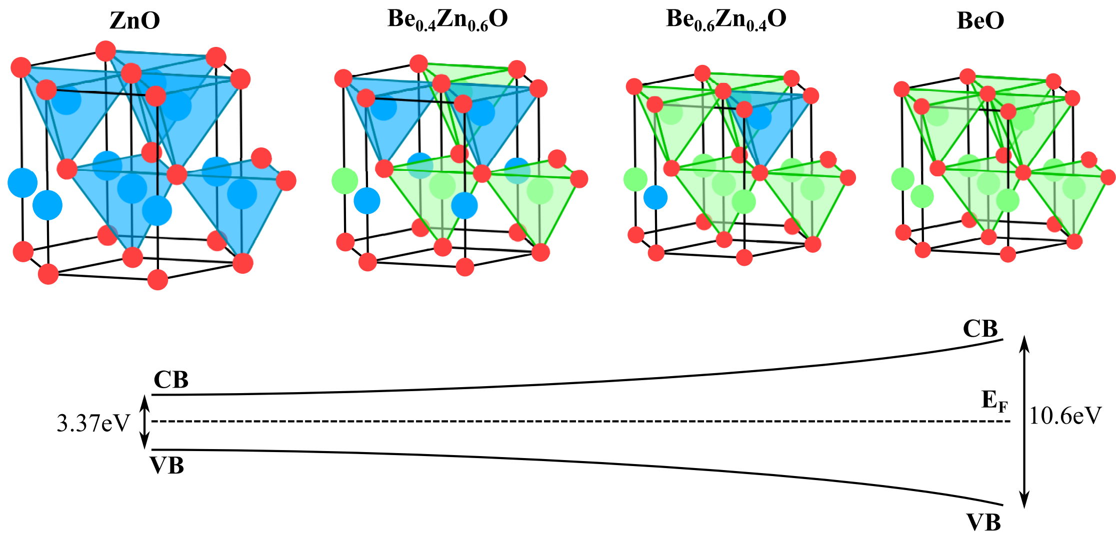

Figure 1.7: Substitutional alloying of BeO and ZnO assuming that the wurtzite structure is maintained.

or III-V semiconductor have been extensively studied from the point of view of band gap engineering. The reasons for alloying or non-alloying have also been widely investigated.[24] In the wurtzitic nitride family of GaN, InN, and AlN, alloying over the whole composition space has been reported for $Al_xGa_{1-x}N$ [25] and $In_xGa_{1-x}N$. The isostructural lattices and similar cation sizes have been suggested to enale the full range of alloys.

Alloying of ZnO has also been tried with MgO(cubic), BeO(wurtzite), and CdO(cubic). The solid solution limits have been shown to be quite low in those compounds: 15% for Mg, 13% for Be and 7% for Cd. For the alloying with CdO and MgO, the different crystal structure gives a plausible explanation for the low solubility. The low solubility of BeO has been attributed to the large ionic radius difference between Zn^{2+} (0.60Å) and Be^{2+} (0.27Å).

1.5 Purpose of research

A strong motivation for research is the desire to challenge the assumed limits set by existing technologies or the available knowledge. The limits of understanding are often set by our limited ability to see and to detect and it is for this reason that I

am interested in developing new materials that may find use in extreme conditions, specifically in the extremely high radiation-load environments of elementary particle detectors.

An important challenge is the measurement of physical phenomena in extreme environments, at high temperatures, in the presence of intense radiation, etc. Indeed, most of the electronics available today do not work long in such environments. New materials and technologies are therefore needed to enable us to see new physics.

Especially for optoelectronic and detector applications, a material where the band gap can be adjusted by alloying has great advantages. In this work, the focus is on thin film alloys of BeO ($E_{\mathrm{g}} = 10.585$ eV) and ZnO ($E_{\mathrm{g}} = 3.37$ eV), grown by Pulsed Laser Deposition (PLD) on sapphire substrates. The interest in this alloy system stems from earlier reports of BeZnO growth covering the full Be composition range[19] while theoretical calculations predict that only some compositions should be structurally stable.[20] The purpose in this thesis work is to determine the alloying limits for BeO in ZnO for thin films grown by PLD and obtain further characterization data on the alloy films.

Chapter 2

Film growth and characterization methods

2.1 Introduction

This chapter provides an overview of the experimental techniques of sample growth and characterization. Pulsed Laser Deposition (PLD) was used for growing the thin films. A profilometer was used to determine the film thickness and calibrate the film growth rate. The film crystallinity was probed by X-ray Diffraction (XRD). The BeO film crystal polarity was verified by measuring the pyroelectric response. The band gap energies were determined from either optical transmission spectra or reflectivity spectra and compared with the wavelength dependent yield of photoconductivity. The defects characteristics were investigated using time-dependent photocurrent relaxation measurements and by analyzing the high-temperature resistivity behavior up to 700°C.

2.2 Growth set-up and conditions

2.2.1 Introduction

The choice of a growth technique sets the limits for the material quality and the range of materials phases that can be fabricated. In general, the best crystal quality in thin films can be achieved using Molecular Beam Epitaxy (MBE), but at a significant cost penalty when compared to PLD. For instance, the record for carrier mobility in ZnO has been obtained using MBE growth of thin films. A high mobility value is a good indication of a very low defect density in the crystal and the mobilities obtained in MBE-grown ZnO films are not only several order of magnitude higher than for the best PLD-grown films but also better than bulk crystals[26].

It is therefore useful to consider the advantages and disadvantages of the experimental techniques used in this work in order to have a better understanding of the proprieties of the grown materials. The main advantages of PLD are the low cost of the deposition system, the ability to grow almost any oxide material in the same deposition chamber, and the possibility of growing metastable material phases. Nevertheless, the PLD technique also has a serious drawback - the density of point defects in the film is usually higher than for bulk crystals due to the high kinetic energy of the ablated atoms.

2.2.2 Pulsed laser deposition system

As the name suggests, Pulsed Laser Deposition constitutes vaporizing material from a solid target in vacuum and allowing the vapor that is formed to condense on the surface of a suitable substrate. The method is commonly used to grow thin films for research purposes, although there are also some applications of this technique in industry, such as the fabrication of high-temperature superconductor tapes.

Similar to other physical vapor deposition techniques, the vaporization occurs in a vacuum chamber, possibly in the presence of a background gas, such as oxygen. The pressure of the background oxygen gas determines the oxygen stoichiometry of the film and the oxidation kinetics during growth. As will be discussed in Section 3.7.2, the growth kinetics has a large effect on the desired crystalline phase formation for BeO films.

The pressure control in the deposition chamber was achieved by a combination of rotary and turbine pumps. Rough vacuum was obtained with a conventional rotary oil pump that has a base pressure of about 1 mTorr or a dry scroll pump with a base pressure of about 40 mTorr. The rotary pump was coupled with a turbomolecular pump that brought the chamber pressure down to at least 10^{-8} Torr. The main difference between the rotary pump and the turbo pump is that the former can pump a large volume of gas but cannot reach high vacuum levels due to the evaporation of pump oil. The latter can only pump a small volume of gas but can reach high vacuum conditions. The deposition system used in this work was composed of a loading chamber and the main deposition chamber. The base pressure of both chambers was kept at about 4×10^{-8} Torr. The pressure monitoring was done with a crystal gauge for high pressures and an ion gauge for pressures below 1 mTorr. During deposition, the chamber was filled with high-purity oxygen or N_2O gas in order to obtain an oxidizing environment. As shown in Figure 2.1, the target was scanned using an X-Y stage. This scanning was done in order to erode the whole target surface evenly and avoid damaging the target surface by ablating a single spot repeatedly. This improved the lifetime of the target and prevented the target stoichiometry from varying. The target was ablated with a KrF excimer laser at an emission wavelength of $\lambda = 248$ nm. The ablation process is quite complicated, combining purely electronic excitations on the picoseconde scale, followed by thermal evaporation on the nanosecond scale, and plasma plume expansion on the microsecond scale. The pulse length of the excimer laser was on the order of 20 ns.

The type of the excimer laser was carefully chosen because the wide band

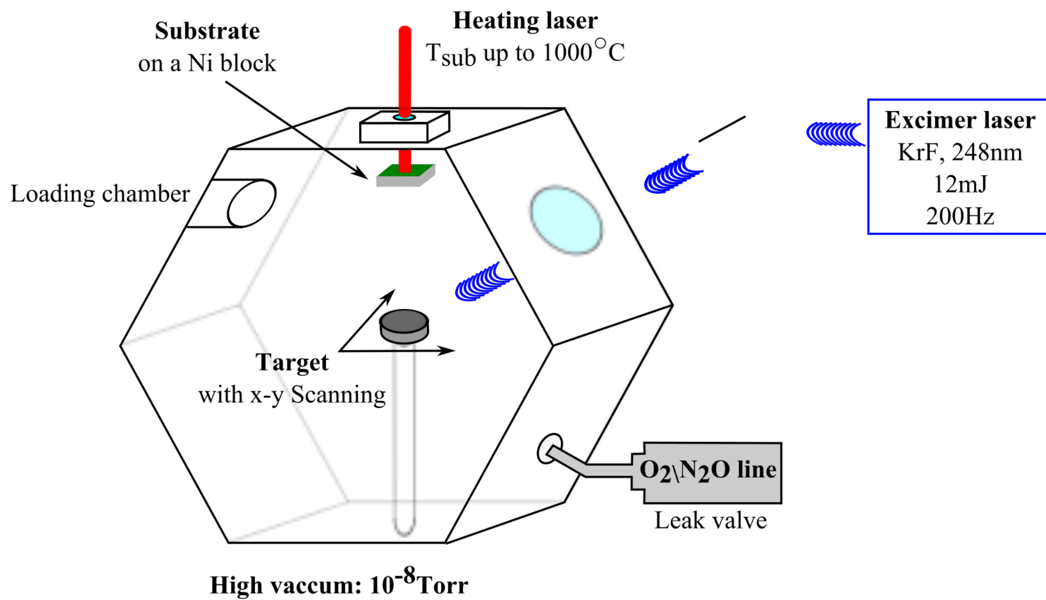

Figure 2.1: Schematic diagram of the micro-PLD chamber.

gap of BeO was expected to make the ablation process less efficient. Indeed, the wavelength of the ablation laser should normally exceed the band gap of the material that is ablated, ensuring efficient absorption of laser light in the surface layer of the target. This condition is met for many common oxides due to the 248 nm wavelength of the laser, which corresponds to a photon energy of 5 eV. However, for BeO, with a bulk band gap of 10.6 eV, it is difficult to meet this requirement. Therefore, a BraggStar excimer laser (200 Hz, 12 mJ) was chosen that has very high brilliance and a fast pulse risetime, increasing the rate of multi-photon excitations and leading to efficient ablation of wide-gap target materials.

The substrate temperature was controlled using a high-power diode laser with a pyrometer temperature feedback. The deposition substrates were mounted to face the plume generated by the ablation of the target.

The substrate temperature is an important process parameter that determines the diffusion length of adatoms brought to the film surface by the ablation plume. Higher substrate temperatures thus promote growth of crystalline phases, but also increase the likelihood of re-evaporation of atoms from the crystal surface.

2.2.3 Experimental deposition conditions

Substrate

The substrate material and crystal orientation were selected to ease the growth of the desired phase of the film. Having similar crystal structures for the desired film phase and the substrate is favorable for obtaining epitaxial growth. A different unit cell symmetry between the substrate and the film is generally energetically unfavorable and would lead to three-dimensional growth and low film crystallinity. In the first monolayers of the film, the film unit cell tends to be strained to fit the substrate. Bulk-like behavior is observed only after several monolayers. The difference of lattice parameters between the substrate and the film should generally be kept as small as possible. The mismatch is usually expressed as M(%) $= 100*(a_{\text{substrate}} - a_{\text{film}})/a_{\text{substrate}}$. A value close to zero limits the strain effect and promotes two-dimensional growth. Strong mismatch can lead to either a highly strained film or it may be impossible to stabilize a crystalline phase at all, resulting in non-crystalline growth. The crystal symmetry also has a strong influence on the stabilization of the film phase. In case of complex oxides with many different cation species, phase segregation may also depend on the level of mismatch between the film and the substrate or even on the substrate symmetry [27].

The substrate material used in most film growth experiments in this work was sapphire (001). The corundum crystal structure of sapphire has the same hexagonal symmetry as wurtzite ZnO and BeO. The mismatch between sapphire and BeO is M $= 43.3\%$ and M $= 31.7\%$ for sapphire and ZnO. However, stabilization of higher order matching between the substrate and a film is also possible. For instance, the matching of one unit cell of sapphire with two unit cell of BeO gives a mismatch of M $= -13.4\%$. The substrates were supplied by Shinkosha. The 2-inch wafers were cut using a diamond knife into pieces of 5 mm by 3 mm. A pre-annealing treatment was used to obtain a step-and-terrace surface morphology before film growth.[28] The annealing treatment was done in air at $1000°$C during 5 hours in a Mila-5000 infrared furnace.

Deposition conditions

The main process parameters for PLD deposition are the background gas pressure, the substrate temperature, the laser fluence, and the pulse rate of the ablation laser. The gas pressure parameter has two important roles. Firstly, it brings additional oxygen to the film surface, ensuring full oxidation of the metal cations. Most of

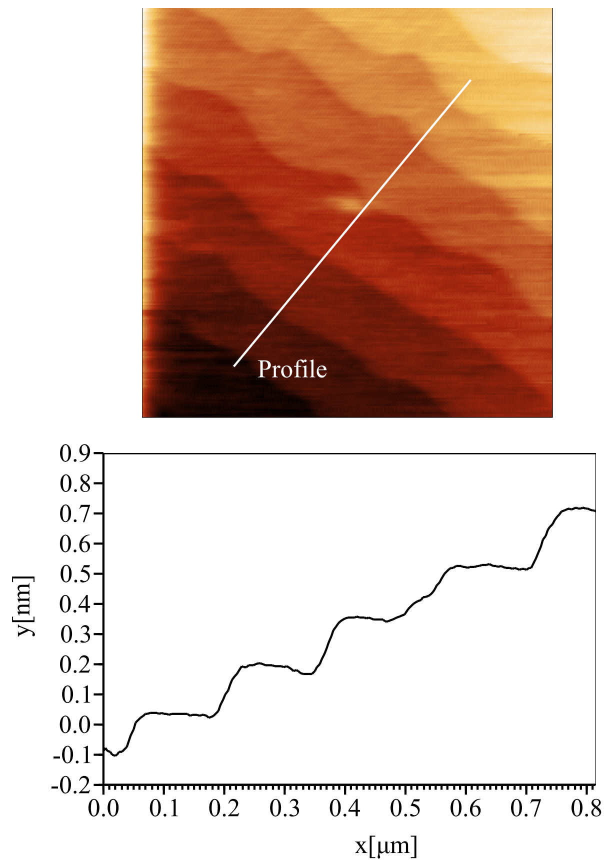

Figure 2.2: AFM image of a pre-annealed sapphire substrate. The image area is 1μm by 1μm. The bottom panel shows a cross-section profile of the step-and-terrace surface, showing that the step height is 1.9Å, i.e., one and half unit cell.

the oxygen needed to form a crystal is delivered by the ablation plume from the target. Secondly, the gas pressure in the chamber affects the kinetic energy of the species that arrive at the surface. If the pressure is high enough, so that the mean free path of the ablated species is shorter than the distance between the target and the substrate, many gas-phase collisions can occur, moderating the kinetic energy in the plume. If the ablated particles hit oxygen molecules before reaching the surface of the substrate, the energy at which they arrive to the sample surface will be lower and the sputtering damage to the deposited film is decreased. As the substrate temperature increases, the migration length of the adatoms increases, allowing greater and faster relaxation of the surface after every ablation pulse. However, if the temperature is increased too much, the long diffusion length and anisotropic crystal surface energies may promote three-dimensional growth or re-evaporation of cations from the surface.

The ablation laser fluence used to ablate the target surface influences the quality of the films. As the fluence increases, the quantity of the ablated species and the growth rate increase. At the same time, the energy transfered from the laser light to the dense plasma of the ablation plume also increases, resulting in higher kinetic energies for individual ions. This may cause increased damage to the film. A balance between the growth rate and the defect generation has to be found for optimal deposition. The ablation threshold is defined as the minimal fluence below which no ablation occurs. It differs from one material to another and sets a boundary condition for the minimum usable fluence. The laser pulse rate and the total number of pulses are used to define the growth rate and the final thickness of the film. A high pulse rate leads to a high growth rate, but leaves less time for the surface to relax between pulses, possibly leading to a rough film surface and lower crystallinity.

One of the main advantages of PLD is the near-stoichiometric transfer of material from the ablation target to the surface of the film. For growing alloy films with arbitrary cation ratios, it would normally be necessary to prepare a new ablation target for each desired alloy composition. However, in order to perform systematic studies of material properties as a function of film composition, it is possible to take advantage of the pulsed ablation process. For the deposition system used in this work, it usually takes about 250 laser pulses to grow a single unit cell layer of ZnO. For BeO, the deposition rate is lower and approximately 1000 laser pulses are used to deposit a single unit cell layer. This means that is possible to synthesize alloys of two compounds by periodically ablating one or the other target. If the targets are cycled often enough, it can be ensured that cation mixing takes place on the surface of the film in the topmost unit cell layer.

(a)

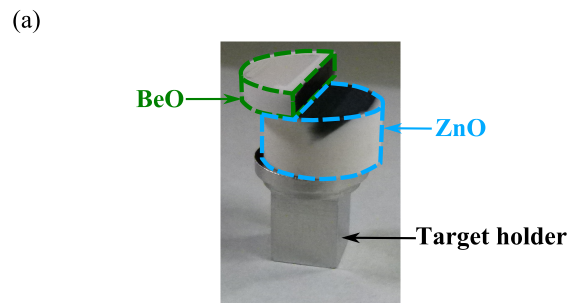

(b)

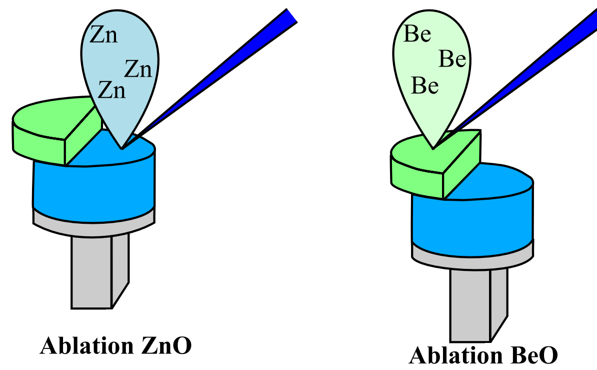

Figure 2.3: (a)Picture of the double target holder composed of one BeO part and one ZnO part. (b) Schematic view of the ablation for each target part.

This technique was used in this work to grow the BeO-ZnO alloy films. Figure 2.3 shows a photograph of a split target with one half consisting of BeO and the other half of ZnO. The X-Y scanning stage of the target manipulator was used to switch the ablation repeatedly between the two target halves, depositing a sub-monolayer film in each deposition cycle. The film composition could be accurately tuned by adjusting the ratio of the numbers of laser pulses fired on each half of the split target.

As shown in Figure 2.4(a), the laser first ablates $(1-x)$ unit cells of ZnO, followed by the growth of x unit cells of BeO with $0 \leq x \leq 1$. For sub-monolayer depositions, rapid surface diffusion can be expected to mix the two precursor materials at the film growth front as the crystal grows, forming a complete unit cell of a $Be_xZn_{1-x}O$ alloy film.

The optimal growth conditions of the alloy were determined by first optimizing the growth of pure ZnO and BeO films. For ZnO films, the best crystallinity was obtained at a substrate temperature of around $700 - 800°$C. The best crystal quality for BeO films was obtained at a growth temperature of $500°$C. The growth rate of BeO drops sharply above $600°$C setting an important restriction for the deposition process. The BeO growth instability will be discussed in Section 3.7.2). Based on these considerations, alloy films were grown at a fixed deposition temperature of $500°$C. The pressure was kept at 10^{-3} Torr as it improved the growth rate of BeO.

Although alloy films could be grown at the relatively low growth temperature of 500°C, the crystal quality of films grown at very low temperatures is usually quite low. A substrate temperature modulation technique was therefore considered to overcome this issue. Figure 2.4(b) illustrates the deposition steps. The deposition of one unit cell of film was still performed at a single fixed temperature of $300°$C. The very low temperature was used to minimize film composition deviations from the desired cation stoichiometry. After the growth of a single monolayer, the film sample was annealed at a higher temperature in order to improve the crystallinity. The annealing temperature was usually $900°$C and the annealing lasted for about 1 min. These deposition and annealing cycles were repeated for each monolayer of the film. The typical alloy film thickness was 20 monolayers ($\approx$ 10 nm).

The sample holder for the deposition system was designed to provide homogeneous heating of the substrate and to minimize heat loss. Figure 2.5 shows a cross-section view of the stainless steel holder. The substrate crystal is mounted on a nickel block and held in place by two thin stainless steel wires. The nickel block serves two purposes. The oxidized back surface of the block absorbs light from

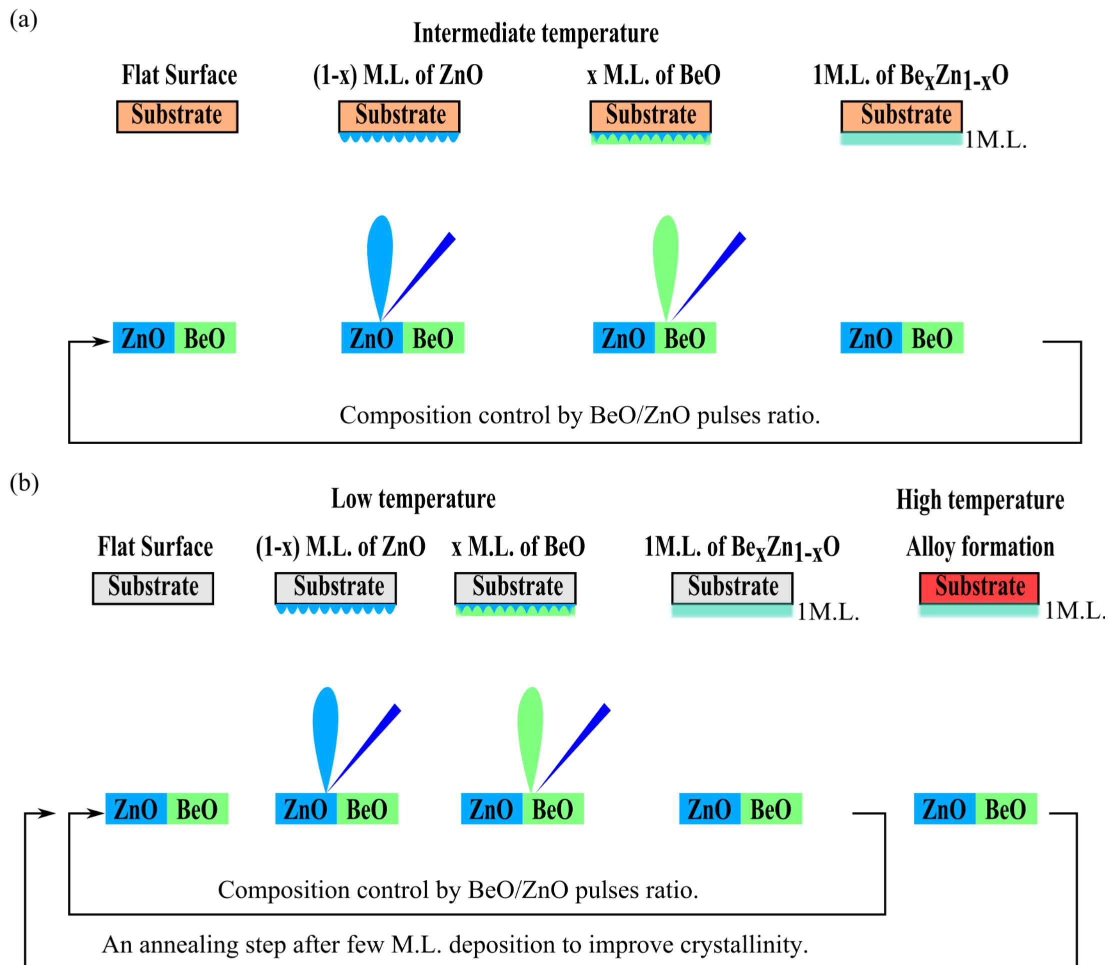

Figure 2.4: Deposition process for controlling the beryllium content in an alloy film. (a) Multi-target PLD deposition by successively ablating BeO and ZnO part of a target. The cycle is repeated for the growth of each unit cell layer of the film. (b) Temperature-modulated multi-target PLD, where each unit cell deposition cycle is followed by a high-temperature annealing step to improve the film crystallinity.

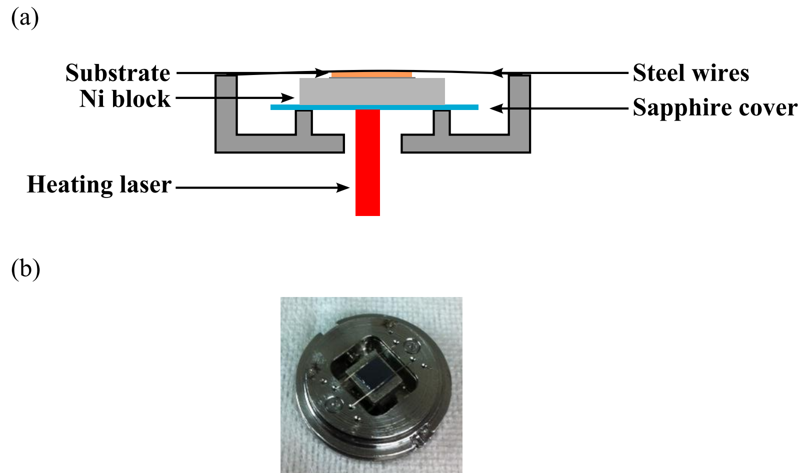

Figure 2.5: (a)Schematic view of the sample holder use for film growth. (b) Photo of the sample holder, showing the outer ring of the sample holder, the thermally isolate nickel block in the center, and a substrate crystal held in place with two stainless steel wires.

the substrate heating laser. The nickel block thickness is sufficient to efficiently distribute the heat over the whole substrate area. Indeed, nickel has relatively good thermal conduction at 90.9 W/mK and a high melting point of 1455°C. Nickel is fairly stable at high temperature, even in an oxidizing ambient. However, it is possible to oxidize the surface of a nickel block by long annealing in air. The NiO_2 layer that forms is nearly black and thus an efficient absorber for the infrared light from the heating laser. The nickel oxides are not particularly volatile in vacuum, which means that there is little nickel contamination in the deposition chamber. To improve the temperature homogeneity of the substrate and to correct for minor surface roughness of the nickel block, thin nickel sheets (typically 5 μm thick) were inserted between the nickel block and the substrate. The nickel block was thermally isolated from the main body of the sample holder by sapphire sheets to minimize heat loss and thus reduce the maximum laser power required to heat a substrate to 1000°C.

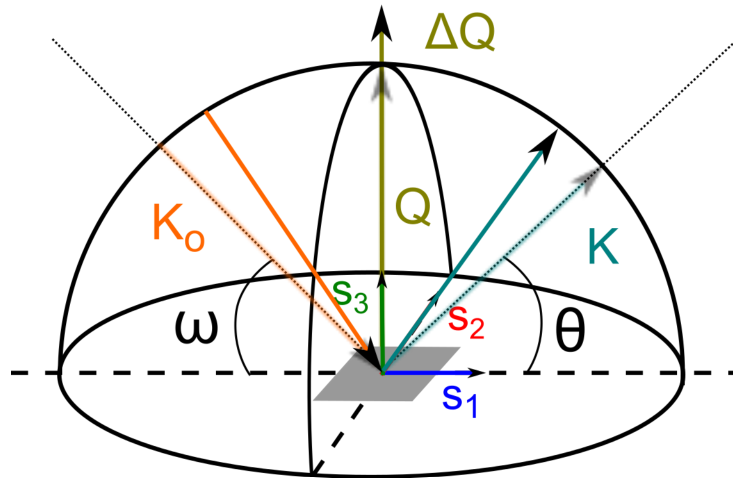

Figure 2.6: The geometry of a 2θ scan. K_0 and K are the incident and diffracted wave vectors, ω and θ are the incident and diffracted beam angles, Q is the scanning wave vector, and s_i are the basis vectors. ΔQ represents the scanned segment of the reciprocal space.

2.3 Structural and morphology analysis

2.3.1 X-ray diffraction

The crystal quality of the films was investigated by X-ray diffraction. A crystal is a periodic structure of atoms. When a crystal is illuminated with a beam of x-ray light that has a wavelength similar to the crystal period, a diffraction pattern is generated. This diffraction pattern follows Bragg's Law, $2d\sin(\theta) = n\lambda$, where d is the crystal periodicity, θ the angle of incidence, n the order of the diffraction and λ the wavelength of the X-ray source. The measurements were carried out on a Rigaku SmartLab diffractometer with a Cu K$_\alpha$ source ($\lambda = 1.54056$Å). Symmetric $\theta/2\theta$ scans were measured for all thin film samples. The presence of a diffraction peak in the scan gives information on the crystal quality and orientation of the grown film. The geometry of this scan is shown in Figure 2.6. The X-ray beam from the source is directed at the sample, leading to a diffracted beam when the Bragg condition is fulfilled. The diffraction angle is linked to the cell parameters and the obtained pattern is characteristic of a particular material.

The in-pane ϕ scans and pole figures were measured using a 4-axis Phillips

diffractometer. The relative orientation of the film to the substrate was determined from those measurements.

2.3.2 Film thickness measurement

The film thickness was measured with a stylus profilometer (Dektak 6M). In this instrument, a diamond stylus is brought into contact with the film surface and scanned along a straight line while monitoring the vertical movement of the stylus. This measurement gives the thickness of the film if a suitable edge is available. As shown in Figure 2.7, the substrate crystal is held in the sample holder by two steel wires. During film deposition, these wires act as shadow masks, under which no material is deposited. After removing the substrate from the sample holder, each sample thus has two lines where the bare substrate surface is exposed, providing the necessary step edges for profilometry. By measuring the depth of these valleys, it is possible to determine the thickness of a thin film. The accuracy of the measurement is limited to about 20%, mostly due to film thickness variation across the substrate surface.

2.3.3 AFM

Thin film sample surface morphologies were analyzed by atomic force microscopy (AFM). A microscope of this type can scan a sharp needle over a small area ($S \approx 1\ \mu\mathrm{m}^2$) of a film, while measuring the height of the needle. Measurements can be done either in contact mode or in non-contact mode, where short-range electrostatic forces between the needle and the surface force the tip higher or lower. The needle is attached to a soft cantilever, which bends when the needle moves vertically. This bending is measured optically and used to generate a height map of the sample surface. While the tip and cantilever scan along a line across the surface, the height of the sample stage is adjusted with a piezo actuator to maintain a constant cantilever bend angle under PID control. The stage height signal is used to construct the actual surface morphology map of the sample surface. The measurements were done with a Shimadzu 5100 series AFM machine.

2.3.4 Plume characterization

The ablation of a target by a laser is a complex mechanism involving several processes. It is interesting to investigate the chemical composition of the plume in order to identify the main vaporized species. This information is necessary for

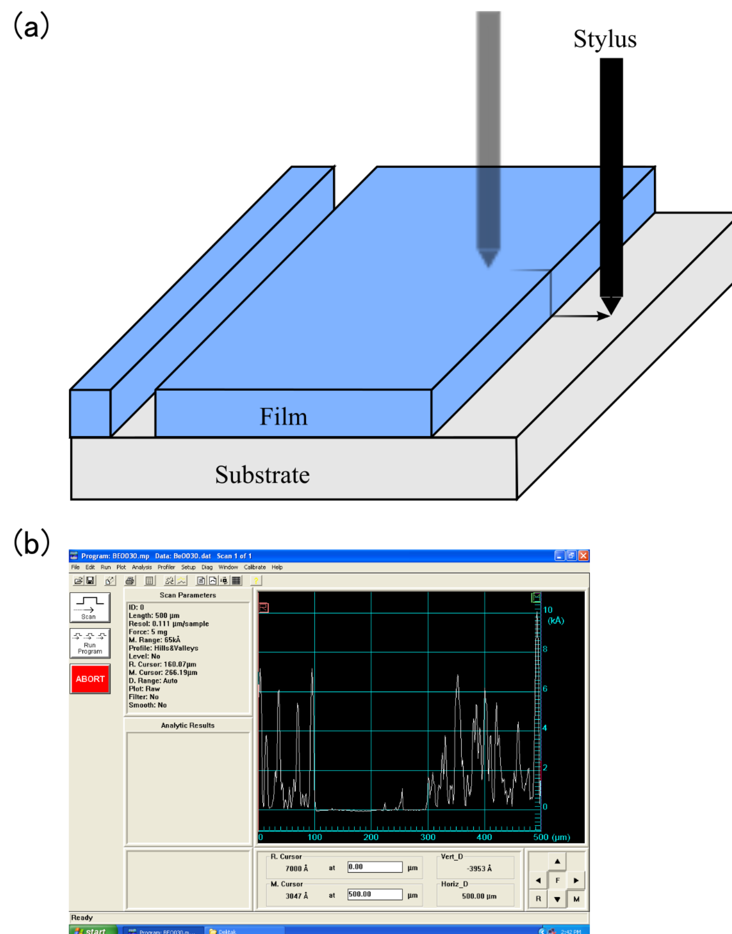

Figure 2.7: (a) Schematic view of the profilometer operation. (b) A typical film thickness profile, illustrating the film thickness measurement process.

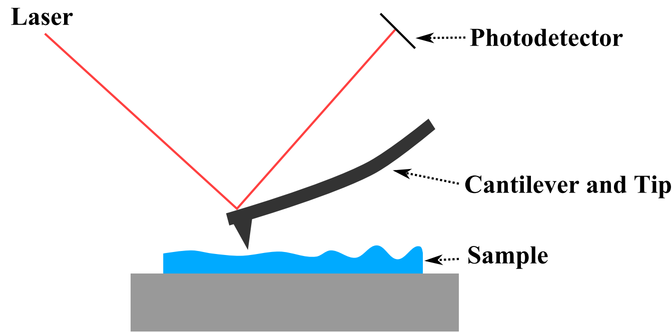

Figure 2.8: Schematic view of an AFM measurement.

determining the growth mechanism of the film, which depends on whether metal ions or oxide clusters nucleate on the substrate. A simple way to investigate this plume composition is to record the time-dependent charge carried by the plasma in the plume. If the measurement is performed at a fixed height above the target surface, and if the plume is assumed to contain mostly ionized species, the current profile can be viewed as a time-of-flight spectrum of the various ion or cluster species in the plume. An electrode was set inside the deposition chamber for this purpose at the position of the substrate. This electrode was used as a collecting electrode to measure the charge of the arriving species. The current was measured with an oscilloscope that was triggered by the excimer laser pulse. The ablation of the target by the laser generates ionic, atomic and molecular species, leading to the appearance of a current in the electrode circuit. It is important to note that this measurement reflects only the charged species, leaving the neutral species unmonitored. Figure 2.8 presents a set-up diagram of this measurement.

The identification of the species in the plume was done by comparing the time of flight and assuming that all the species have the same kinetic energy, i.e., that the plume is thermalized. The time of flight is in this case given by $t = x\sqrt{m/2E}$, where x is the distance to the electrode, m the mass of the species and E the energy of the species. Therefore, the ratio between two time-of-flight peaks can be expressed as $t_1/t_2 = \sqrt{m_1/m_2}$, where indices 1 and 2 represent two different charged species. As the possible species are known (Be, O or BeO), it is possible to identify the relative ratio of the various species in the plume.

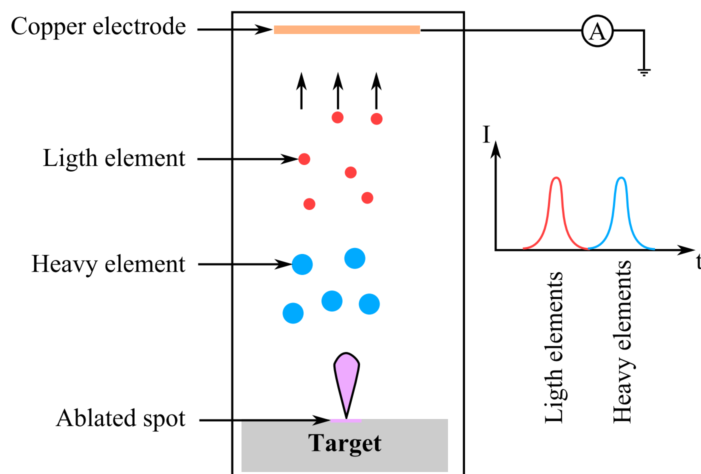

Figure 2.9: Time-of-flight plume analysis diagram.

2.4 Optical and electrical measurement

2.4.1 Pyroelectric characterization

Pyroelectricity is a property of all polar materials. A pyroelectric material is also piezoelectric, but not always ferroelectric. The polarization of a material is temperature dependent, which means that under the application of a fast temperature step, the surface charge of a sample changes. This surface charge change can be measured as a small current pulse if an electrode is attached to the sample surface.

To measure the pyroelectric current, the temperature change has to be as fast as possible. This can be achieved by illuminating a thin film sample with a chopped laser beam. The temperature of the exposed film area increases at the beginning of a lase pulse and therefore a pyroelectric current flows. It is also possible to distinguish between a pure pyroelectric (transient) current and a persistent photoelectric current contribution. The generated current is measured by attaching an electrode to the sample surface. The counter electrode at the back of the film sample is usually formed by a conducting substrate, in this case Nb:$SrTiO_3$. The top electrode on the film surface was formed by thermally evaporated metal. The presence of a sufficiently thick metal top electrode also means that the photocurrent contribution is reduced. For this measurement, a BeO film was deposited on a Nb:$SrTiO_3$ (111) substrate. This substrate is metallic and can thus be used as a bottom electrode. The films grown on the (111)-oriented cubic $SrTiO_3$ sub-

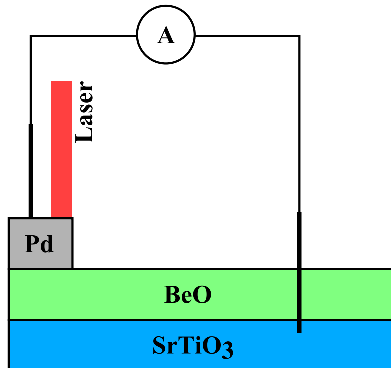

Figure 2.10: Pyroelectric measurement set up: the film is periodically heated by a chopped laser beam. The current generated by the temperature step is measure between the Pd top electrode and the conducting substrate.

strate exhibited similar crystallinity as these grown on sapphire substrates. The top electrode material was palladium, which was chosen for its work function. The sample configuration is shown in Figure 2.10.

Contact to the bottom electrode was done by ultrasonic aluminum wire bonding and the contact to the top electrode was made by pressing a metal needle onto the film surface. A laser with a wavelength of $\lambda = 345$ nm was used to modulate the sample temperature while the pyroelectric current was measured. The generated current was measured with a wide bandwidth high-gain current-to-voltage (I/V) converter. The use of an I/V converter is essential due to the low magnitude of the current, typically in the range of pA.

2.4.2 Reflectivity and transmission measurement

Various optical characterization techniques are important when studying the growth of potentially useful optoelectronic materials. When a semiconductor or an insulator is exposed to monochromatic light, the light beam can be partially reflected, transmitted, and absorbed. The following discussion will present a brief overview of the physical mechanisms behind these phenomena and the relation with the material proprieties.

Transmission spectra and the band gap.

The definition of transmission is somewhat ambiguous, depending on whether a single interface or the whole crystal is considered.

The first definition include the absorption, scattering or luminescence processes.

The second case is more common and convenient: transmission is defined as $T = I_t/I_0$, where I_0 is the intensity of the incident radiation and I_t is the intensity of the transmitted radiation through a sample. The value of I_t is measured using a spectrometer in transmission mode. Figure 2.11(a) shows the set-up of the measurement. The incident intensity, I_0, is known and the transmitted intensity is measured. The measured transmission corresponds to the transmission of the film and the substrate. The substrate contribution can be eliminated by measuring a baseline with the bare substrate. In this case the transmission of the film can be expressed as $T_{\text{film}} = T_{\text{Measured}} - T_{\text{substrate}}$. This measurement does not consider reflection losses at the film interfaces.

The transmitted light intensity in a semiconductor/insulator is mainly determined by the absorption. Indeed, a photon with an energy above the band gap can be absorbed, lifting an electron from the valence band to the conduction band. The absorption is given by the imaginary part of the complex dielectric function. If the incident light is considered to be a monochromatic wave, the expression for light propagating inside the semiconductor in complex form is: $\vec{E} = \vec{E_0}\exp[k_0(ict - in_r(\omega)r + n_i(\omega)r)]$, where $k_0 = \omega/c$ is the wavelength in vacuum, $n_r(\omega)$ and $n_i(\omega)$ are the real and imaginary parts of the complex refractive index, $n(\omega)$. From this expression, the spatial propagation of the wave is determined by the refractive index $n_r(\omega)$, whereas the damping part is characterized by the extinction index $n_i(\omega)$. The complex refractive index is defined as: $n(\omega)^2 = \epsilon(\omega) = \epsilon_r(\omega) + i\epsilon_i(\omega)$, where $\epsilon(\omega)$ is the dielectric function. The absorption of the film is therefore directly linked to the evolution of the imaginary part of the dielectric function. In this case, it is assumed - and it will be discussed in the following part- that the change of the sample transmission is mainly due to the change of absorption. The reflected part and the other scattering processes are neglected. An analytical expression for $\epsilon_i(\omega)$ can be derived for a material with a direct band gap E_g [29]

$$\epsilon_i(\omega) = \begin{cases} A(\frac{\hbar\omega}{E_g})^{-2}(\frac{\hbar\omega}{E_g} - 1)^{1/2} & \text{for } \hbar\omega > E_g, \\ 0 & \text{for } \hbar\omega < E_g, \end{cases} \tag{2.1}$$

where A is a constant.

The absorption rate scales with the square root of the photon energy. The absorbance of a material is used to express absorption on a logarithmic scale in units of length

$$\alpha = -\frac{1}{l}\log(\frac{T}{(1-R)^2}) \approx -\frac{1}{l}\log(T) \tag{2.2}$$

if the reflection part is neglected. The absorbance thus has the same wavelength dependence as absorption. Neglecting the reflectivity is justified in many cases. Indeed, the reflected intensity for the BeO - air interface is about 7% at $\lambda \approx 600$ nm. Based on these considerations, the following expression can be derived

$$\alpha(\hbar\omega)\hbar\omega \propto \sqrt{\hbar\omega - E_g}. \tag{2.3}$$

The band gap of a material can be obtained by fitting experimental absorption spectra with this formula.

One of the main limitations of this measurement for thin films is that it probes the smallest band gap in the light path, which can correspond to either the film or the substrate. The band gap of the substrate material therefore has to be sufficiently larger than the thin film material to neglect the absorption in the substrate. In the case of BeO-based wide band gap insulators, Al_2O_3 is a suitable candidate up to a wavelength of about 137 nm, since the band gap energy of sapphire is ≈ 9 eV. For measuring the absorption spectra of films with wider band gaps than 9 eV, it would be possible to use a BeO substrate. However, BeO substrates are not available. Another solution is the measurement of reflectivity spectra. With this measurement, the substrate is not contributing to the spectrum and it is possible to determine the band gap of the film independently of the substrate.

Reflectivity and the band gap.

The reflectance of a medium is defined as $R = I_r/I_0$, where I_0 is the intensity of the incident radiation and I_r is the intensity of the reflected radiation. The precise demonstration of the relation between the the reflectivity and the band gap is relatively complicated. The mechanism, on the other hand, is simpler and offers a good understanding of the wavelength dependence of the reflectivity. Good conductors, such as metals, have high reflectivity. This is related to the skin effect. The electromagnetic field associated with the incident light generates a surface current that tends to reflect the incoming photon. The current is created in a thin layer of the medium, with a thickness of $\delta = \sqrt{\frac{2}{\omega\mu_0\sigma}}$, where ω is the incident light frequency, μ_0 is the permittivity of vacuum and σ is the conductivity of the

medium. Thinner skin layer results in a stronger reflection. Therefore, when the photon energy reaches the band gap, the photocarrier concentration increases and the film acts as a mirror for the incident photons. The presence of a maximum in the reflectivity therefore correspond to the band gap value, where the photocarrier generation efficiency is the highest.

Some limitations of the optical absorption and reflectivity measurements should be pointed out. For the short wavelength part of the spectrum, below 300 nm, air becomes a strong absorber, affecting the measurement. Therefore, the intensity decreases strongly and reduces the signal-to-noise ratio. Another issue is the necessity to grow thick enough films. In very thin films, the ratio of the film contribution over the substrate contribution becomes lower and in transmission measurements the film can act as an anti-reflection coating leading to an apparent increase of the transmission intensity.

2.4.3 Photocurrent measurement

Introduction

Semiconductor and insulator band structures exhibit a forbidden gap in which no electrons are present. In an ideal case, the conductivity of such materials is due to the electrons that populate the conduction band. However, if the band gap energy is large, the population of the conduction band has to involve some external excitation to reach practical conductivity levels (Figure 2.12). One possible way to excite electrons to the conduction band is to absorb a photon. In this process, the photon energy has to be larger than the band gap energy to lift an electron from the valence band to the conduction band. From the point of view of photoconductivity, the main difference between a semiconductor and an insulator is the origin of the excited carriers. In case of an intrinsic narrow-gap semiconductor, thermal excitation is predominant. In an insulator, the thermal excitation is negligible and almost all carriers in the conduction band are due to optical excitations. The relative variation of detected photo current is therefore higher in the case of an insulator.

Wavelength dependence

Figure 2.13 shows the evolution of photocurrent as a function of wavelength for an insulator. For photon energies below the band gap energy, E_g, no absorption is possible, the photon passes through the insulator and no photocarriers are gener-

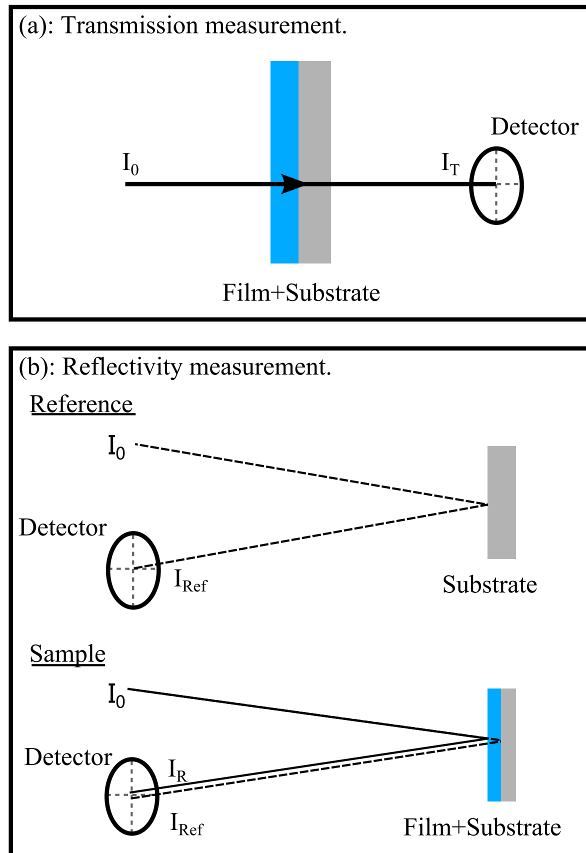

Figure 2.11: (a) Measurement of a transmission spectrum through a film and a substrate. (b) Measurement of a reflectivity spectrum. The reflectivity spectrum of a bare substrate and the sample (film + substrate) are recorded in order to correct the measured reflection intensity for the substrate reflectivity. The incident and reflected beams are close to the normal of the surface. For clarity, the beam path divergence is expanded in the figure.

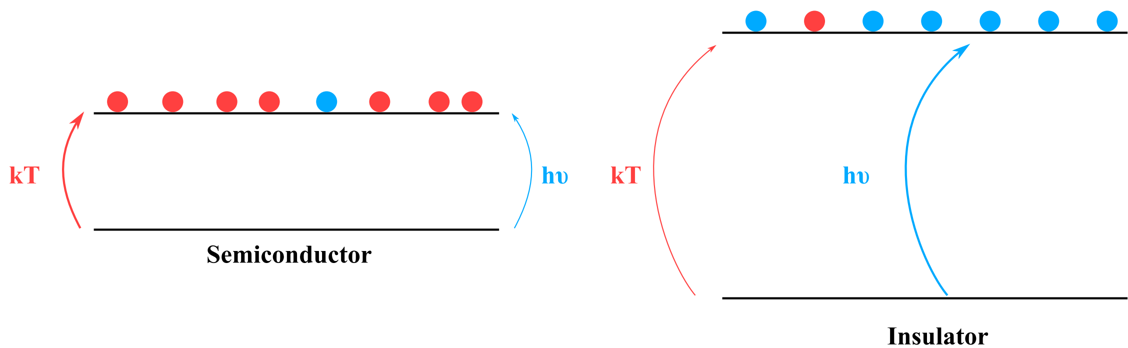

Figure 2.12: Excitation of electrons in a semiconductor or an insulator.

ated. If the energy of the photon exceeds the band gap energy, the photon may be absorbed and a photocarrier can be generated. in general, absorption can occur for energies above the band gap as well, as long as a suitable unoccupied electronic state is available. However, it has been reported that the measured photocurrent decreases when the photon energy is increased above E_g and finally reaches a constant value in the deep ultraviolet part of the spectrum[30]. In a simplistic band gap picture, it would be reasonable to expect that the photocurrent would reach a constant value after crossing the band gap energy, as nearly all photons are absorbed, generating photocarriers. However, an important parameter in the photocurrent characteristic is the recombination rate, which tends to counterbalance the carrier generation rate. The balance between these two mechanisms controls the actual observed intensity of the photocurrent. Therefore, the decreases of the photocurrent above the band gap energy can be explained by considering an increase of the recombination rate. The recombination rate is usually determined by the defect characteristics. Two contributions in recombination can be distinguished: the volume and the surface contributions. As the surface defects and volume defects are different, the recombination rates should also be different. The maximum of the photoconductivity therefore corresponds to the maximum of photocarrier generation and the minimum of carrier recombination. For intermediate energy photons, just above the band gap energy, the absorbance is still relatively small and light can penetrate deep into the material. Due to this, volume recombination is the rate-limiting factor. However, for higher energy photons, the absorption occurs in a very thin surface layer and the recombination rate is determined by the density of surface defects [31].

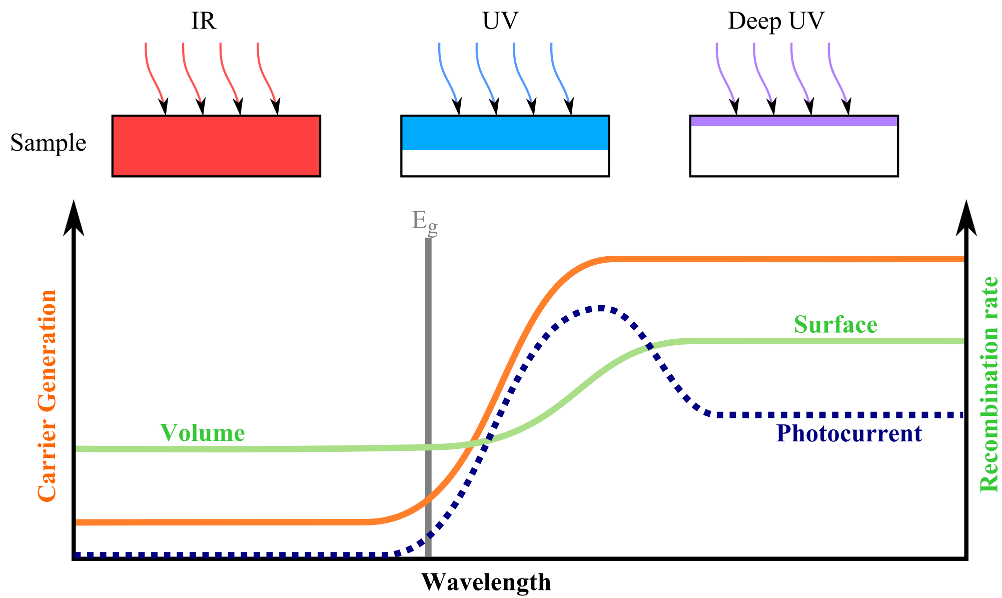

Figure 2.13: Photocurrent evolution as a function of the photon energy.

It is possible to derive a relation between the photocurrent, the absorption coefficient of a film and the recombination rate.[31] If the thickness a sample is small enough, the relation can be simplified to $I_{\text{Photocurrent}} \propto 1 - e^{-\alpha l}$. Therefore, plotting the logarithm of the photocurrent versus the wavelength gives the equivalent of an absorption spectrum. The band gap energy can then be derived from a linear fitting.

Figure 2.14 shows the photoconductivity spectral response measurement setup. White light from a short-arc Xenon lamp is passed through a double monochromator. The monochromator is composed of a set of mirrors and gratings that spatially disperse the white light spectrum. By rotating the mirrors and the gratings, a monochromatic beam is obtained. Light from the monochromator is collimated and passed through a beamsplitter. The split beam illuminates a calibrated wide-area Si photodiode that is used for the incident light intensity measurement. The main part of the beam is focused on the surface of the sample. A chopper in the beam path was used for lock-in measurements of the photocurrent.

Aluminum leads were attached to the sample films by ultrasonic wire bonding. To measure the photocurrent, the samples were under a constant applied bias and the sample current was converted to a voltage signal with a current-to-voltage

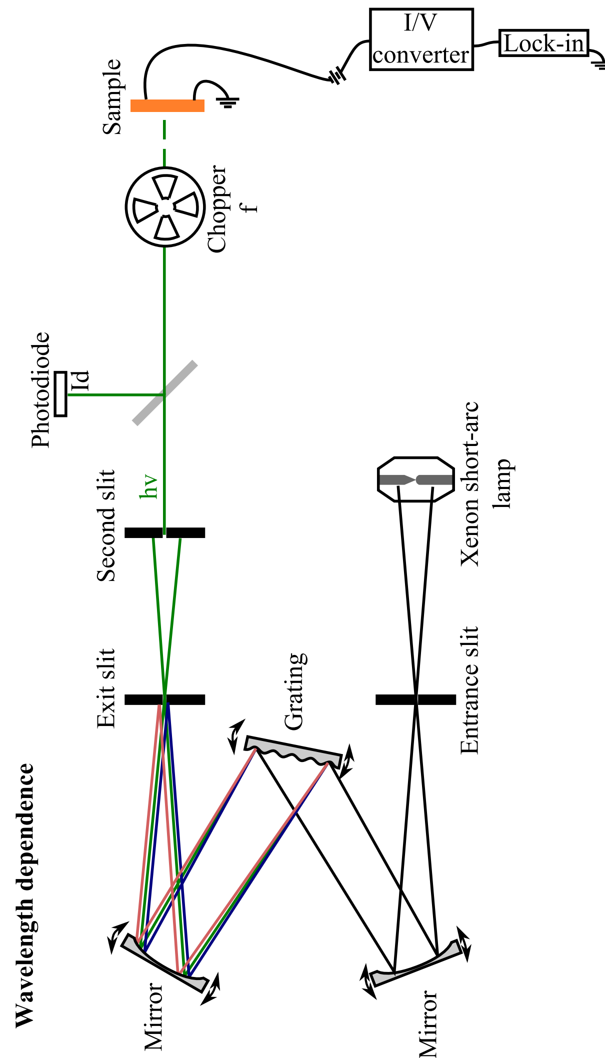

Figure 2.14: Schematic view of the setup used for measuring the wavelength dependence of the photocurrent. Monochromatic light is chopped at a constant frequency f. The induced photocurrent is converted to voltage with a transimpedance gain G. This voltage is measured with a lock-in amplifier synchronized to the chopper frequency. The photon wavelength is selected with a double monochromator.

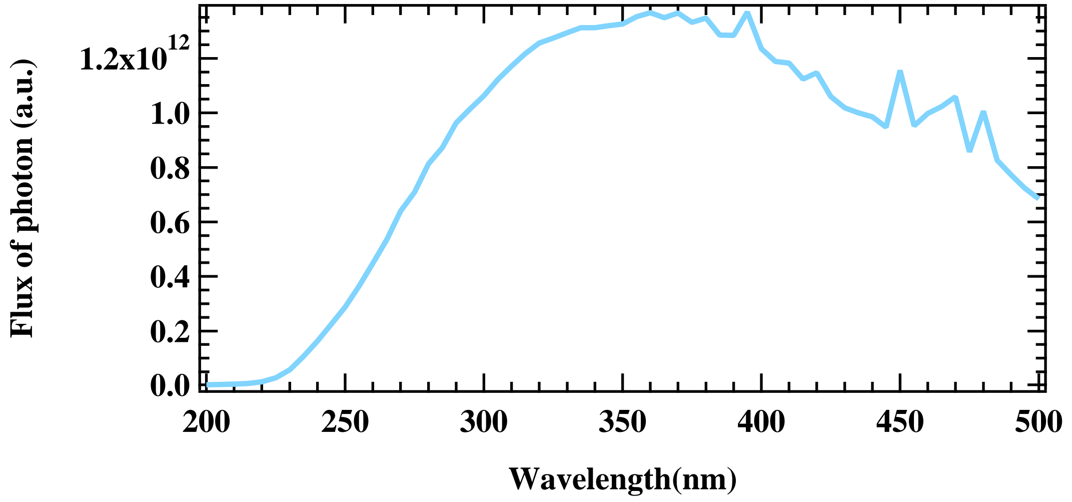

Figure 2.15: Photon flux as a function of wavelength.

converter. The voltage amplitude was measured either with a lock-in amplifier or digitized directly.

During photoconductivity measurement the wavelength of the incident light was scanned from 500 nm to 200 nm in 10 nm steps. For each step, a waiting time was observed in order to reach a steady state since a transient response was observed each time the wavelength was changed. The change of wavelength has two mains consequences. First, the photon flux changes due to the non-uniform emission spectrum profile of the Xenon lamp (Figure 2.15). The recombination rate in the thin film sample is also wavelength dependent. The sudden change of wavelength therefore places the film in a non-equilibrium state. A Python script was used to convert fit the exponential rise and decay times for each measurement step and derive the photocurrent amplitude.

The measured current has to be normalized to the photon flux. The result of this calculation is the photocarrier yield that gives the number of electrons detected per photon $Y = F_{\text{Electron}}/F_{\text{Photon}}$. First, the electron yield is calculated as

$$F_{\text{Electron}} = \frac{I_{\text{Photocurrent}}}{e}, \tag{2.4}$$

where e is the elementary charge. The monochromatized light intensity spectrum was calibrated before measurements, giving a function $L(\omega)$, which links the mea-

sured photodiode current to the power of the beam. Dividing the incident power by the energy of a single photon gives the photon flux

$$F_{\text{Photon}} = \frac{I_{\text{Photodiode}}}{L(\omega)\hbar\omega}. \tag{2.5}$$

Frequency dependence

A chopper was used in the photoyield measurements described in the previous Section. The purpose of using a chopped light source was to suppress the effects of long relaxation effects that are related to slow trapping processes and not relevant for band gap analysis.

It is possible to use the same measurement setup to analyze the various relaxation time constants in the thin film samples. In this case, the wavelength of the light source was held fixed, while the chopper frequency was changed and the photocurrent amplitude was recorded as a function of the chopping rate. The result is a plot that can be used to extract the lifetime of the photocarriers. The relation is given by

$$I = I_1 \tanh \frac{1}{4\tau_1 f} + I_2 \tanh \frac{1}{4\tau_2 f}, \tag{2.6}$$

where the existence of two relaxation phenomena is assumed, with relative intensities I_1 and I_2, and characteristic time constants τ_1 and τ_2. The light chopping frequency is given by f. The original theoretical analysis by Ryvkin only assumed a single time constant.[32] However, experimental data analysis shows a much better fit if two time constants, τ_1 and τ_2, are used. This model has been applied successfully to a variety of different materials.[33, 34] Figure 2.16 shows the measurement setup used in these experiments.

Light intensity dependence

The in-gap defect structure can be investigated by looking at the light intensity dependence of the photocurrent. Several models have been developed to link the observed behavior to the defect distribution.[35] The behavior of the photocurrent in various cases can be expressed by $I_{\text{photocurrent}} \propto F^{\alpha}$, where F is the light intensity and α is a parameter. For instance, a supralinear behavior($\alpha > 1$) has been observed for $SrTiO_3$[30], whereas a sublinear behavior has been measured for Sb_2S_3.[36]

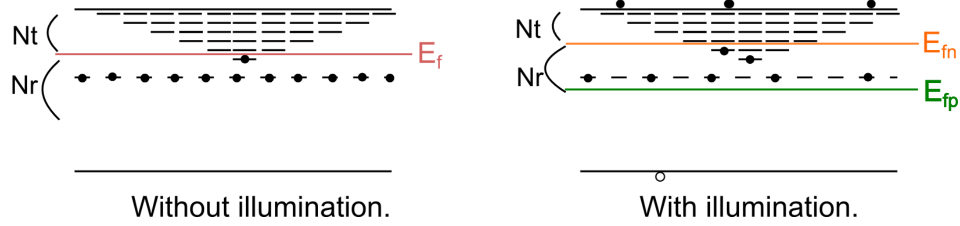

Figure 2.16: Defect distribution that results in a power-law dependence of photoyield on the light intensity with a coefficient less than 1. N_r is the concentration of the recombination centers, N_t is the concentration of traps, E_f is the Fermi level, $E_{fn}$is the pseudo-Fermi level for electrons, $E_{fp}$is the pseudo-Fermi level for holes.

At a constant wavelength, the increase or decrease of light intensity corresponds to an increase or decrease of the photon flux. The concentration of photocarriers is defined by: $N \propto F\tau$ where F is the photon flux and τ is the photocarrier lifetime. An illuminated sample is in a non-equilibrium electronic state. The Fermi level is split into two pseudo-Fermi levels that define the limiting occupation levels for electrons and holes. Figure 2.16 shows the splitting of the pseudo-Fermi levels. In the case of the electron pseudo-Fermi level, an increase of the photon flux pushes the pseudo level toward the conduction band and may cross over some of the in-gap defect levels.

An accepted model for explaining the sublinear photoyield behavior is to consider an exponential distribution of defects between the Fermi level and the conduction band and an occupation of the recombination center by the majority carriers. The exponential distribution is defined as

$$N_t(E) \propto e^{-\frac{E_c - E}{kT_1}}, \tag{2.7}$$

where E_c is the conduction band edge energy, k is the Boltzmann constant, T the absolute temperature and T_1 is a characteristic temperature of the defect distribution. By increasing the illumination intensity, the role of the lowest defect levels changes from trapping to recombination centers filled by the minority carriers. The photocurrent can be modeled by

$$I_{\text{Photocurrent}} \propto F^{\frac{T_1}{T+T_1}}, \tag{2.8}$$

where F is the photon flux.

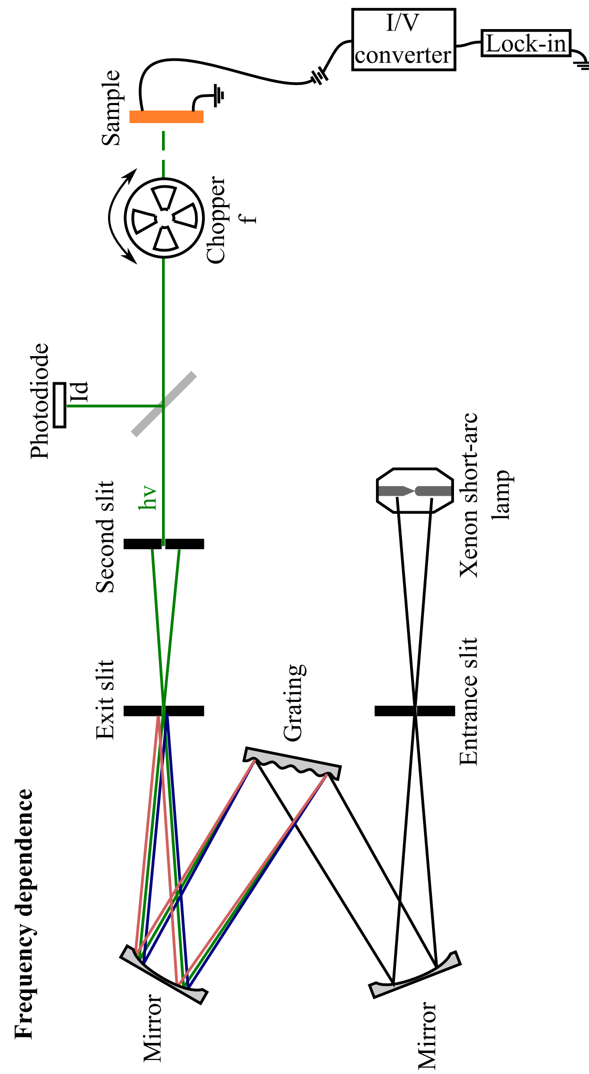

Figure 2.17: Schematic view of the photocurrent measurement for chopping rate analysis.

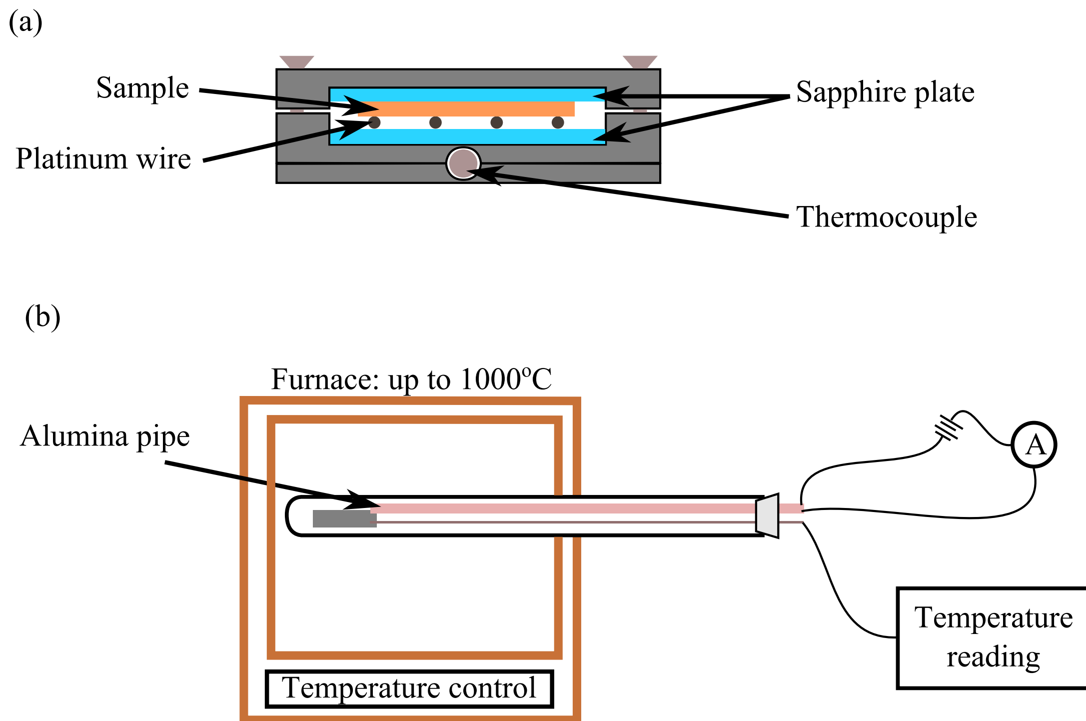

Figure 2.18: Schematic view of the high-temperature probe and the measurement setup. (a) Front view of the high-temperature holder. (b) Measurement setup inside a furnace.

2.4.4 High-temperature resistivity measurement

As stated in the introduction, wide-gap insulators are of prime interest for high-temperature electronic applications. It is therefore important to measure the resistivity of wide-gap insulator films well above the room temperature. To measure the resistivity, a special high-temperature probe was built for measuring the resistance of thin film samples in air at temperatures of up to 800°C. The construction of the probe head is illustrated in Figure 2.18. The holder frame was made of steel and had an integrated K-type thermocouple. Electrical contacts to the film surface were made by pressing the sample against four parallel platinum wires. Two sapphire plates were used sandwich the sample and the lead wires in order to prevent leak currents. The whole probe was inserted inside a small electric furnace with a maximum temperature of about 1000°C.

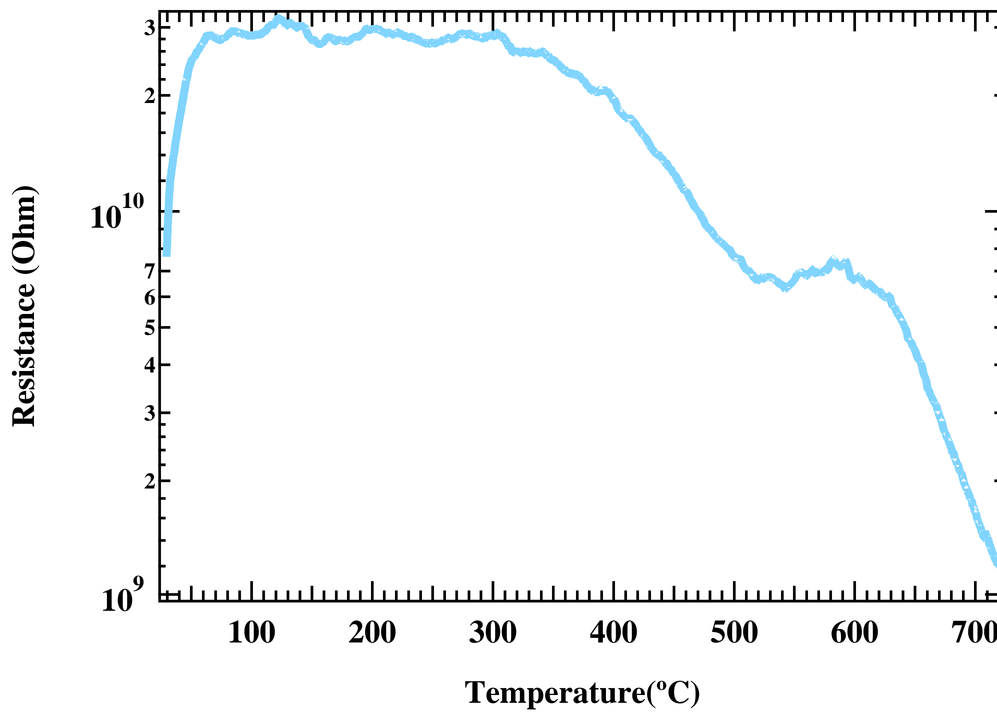

Figure 2.19: Resistance of a sapphire substrate as a function of temperature.

The temperature of the furnace was set to a desired value and the actual sample temperature was measured with the thermocouple close to the thin film sample. As the samples exhibit very high resistance, most measurements were done in a two-point configuration with a Keithley 487 sourcemeter. A resistivity curve of an empty Al_2O_3 sample stage was measured under an applied 20 V bias. It represents the maximum resistivity measurement possible with this setup.

Chapter 3

BeO growth stability

3.1 Introduction

Beryllia is the lightest stable oxide. It is frequently used in the form of bulk ceramic, but rarely available in single crystal form due to possible adverse health effects of inhaled oxide powders. It is therefore interesting to study the growth behavior of beryllia thin films, since this makes it possible to study most of the physical properties without having to work with large quantities of a potentially hazardous material.

Crystalline BeO films has been studied before , with a particular interest in the use of beryllia in dosimeters.[37]. Amorphous beryllia films have found use as efficient diffusion barriers in field-effect transistor gate insulator stacks.

In this chapter, the phase formation stability was investigated in thin films grown by pulsed laser deposition (PLD) and analyzed by standard XRD measurements. Three growth regimes were identified: amorphous growth, crystalline growth, and rapid sublimation. The optimum conditions for crystalline beryllia growth were identified. The range of deposition conditions where no film growth occurs (high temperature) was investigated. The deposition plume composition was measured to obtain additional information on the film growth kinetics. The presence of metallic Beryllium in the plume suggests the re-sublimation of the deposited species is responsible for the rapid loss of growth rate at elevated temperatures. The polarity of BeO films was measured by pyroelectric analysis of thin beryllia films deposited on metallic Nb:$SrTiO_3(111)$ substrates. The dielectric permittivity and the loss figure were estimated.

3.2 BeO growth optimization

The BeO film growth was optimized to obtain the best crystallinity as determined by x-ray diffraction. The number of parameters for the optimization was narrowed down to the background oxygen pressure and the substrate temperature. Those two parameters have the strongest effect on the crystal quality of the film. The oxygen background pressure was selected in the range of 10^{-6} Torr to 10^{-3} Torr. In this pressure range, the deposition process varies between typical molecular-beam epitaxy conditions, where evaporated ions have few gas-phase collisions, to typical pulsed laser deposition conditions, where the plume interacts strongly with the ambient gas atmosphere. At high pressures, the ablated species from the target collide with many oxygen atoms before reaching the substrate. This reduces the kinetic energy of the atoms or clusters impinging on the film growth front. The

lower kinetic energy of adatoms means that there is less chance of re-sputtering the film surface, but it also means that the thermalization of adatoms is faster, and the average surface diffusion length shorter, possibly promoting three-dimensional growth.

The substrate temperature was varied between room temperature and 900°C. The crystallinity of a film usually improves at higher growth temperatures. The laser pulse rate was fixed at 100 Hz in order to ensure a reasonable growth rate. The fluence was set at 0.6 J/cm^2, which is slightly above the ablation threshold energy density. The conditions are summarized in Table 3.2.

Parameter	Value
Temperature	30°C - 900°C
Pressure	10^{-6} Torr - 10^{-3} Torr
Fluence	0.6 J/cm^2
Frequency	100 Hz

The target and the substrates

The ablation target was a 99.5% purity BeO polycrystalline ceramic pellet supplied by American Beryllia. Different substrates were used for the deposition. Sapphire (100) substrates were used for structural analysis of BeO. $SrTiO_3$ and Nb:$SrTiO_3$(111) crystals were also used for electrical characterization. The Nb:$SrTiO_3$ substrates were used as a bottom electrode for pyroelectric measurement where a metallic bottom electrode was required. $SrTiO_3$(111) has a hexagonal symmetry with an in-plane lattice constant of $\sqrt{2}a_{\mathrm{SrTiO_3}} = 5.52\text{Å}$.

3.3 X-ray diffraction analysis

The deposition conditions were varied in order to find the optimum substrate temperature and oxygen pressure for achieving the sharpest and highest intensity BeO diffraction peaks in symmetric $\theta/2\theta$ XRD scans. Figure 3.1 presents a $\theta/2\theta$-scan of a BeO film grown on sapphire at the optimal deposition conditions. The oxygen pressure was $P_{\mathrm{O_2}} = 10^{-3}$ Torr and the sapphire (001) substrate temperature was 500°C. The film thickness was about 150 nm. The peak at $2\theta = 41.21°$ corresponds to the unstrained bulk BeO (002) diffraction peak position. It can thus be concluded that the film has the correct phase and is fully relaxed. The sharp diffraction peak at 41.7° is the sapphire (006) peak, marked with a *. The two additional minor peaks marked with diamonds are caused by the sample holder. In

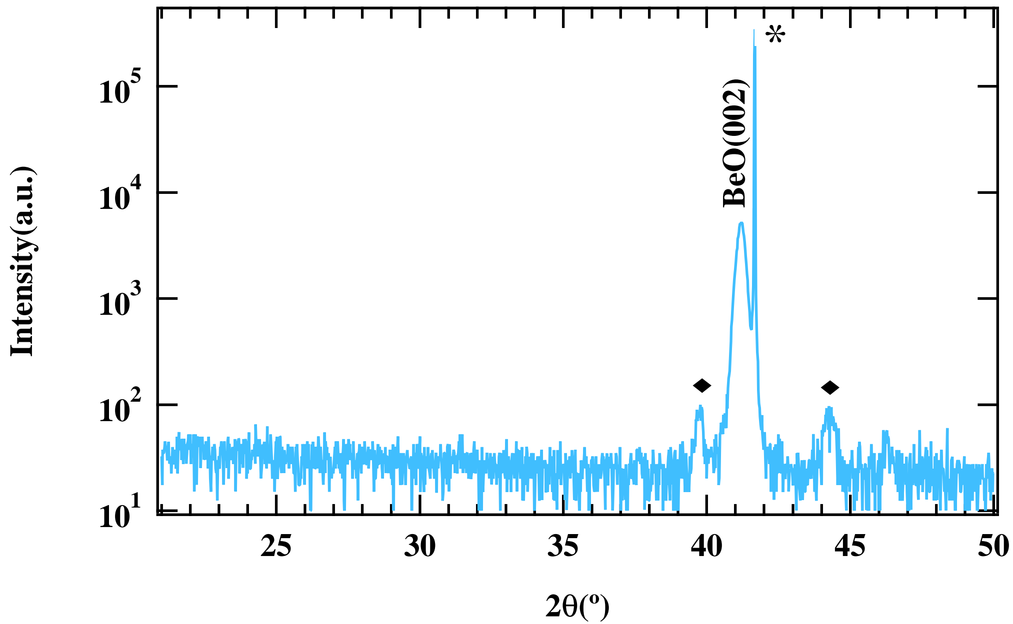

Figure 3.1: $\theta/2\theta$-scan of a BeO film deposited at 10^{-3} Torr and 500°C. (*) indicates a sapphire substrate peak. Additional peaks caused by the sample holder are marked by filled diamonds.

general, the diffraction peaks of the BeO film have unusually low intensities. This is caused by the very low x-ray scattering cross-section of Be atoms. Nevertheless, the presence of a heavier element, in this case oxygen, makes the detection of the crystal possible. The weaker intensity of the BeO peak can be explained by the low cross section consideration.

Surprisingly, a crystalline phase was obtained even when a film was deposited at room temperature and at low oxygen pressure. The diffraction pattern of a film grown without substrate heating at an oxygen pressure of 10^{-6} Torr is shown in Figure 3.2. Although a clear film peak was obtained, the peak position had shifted to a lower diffraction angle, which corresponds to an increase of the lattice parameter, probably due to the presence of defects, such as oxygen vacancies.

An overview of the $\theta/2\theta$-scans of BeO films grown under various process conditions is given in Figure 3.3. The crystallinity improved at high pressure and high growth temperatures. No crystalline phase peaks were observed for films

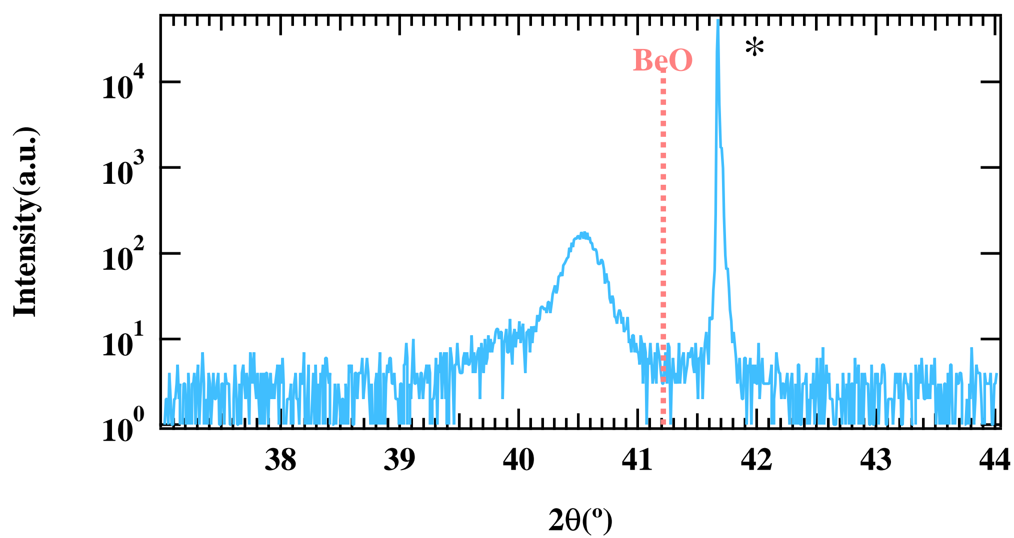

Figure 3.2: $\theta/2\theta$ scan of a BeO film deposited at 10^{-6} Torr and room temperature. (*) indicates the sapphire (006) substrate peak. The dashed line marks the expected BeO bulk diffraction peak position.

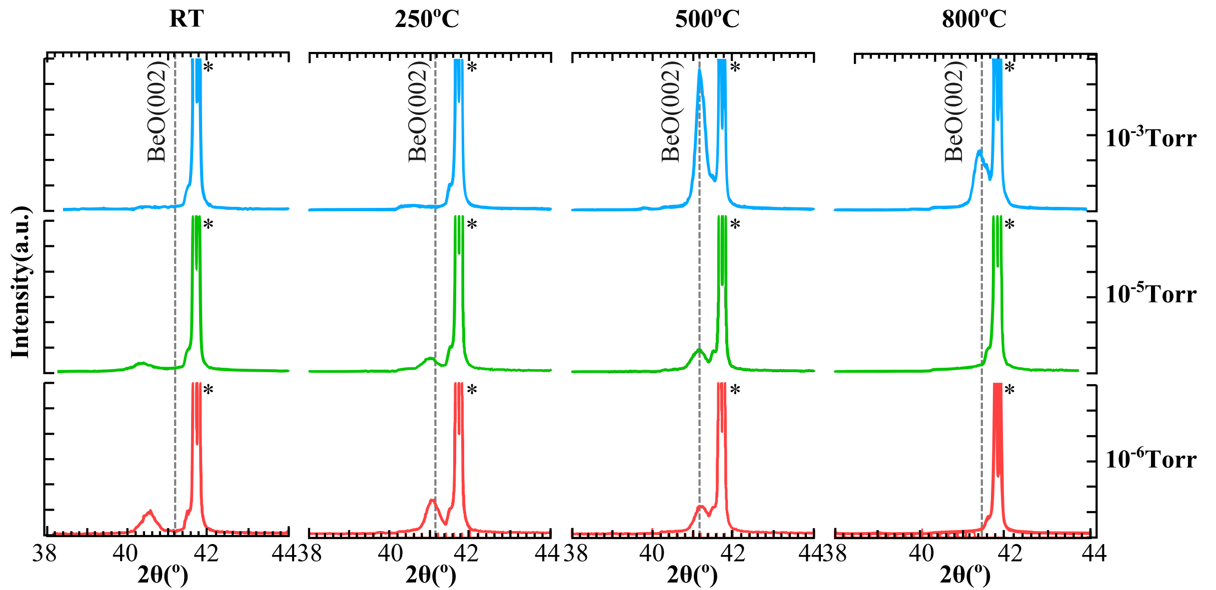

Figure 3.3: Overview of the $\theta/2\theta$ scans of BeO films grown under various oxygen pressures at different substrate temperatures. The (*) marks the sapphire substrate peaks.

grown at room temperature and high oxygen pressure. Likewise, no peak was observed in films grown at high temperature and low pressure. A valley of stability can therefore be defined, corresponding to intermediate growth temperatures and pressures where a crystalline BeO phase does form. A discussion of those results is presented in Section 3.7.2.

The BeO film peak intensity was high enough to consider the measurement of a ϕ scan, also known as a diffraction pole figure. The results are shown in Figure 3.4. The (112) peak of BeO and the (223) peak of sapphire were probed. The ϕ scan shows six peaks corresponding to the hexagonal structure of wurtzite BeO and corundum Al_2O_3. There is a $30°$ shift between the orientations of the BeO and sapphire lattices.

The lattice matching between BeO and sapphire can happen either at a higher order, where n unit cells of BeO match with m unit cells of Al_2O_3, or with a change of the relative in-plane orientation. To determine if the BeO films on sapphire are indeed epitaxial and to resolve the type of lattice matching, the relative orientation of the film and the substrate was investigated. The measurement of a

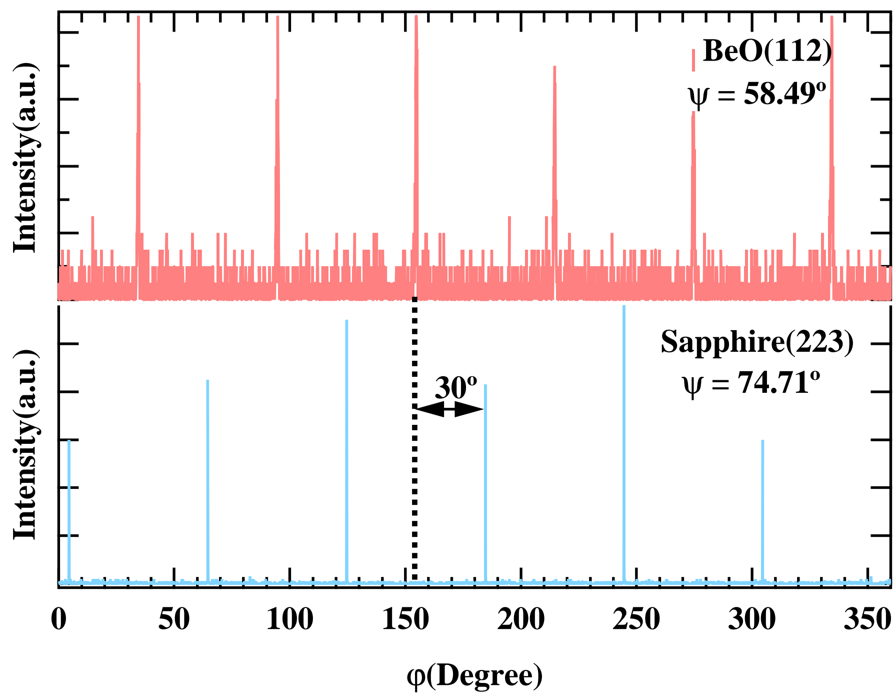

Figure 3.4: Φ scan of a BeO thin film grown on sapphire, showing a 30° in-plane rotation of the BeO lattice relative to the substrate.

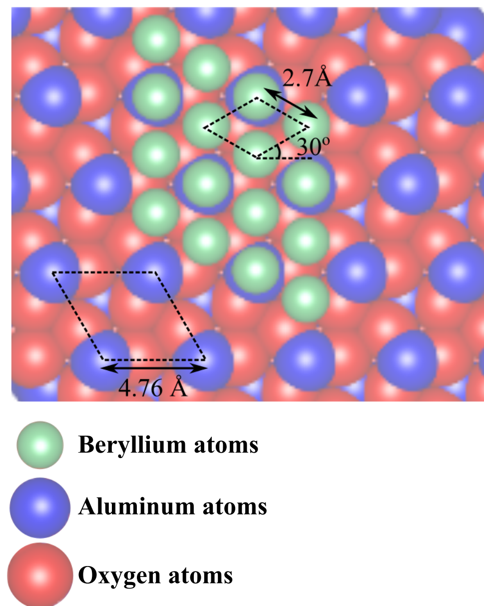

Figure 3.5: Relative in-plane orientation of the BeO thin film on a sapphire surface. Oxygen atoms are shown in red, beryllium in green, and aluminum in blue.

Φ-scan, shown in Figure 3.5 proved that the film is indeed epitaxial and showed that a shift of 30° exists between the BeO (112) peak and the sapphire (223) peak Φ scans. Therefore, there must be an angle of 30° between the in-plane directions of the (100) directions (Figure. 1.2) of BeO and sapphire. By looking at the in-plane atomic structure, this in-plane 30° rotation of lattices leads to a superposition of Beryllium atoms with the oxygen atoms of the sapphire lattice. In the non-rotated case, no reasonable superposition happens before very high matching orders. Therefore, the rotated configuration is more stable for crystal growth. Nevertheless, this superposition is reasonable only on a short length scale. After several unit cells, the mismatch becomes too large and the crystal lattice coherence between the film and the substrate is lost. The nanocrystalline morphology of BeO films grown on sapphire reinforces this interpretation, assuming that each grain represents a single crystal. Therefore, the crystallite size should be linked to the overall stability of the formation of a BeO grain on the atomically flat sapphire surface.

Figure 3.6 shows a $\theta/2\theta$-scan of a BeO film deposited on Nb:$SrTiO_3$(111). Good crystallinity was achieved and a strain of less than 0.3% was observed. The

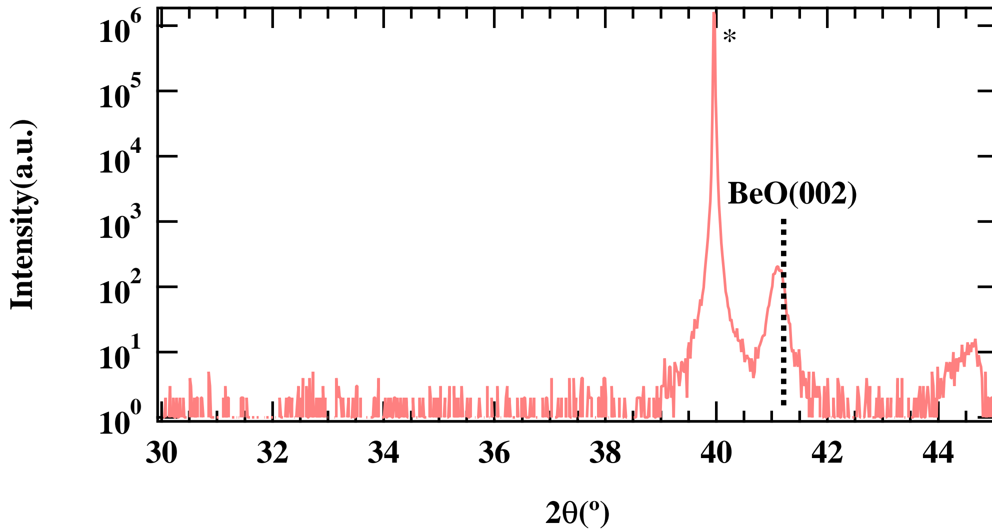

Figure 3.6: Diffraction pattern of a BeO film deposited on a Nb:$SrTiO_3$ (111) substrate. The Nb:$SrTiO_3$ (111)reflection is marked by (*).

relative orientation of the BeO thin film on Nb:$SrTiO_3$(111) is shown in Figure 3.7. The film has an in-plane aligned structure with the substrate.

Perfect alignment was observed for BeO films grown on $SrTiO_3$(111). Higher-order matching between the two lattices explained this orientation. The mismatch between 2 unit cells of BeO and 1 unit of $SrTiO_3$(111) is $M = 2.29\%$. Figure 3.8 shows the superposition of the two lattices.

3.3.1 Pole figure

A pole figure ($\psi - \phi$ scan) was measured for the BeO thin film deposited on sapphire. The 2θ angle was fixed at about $84°$ to probe simultaneously the BeO(112) and sapphire(223) reflection peaks. The observation of two sets of peaks, one corresponding to the BeO films, the other corresponding to the sapphire substrate was expected. The 6-folds reflection peaks of BeO were not observed at the expected $\psi = 58.4°$ value due to the high scanning speed. A low speed ϕ-scan was performed at the expected ψ to measure the BeO reflection peaks.(Figure 3.4)

A two unexpected sets of reflection peaks were observed at $\psi = 31°$ and $\psi = 17.5°$. The same pole figure was performed on a bare sapphire substrate and

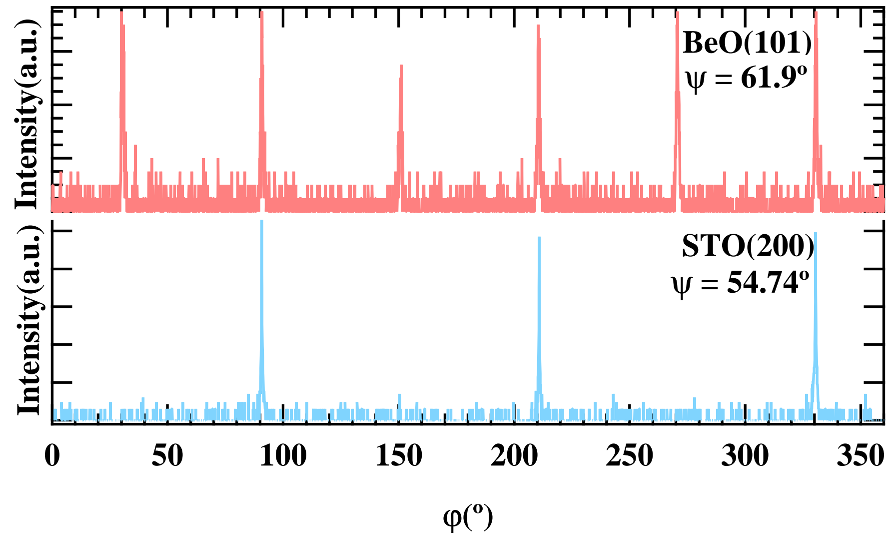

Figure 3.7: ϕ-scan of a BeO film deposited on a Nb:SrTiO$_3$(111) substrate.

two similar sets of peaks were also observed(Figure 3.9). A consistent assumption is the assigment of those two sets of peaks to the plans (1,1,9) (6-fold) and (1,0,10) (3-fold) of the sapphire. The corresponding value of the ψ angle are consistent with the observed value.

3.4 Morphology

The morphology of the film surface was analyzed by atomic force microscopy. Fig. 3.10 shows a typical AFM image of a BeO thin film. Small grains of approximately 90 nm are observed, which indicates that there is no stabilization of large crystallites. The sample film was grown at 10^{-3} Torr and $500°$C. Although the surface morphology appears polycrystalline, XRD analysis showed that the film is perfectly c-axis oriented.

3.5 Growth rate

The film thickness was measured for all of the deposited films. Figure 3.11 shows the evolution of the growth rate with temperature for different growth pressures.

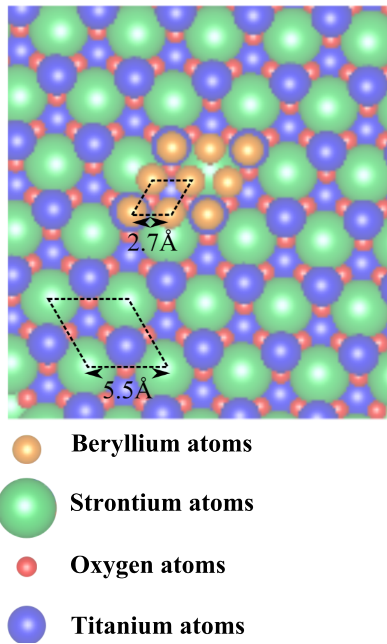

Figure 3.8: Relative in-plane orientation of the BeO thin film on a $SrTiO_3(111)$ surface.

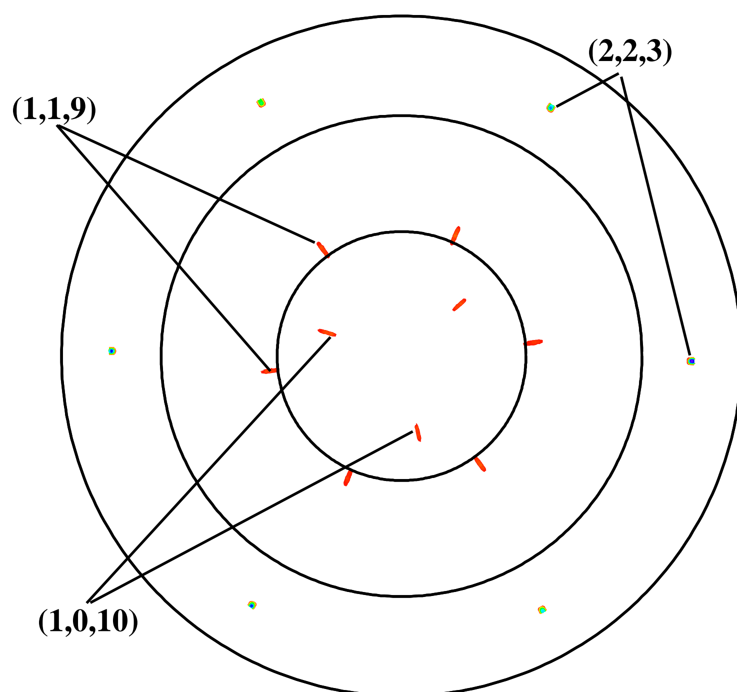

Figure 3.9: Pole figure of a bare sapphire substrate for $2\theta = 84.4$. The assigned reflections of sapphire are shown.

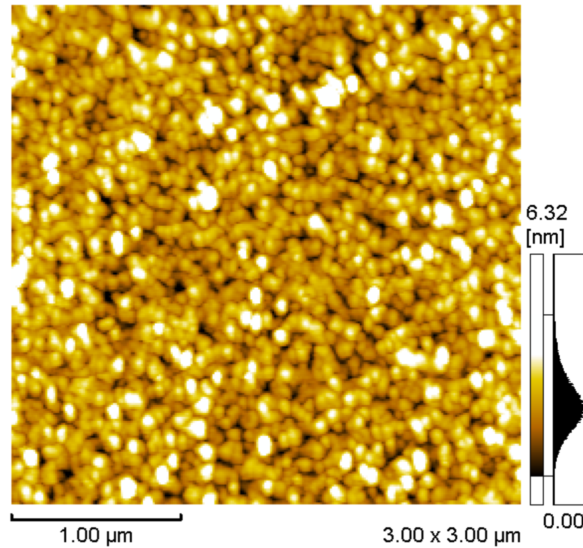

Figure 3.10: AFM image of a BeO thin film. The image size is $3\mu m \times 3\mu m$.

It is clear that the growth rate drops sharply at temperatures above 600°C and no films growth occurred at temperature above 800°C, despite a large number of deposition pulses. The effect of growth pressure on the growth rate is less important but there is a slight rate increase with the ambient oxygen pressure. This may indicate that the limiting factor for the beryllia film growth is the slow oxidation kinetics of Be atoms on the film surface.

3.6 Plume dynamics

Time-of-flight (TOF) plume content analysis experiments were performed for various target-to-sample distances and laser fluences in order to confirm the validity of the purely kinetic particle model that was introduced earlier in Section 2.3.4. The square root dependence of the flight time on fluence and the linear dependence on distance were observed. Figure 3.12 presents a typical TOF measurement result. The laser trigger point is shown in the Figure. The oscillations that follow the laser trigger are due to the high electrical field generated by the excimer laser. The time profile shows two current peaks, occurring at approximately

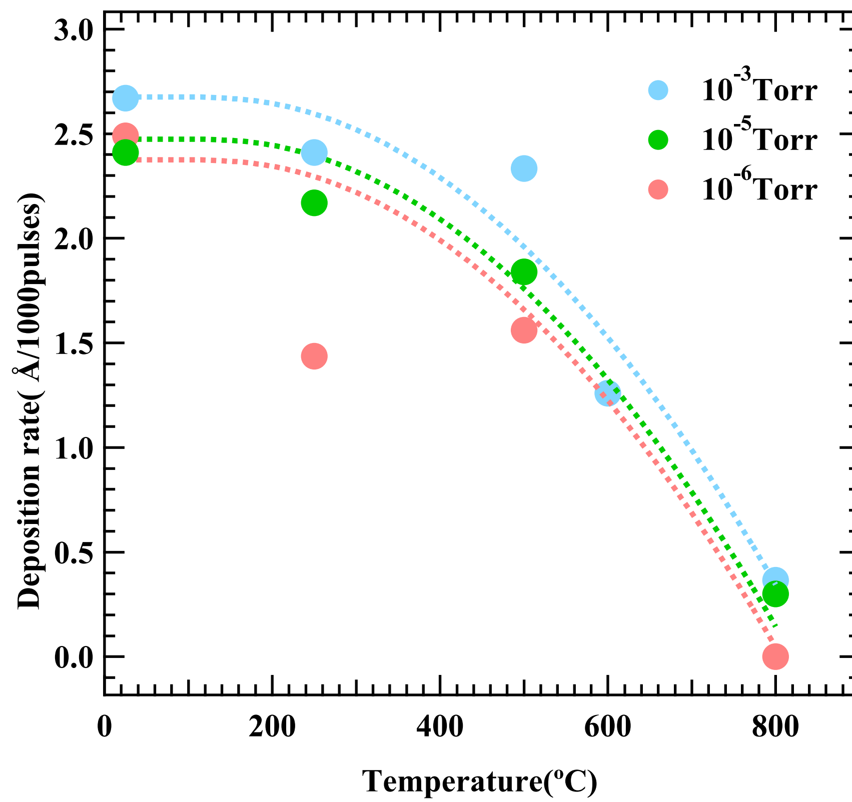

Figure 3.11: Growth rate of BeO thin films as a function of temperature for growth on sapphire substrates at various ambient oxygen pressures.

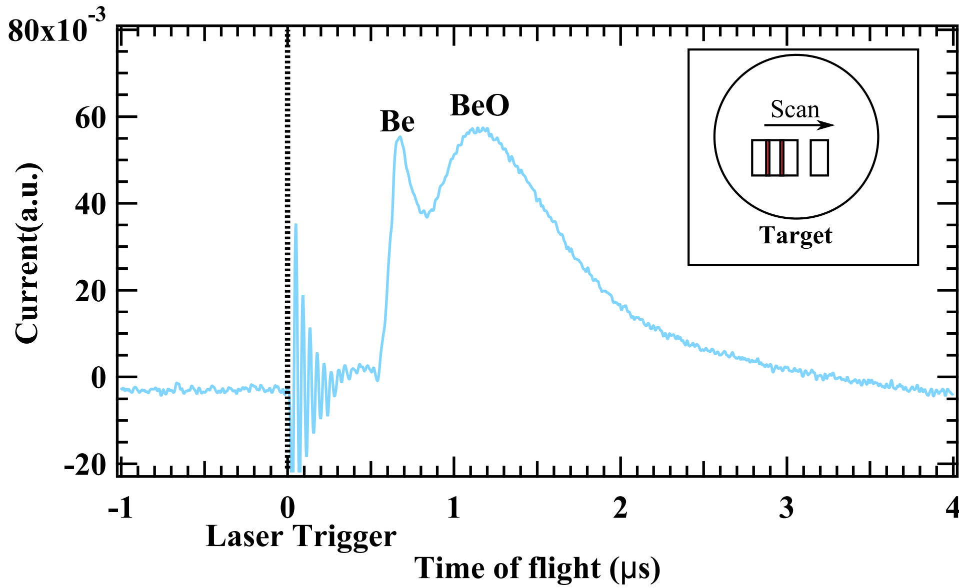

Figure 3.12: Time-of-flight spectrum of the ionized species in the ablation plume of a BeO target. The inset shows the overlap between consecutive ablation spots on the target surface when the target x-y scanning speed is too low.

0.67 and 1.15 microseconds after the laser pulse. The ratio of these two arrival times,$t_1/t_2 = 0.67/1.15 \approx m_{\text{BeO}}/m_{\text{Be}}$ corresponds to the ratio of the mass of Be^+ ions and BeO^+ clusters. Therefore, the plume can be concluded to consist mainly of those two species.

Figure 3.13 shows the effect of firing multiple ablation shots on a single spot on the target surface. The relative intensity of the Be and BeO peaks varies as a function of the ablation pulse count. Be ions become predominant after a few shots. This indicates that oxygen is lost from the surface layer of the target, which is harmful for achieving the correct oxygen stoichiometry in the film. Scanning of the target has to be fast enough to minimize the overlap between consecutive ablation spots on the target surface. This requirement is difficult to meet due to the high-frequency ablation, typically done at 100 Hz. If the laser firing is stopped for a few tens of seconds, ablating the same spot on the target again shows a recovery of the BeO peak intensity. The target oxidation therefore has to be fast enough to match the scanning speed of the target. The inset of Figure 3.12 shows the overlap between laser ablation pulses if the target scanning speed is too low to guarantee

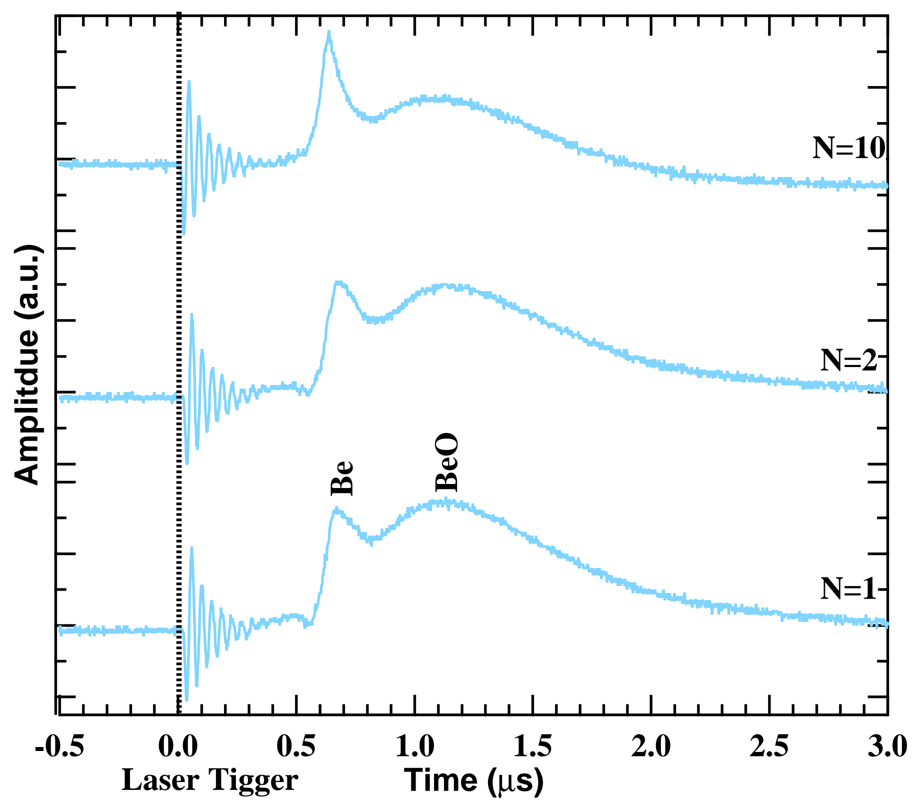

Figure 3.13: TOF measurement of selected laser shots fired on the same spot of a BeO target at 10^{-6} Torr and a laser fluence of 0.6 J/cm^2. The shot index N is shown for each TOF spectrum.

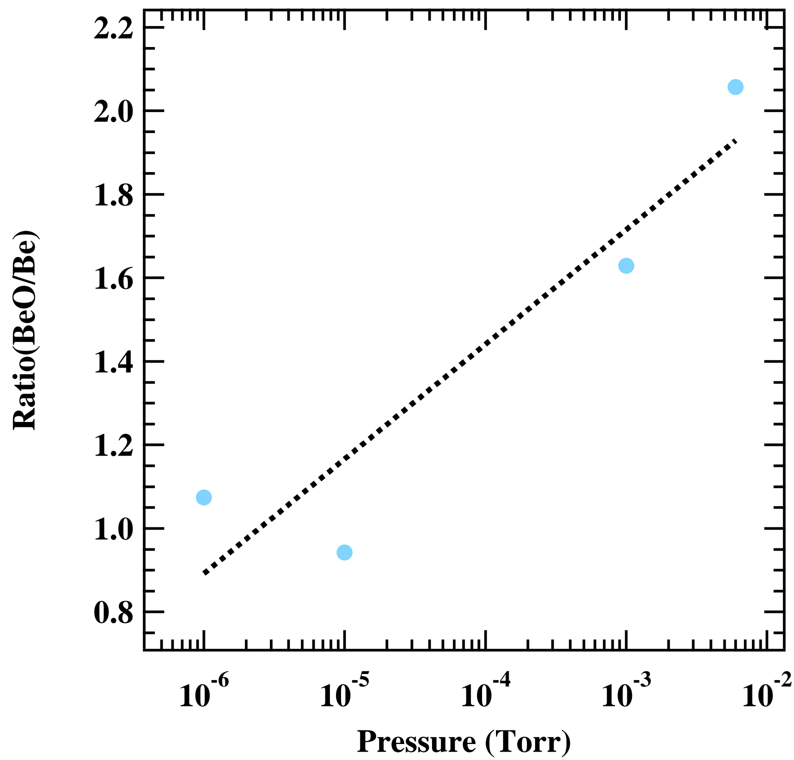

Figure 3.14: Ratio of Be and BeO species in the ablation plume for various ambient oxygen pressures.

non-overlapped ablation spots, resulting in Be-rich evaporation.

Figure 3.14 shows that ablation at higher oxygen pressure limits the intensity of the Be peak. A better re-oxidation of the target is due to the higher concentration of oxygen.

3.7 Discussion

3.7.1 Room temperature growth

It was shown in the previous Section that a crystalline thin film of BeO could be grown on a sapphire substrate. Other materials have been reported to grow at room temperature [38, 39, 40]. It has been argued for nitrides (AlN, InN, GaN)

[41] that the enhanced kinetic energies of the adatoms delivered to the film surface in the PLD process improve the migration length of the film precursors and promotes crystalline growth. The loss of crystallinity at room temperature for higher ambient oxygen pressures can thus be explained by the influence of the oxygen pressure. A higher oxygen pressure thermalizes the plasma in the ablation plume, reducing the average kinetic energy of the adatoms. Higher ambient pressures also reduce the surface diffusion length. Surface adatoms that cannot diffuse to optimal crystallization sites form clusters with low crystallinity. Even if nanoscale crystallites are present, it may be difficult to prove by simple XRD measurements due to strong peak broadening and loss of diffraction intensity for nanoscale crystallites. However, even amorphous films of this type may be useful as diffusion barriers, as described in the introduction, but were not considered further in this work. Regardless of growth pressure, better crystallinity was obtained at higher substrate temperatures. For lower pressures, the shifted film peak obtained in room-temperature growth gradually reached the bulk value as the growth temperature was increased. For higher background pressures, the crystalline phase started to appear for temperatures above 250°C.

3.7.2 BeO growth instability

For growth temperatures above 600°C, no film could be successfully grown. Indeed, as shown previously, the deposition rate drops off when the substrate temperature exceeds 600°C, making the formation of a thin film impossible. The absence of a film on the surface of a substrate possibly originated from the desorption of the deposited atoms at a higher rate than the deposition rate. Several mechanisms can explain the desorption. The most likely candidate would be the re-sputtering of surface atoms by the energetic species in the ablation plume, where kinetic energies in the 10 eV range are possible. A less likely candidate is the evaporation of the surface species by sublimation. The evaporation of various oxides can be forecast by looking at the vapor pressure of the involved species. The vapor pressure of BeO is quite low even at very high temperatures. The vapor pressure of beryllium metal, however, is 10^{-8} Torr at 707°C, 10^{-6} Torr at 832°C, and 10^{-4} Torr at 997°C. Those values correlate well with the observed growth temperature limit. The analysis of the plume composition by the time-of-flight method showed that beryllium metal atoms form a large part of the deposited species. A slight deposition rate increase was also observed for increased oxygen pressure at a fixed growth temperature. The conclusion from these experiments thus is that most likely Be atoms desorb from the film or substrate surface if the

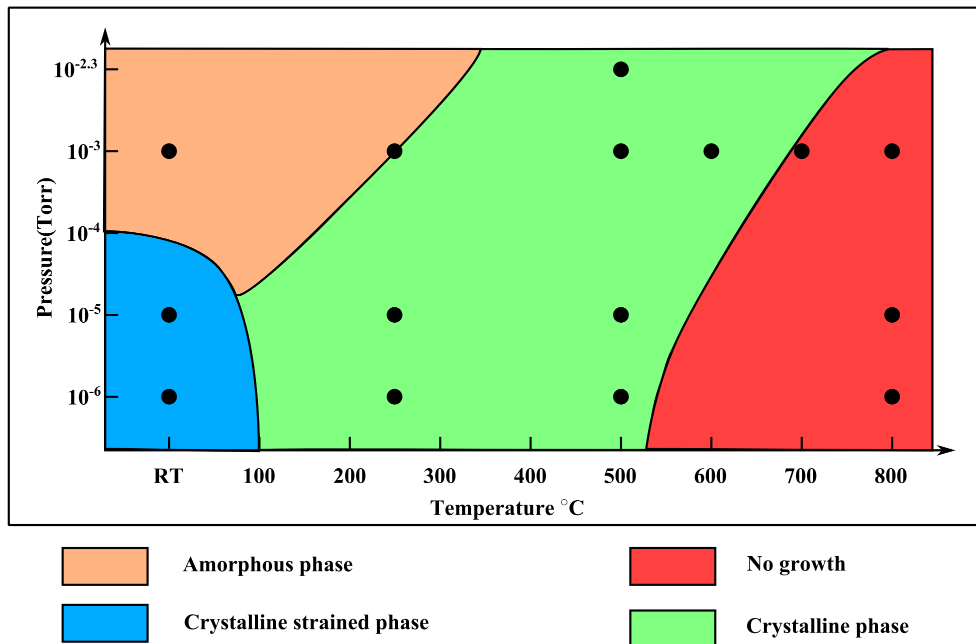

Figure 3.15: Growth stability diagram of BeO thin film growth on sapphire.

oxidation kinetics are too slow to form a stoichiometric BeO phase before the arrival of the next deposition pulse of high-energy particles.

Figure 3.15 presents a overview of the growth stability diagram. The blue area corresponds to a crystalline strained phased grown at low temperature and low pressure. Only amorphous growth was observed in the orange region. A crystalline unstrained phase was found in the green zone. Finally, the red area is the instability part of the phase diagram where no film could be grown.

3.8 Pyroelectric measurement

Figure 3.16 shows the results of a pyroelectric measurement of a BeO film. The sample was periodically heated with laser light that was chopped at a rate of 2 Hz. The light intensity profile is shown at the top of the Figure. A high laser intensity would result in a rapid increase of the sample temperature, followed by rapid cooling when the laser beam is turned off. The pyroelectric current is observed immediately after the start and end of each heating laser illumination pulse. The

magnitude of the current is proportional to the change of the sample polarization in response to the rapid temperature change. The quick increase of temperature therefore creates a positive spike of current followed by an exponential decrease. The same process repeats, but with the opposite polarity during the cooling phase. While the exponential decay of the pyroelectric current is caused primarily by the exponential temperature increase of the illuminated area, heat conduction into the substrate and the time constant of the current measurement circuit also affect the result. There is also a slight current offset between the illumination and dark periods, indicating the presence of a photocurrent component. This is commonly observed in pyroelectric measurements. Even for samples where no direct bandgap excitations can occur due to the low laser photon energy, carriers can still be generated at the top electrode or bottom substrate interfaces.

A capacitance - voltage (C-V) measurement was done with the same sample. Figure 3.17 shows that the film capacitance is independent of the applied voltage. A capacitance of 1050 pF was measured. By considering a simple planar capacitor model, the capacitance can be expressed as: $C = \epsilon_R \epsilon_0 A/d$, where ϵ_0 is the dielectric permittivity of vacuum, ϵ_R is the relative permittivity, A is the surface area of the capacitor and d is the thickness of the capacitor. A relative permittivity of $\epsilon_R = 7.5$ was derived, which is consistent with the values found for thin film BeO.[42]

Figure 3.18 presents a current-voltage characteristic of a Nb:$SrTiO_3$/BeO/Pd heterostructure. The BeO film thickness was 200 nm. The device functioned as a diode. It was in a blocking state for negative voltages and showed a low-resistance state for biases above 0.5 V. Due to the measurement geometry, it is possible that the measurement is affected by pinhole or grain boundary defects in the film, showing an abnormally low resistance at high bias.

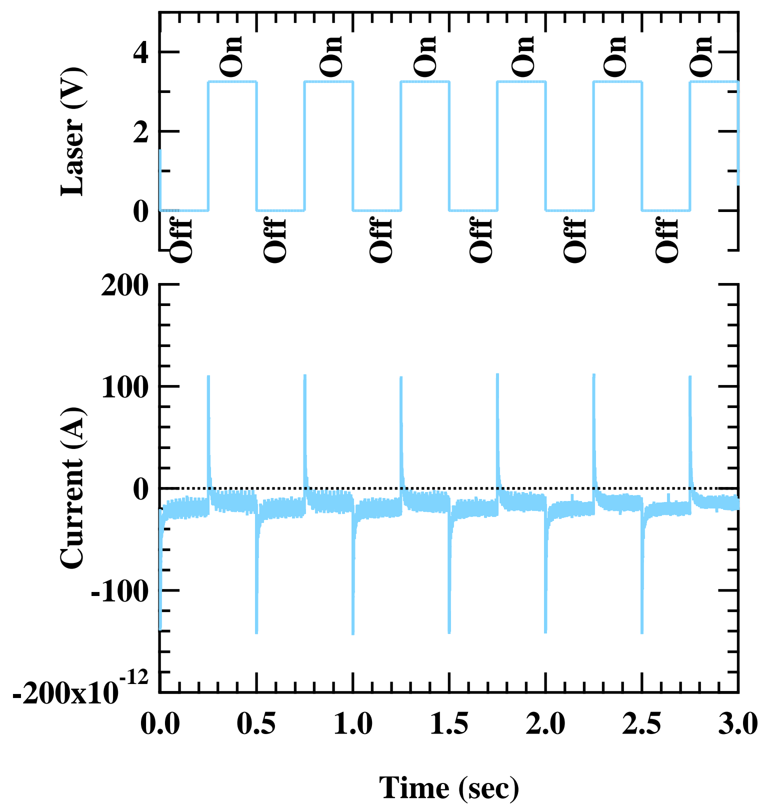

Figure 3.16: Pyroelectric response measurement obtained at a laser chopping rate of 2 Hz.

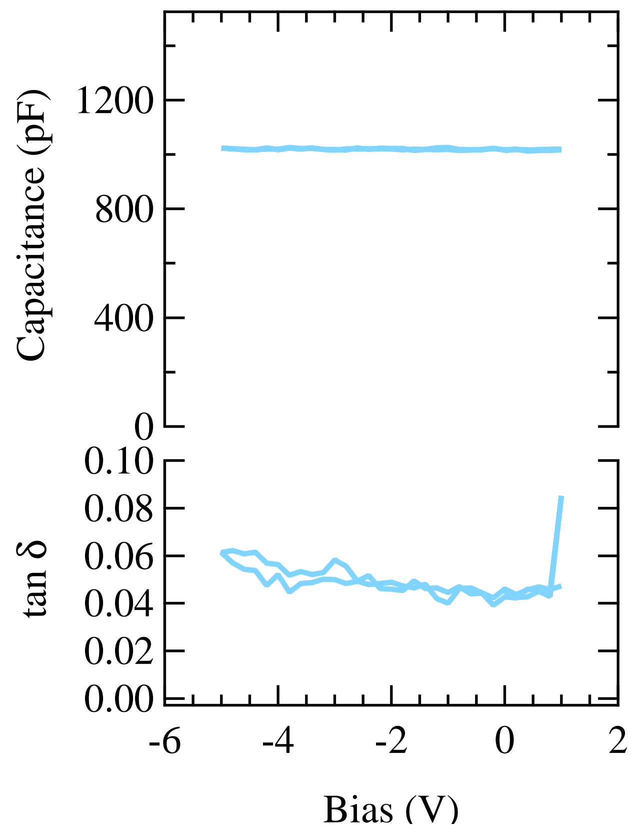

Figure 3.17: A C-V curve of a BeO film and the loss tangent, measured at 600 Hz

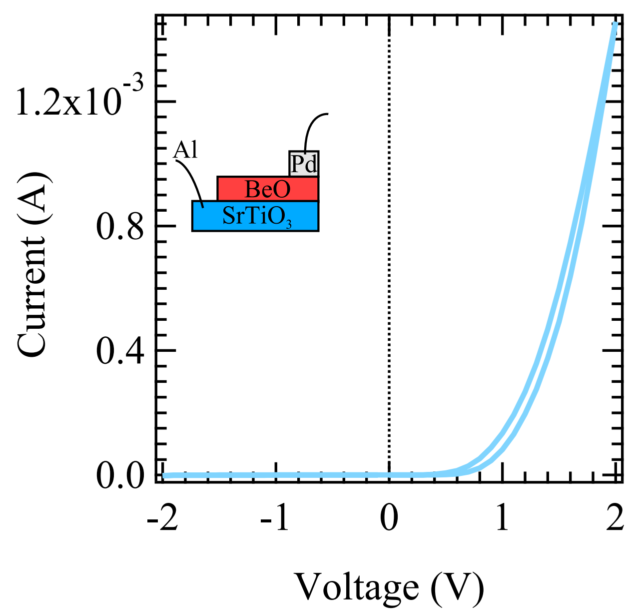

Figure 3.18: IV curve of BeO film.

Chapter 4

Band gap tuning by alloying BeO and ZnO

4.1 Introduction

In this Chapter, the growth of BeO alloys with ZnO will be discussed. $Be_xZn_{1-x}O$ films were grown with a crystalline phase on a substantial range of the composition. The determination of the Be content by X-ray diffraction is put into perspective with the expected Be-content as a difference was observed. Based on the symmetrical $\theta/2\theta$ scan, the evolution of the crystallinity was investigated as a function of Be-content. The origin of the crystal quality decrease will be discussed. A model is suggested to explain the structural change due to the incorporation of beryllium atoms in ZnO. The transmission and the reflectivity measurement have confirmed the possibility of band gap energy engineering. A relation between the $Be_xZn_{1-x}O$ film band gap energy and the Be content x was derived.

4.2 Crystallinity and Be content

4.2.1 Determination of the concentration

As shown in Section 2.2.3 it is possible to control the composition of a film by ablating successively two different targets. If this is done at an elevated temperature, an alloy phase can be formed, similar to traditional bulk ceramic synthesis.

Accurate growth rate measurement for each target material is necessary for composition control in such binary alloy materials In case of the BeZnO alloy, it is thus necessary to measure the growth rates of ZnO and BeO. The determination of the growth rates was done by depositing several films of pure ZnO or pure BeO on sapphire at room temperature and 10^{-6} Torr. The number of ablation pulses was fixed at 500,000 in order to have a good estimation of the film thickness and the growth rate.

The film thickness was measured using a profilometer. The growth rate per 1000 pulses was computed for both BeO and ZnO and converted to more convenient units for deposition, namely unit cells per 1000 pulses. The values are given in Table 4.1. The general formula for calculating the number of laser pulses required to deposit x unit cells of a compound is then $N = \frac{1000x}{\kappa}$, where κ is the growth rate.

For instance, to fabricate a single unit cell layer of an alloy film with a 20% Be content, it would be necessary to ablate $1000 * 0.8/4.4 = 182$ pulses of ZnO and $1000 * 0.2/0.43 = 465$ pulses of BeO. The main source of error in these calculations is the large margin of error in the growth rate measurement. However,

this growth rate error should lead to a constant shift of the effective composition compared to the expected value.

It is assumed that the alternate deposition of two compounds behaves similarly to growing a film from a single mixed-composition target. This assumption may prove to be incorrect if there is significant re-sputtering occurring at the film growth front.

Material	Growth rate (u.c./k pulses)
BeO	0.43
ZnO	4.44

Table 4.1: Growth rates of BeO and ZnO at room temperature and 10^{-6} Torr.

The composition of the films needs to be checked after deposition in order to verify that the actual Be/Zn ratio matches the expected ratio. Since x-ray diffraction was used to measure the crystallinity of all samples anyway, the easiest method for verifying the film composition was to use Vegard's law. This is an empirical law that links the cell parameter of an alloy with the lattice parameters of the two compounds used to make the alloy.[43] For $\mathrm{Be}_x\mathrm{Zn}_{1-x}\mathrm{O}$, the relation can be written as:

$$c_{\mathrm{Be}_x\mathrm{Zn}_{1-x}} = x * c_{\mathrm{BeO}} + (1-x) * c_{\mathrm{ZnO}}, \tag{4.1}$$

where $c_{\mathrm{Be}_x\mathrm{Zn}_{1-x}}$, c_{BeO}, and c_{ZnO} are the lattice parameters of the alloy, pure BeO, and pure ZnO, respectively. It has been shown that the $\mathrm{Be}_x\mathrm{Zn}_{1-x}\mathrm{O}$ system follows this relation[19]. However, there are also limits of the law. Vegard's law has been successfully applied to different alloys [44] but it fails for others [45]. The law is based on a linear evolution of the cell parameter. Therefore, an error in the determination of the alloy c-axis leads to an incorrect estimate for the composition. The law only works if there are no major structural transitions in the alloy composition phase space and if the alloying is substitutional, i.e., the effects of vacancies or interstitials can be ignored.

The cell parameters of the alloys are generally obtained by XRD measurement, which probes only the crystalline part of the film and does not give information on the possible presence of non-crystalline or nanocrystalline phases. Therefore, Vegard's law applies only to the crystalline part and gives information on the relative composition in the crystalline part of a film only. If the assumption discussed here are not fulfilled, a deviation from the linear lattice parameter interpolation

would be observed. Generally, Vegard's law may be expected to work well for close to the end compositions in the alloy phase diagram[46] and deviation may appear above a certain critical composition.

The change of the cell parameter is due the substitution of one of the cations by another. It thus shows the level of actual alloying of the two cations in the host lattice. The presence of interstitials is not probed and lead to an error in the composition calculation.

Furthermore, in case of thin films, Vegard's law has an additional limitation. A film grown on a mismatched surface tends to be strained. In first approximation a biaxial in-plane strain imposed by the substrate on the film results in an extension of the out of plane lattice parameter, which is probed by x-ray diffraction. The variation of the out of plane parameter thus includes two contributions: the actual alloying effect and the strain effect. The law cannot be applied in this case. Therefore, Vegard's law has to be carefully applied in the case of thin films and it is necessary to verify its validity.

Figure 4.1 compares the expected Be content with the calculated value obtained from the XRD data by Vegard's law analysis. The dashed line marks the ideal behavior, which the data points follow up to a Be content of about 6%.

The beryllium content matches the expectation for doping levels of up to 6%. Between 6% and 8%, a loss of beryllium is observed. Then, a strong positive deviation of the Vegard's law is observed above 8%. The measured Be content shows a sudden jump to about 75%.

As shown in Section 2.2.3, a periodic temperature modulation method was used in order to obtain films with better crystallinity. The films were deposited with a two-step temperature program. One unit cell layer of an alloy was deposited on a substrate at low temperature. This step should guarantee a correct composition of the film. Side-effects, such as re-sputtering or sublimation, should be reduced by the low substrate temperature. The film quality is improved by a short annealing at high-temperature after the growth of each unit cell layer. Sublimation effects are considered to be negligible during this high temperature annealing step. A sudden jump of Be content is also observed, for films deposited by a temperature modulated interval methods. The jump is shifted to higher expected Be content in comparison with the films deposited without interval temperature modulation.

The difference between the expected and measured compositions can be explained in different ways. A clear possibility is that Vegard's law could give a wrong value for the content. As was already discussed earlier, the presence of an amorphous component or interstitials could leads to a significant divergence in

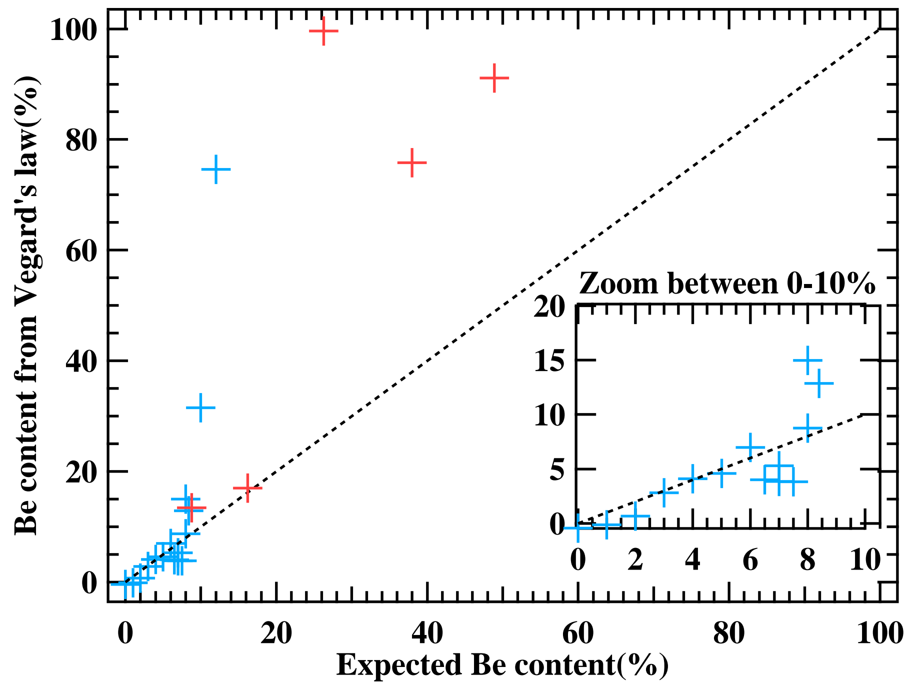

Figure 4.1: Correlation between the expected Be content calculated from the growth rates and the Be content obtained from Vegard's law analysis of the x-ray diffraction peak positions for two different growth methods. The inset shows an enlarged view of the low Be content range of up to 10%. Data for thin films grown by PLD without temperature modulation are marked with blue crosses. The red crosses correspond to films grown by the temperature modulation technique. The expected behavior is represented by the dashed lines.

Material	Cell parameter (Å)	Compressibility (10^{-3} GPa^{-1})
BeO	4.3772	4.1
ZnO	5.20661	22

Table 4.2: The c-axis parameters and volume compressibilities of BeO and ZnO.

the calculated Be content. On the other hand, re-sputtering or sublimation of one compound during the growth could also explain the observed difference. For example, comparison of compositions calculated for $Be_xZn_{1-x}O$ alloys from XRD and XPS data have shown that above an alloying limit the lattice parameter no longer depends on the Be content while the Be spectral weight in x-ray photoelectron spectra continues to increase. This discrepancy has been explained by assuming that above a certain composition limit, beryllium atoms start to populate interstitial crystal sites due to the small size of the beryllium ions.[47] The ionic radius for Be^{2+} and Zn^{2+} radii are 0.27 pm and 0.6 pm, respectively.

For Be compositions between 6% and 8%, the apparent drop of Be concentration in Figure 4.1 corresponds to a lack of substitutional beryllium atoms at the original Zn sites. Several models have been developed to try to predict the value and sign of the deviation.[48] The deviation is usually explained by the difference of the structural parameters of two compounds, such as the unit cell parameters and compressibility. The main argument is that a similarity in bond lengths of two compound should ease alloying. For BeO and ZnO, the compressibility and the unit cell parameters exhibit significant differences (table 4.2). The model of Fournet [49] predicts correctly a negative deviation.

Large composition deviations occur when the Be doping level in ZnO exceeds 8%. This shows that alloy phases in the middle of the composition pahse diagram appear to become structurally unstable. It has been shown that the miscibility gap increases when alloying is attempted between materials with a large atom sizes difference.[50]

In principle there are a number of methods that can be used to measure the precise composition of a thin film. An Energy Dispersive X-ray (EDX) measurement was therefore attempted. In an ideal case, several characteristic x-ray peaks are observed for each element in a sample. Due to the relatively large, micron-order probing depth of EDX, the measurement integrates over the whole thin film volume. However, it appeared that the characteristic X-ray energy for Be is too low to be resolved in the EDX spectrometer available at ISSP. An alternative technique would be to measure X-ray Photoelectron Spectra (XPS), although it would

be difficult to determine the true bulk composition of a film due to the shallow escape depth of photoelectrons.

4.2.2 Crystal structure

As shown in figure 4.2, a crystalline phase was successfully obtained for $Be_xZn_{1-x}O$. The observed peak corresponds to the wurtzite (002) reflection. The peak position shifts to higher diffraction angle, i.e., smaller lattice parameter as the Be content x increases. In other words, the c-axis parameter showed the expected decrease when more Be atoms were incorporated in the lattice. The increase of Be content also resulted in a reduction of the diffraction peak intensity and a strong broadening of the (002) peak. No crystalline film was observed above Be doping levels of 20%. This limit corresponds to the composition gap where no crystalline phase can be formed. The instability is discussed in more detail below. A crystalline phase was recovered when the Be content increased above 80%. As for the lower doping region, the crystallinity improved as the thin film alloy composition approached pure BeO.(Figure 4.3)

A plot of the Full Width at Half Maximum(FWHM) of the (002) peak in Figure 4.4 shows two minima close to either end composition and maximum appears in the mid-range. For both BeO and ZnO end of the diagram, the crystallinity starts to recover for composition below a doping level of 20%. Therefore, it appears that it is possible to alloy BeO with ZnO only in limited ranges close to the end compositions.

The instability of the mid-range compositions was also observed through the appearance of phase segregation. Indeed, when films with an expected composition close to the solubility limit of 20% were deposited, in some case the XRD-patterns showed two film peaks (Figure 4.5). The higher angle peak corresponds to a Be-rich alloy and the other to a Zn-rich alloy. The two peaks correspond to apparent Be compositions of $x = 7.63\%$ and $x = 95.6\%$.

A thin film was deposited at room temperature with an expected 50% Be content. No crystalline phase was observed by XRD measurement. Annealing such a film at high temperature may promote alloy phase formation if the phase segregation observed in the PLID films was driven either by the low oxygen pressure or by some type of kinetic processes. The film was therefore annealed for 4 hours at 1200°C. This treatment did not produce a crystalline phase. Neither alloying nor phase segregation was observed. This indicates that the amorphous alloy phase is stable even at very high temperatures, suggesting that highly Be-doped ZnO may work as an excellent barrier oxide in floating-gate type devices.

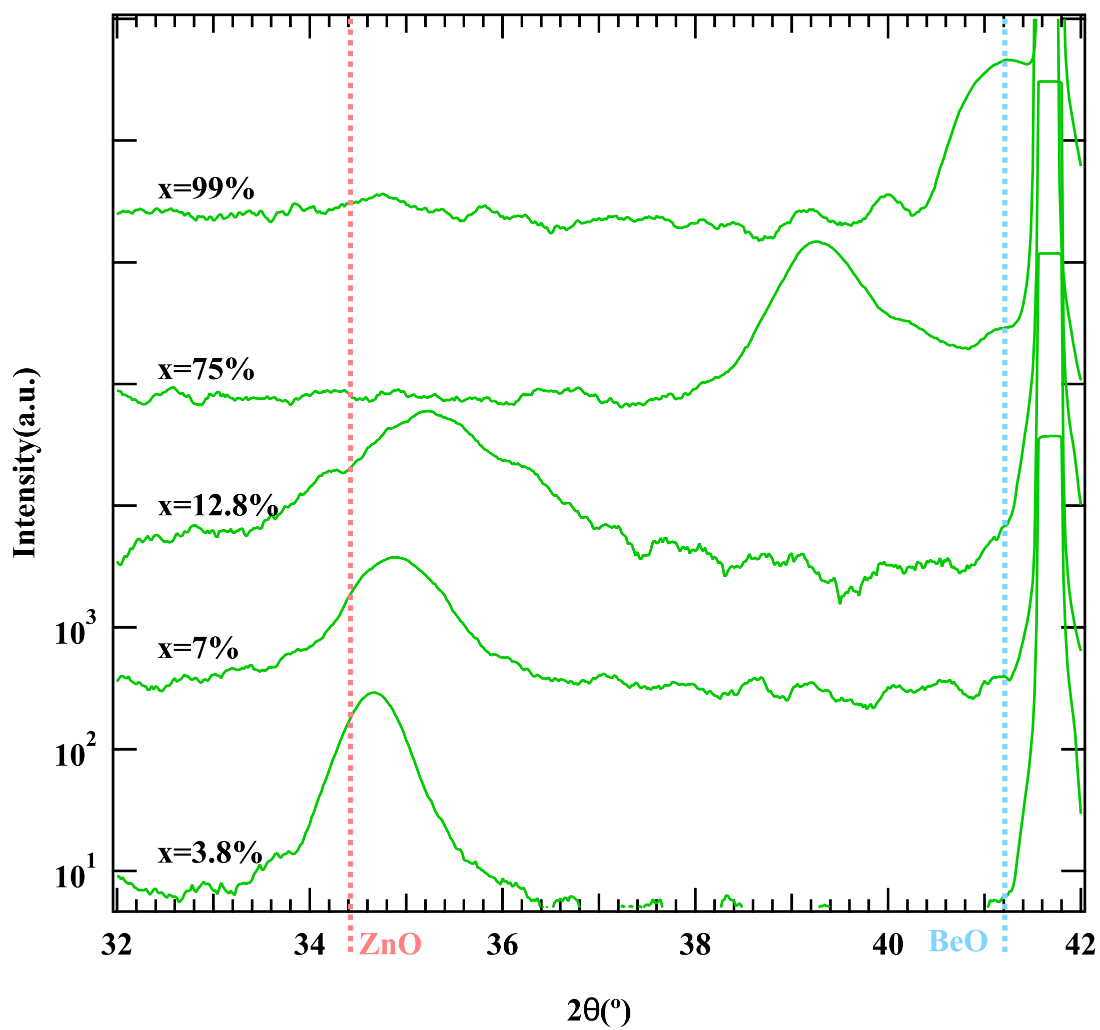

Figure 4.2: XRD patterns for $Be_xZn_{1-x}O$. The peak positions of BeO(002) and ZnO(002) are shown for reference.

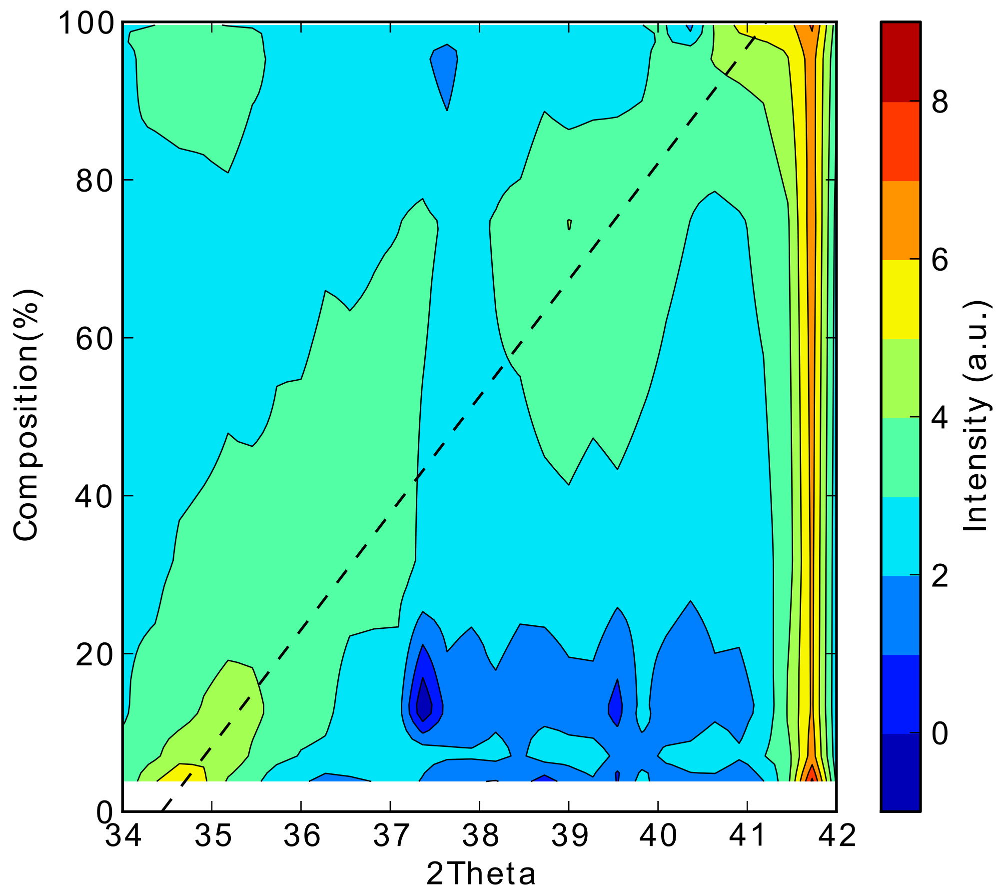

Figure 4.3: Contour plot of the XRD intensity of the $Be_xZn_{1-x}O$ (002) peak. The dashed line indicates the expected peak position according to Vegard's law.

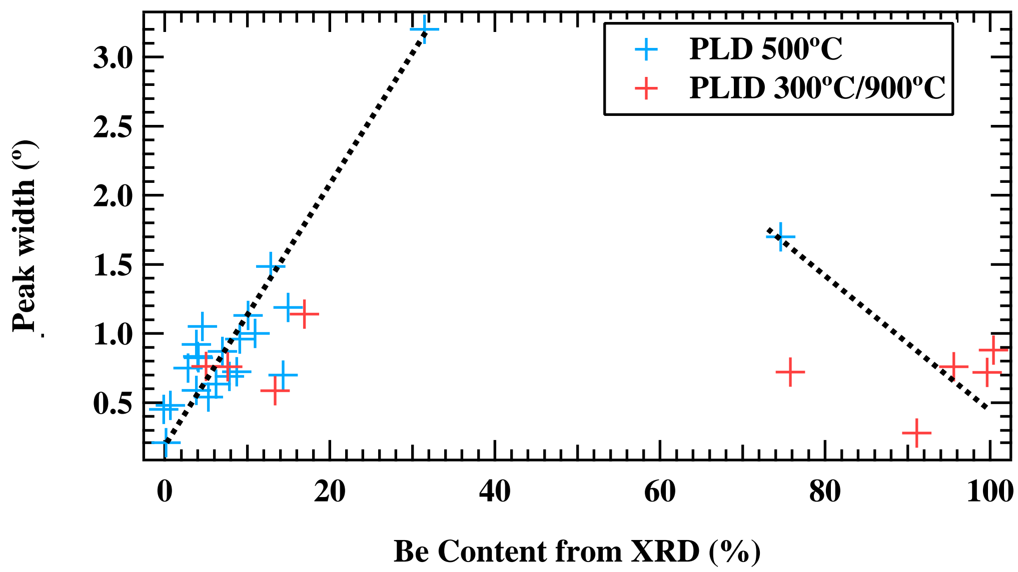

Figure 4.4: Evolution of the $Be_xZn_{1-x}O$ (002) peak width with the Be content. The dashed lines are guides for the eye. PLD refers to films grown at a constant temperature. PLID refers to films grown by the temperature modulation technique.

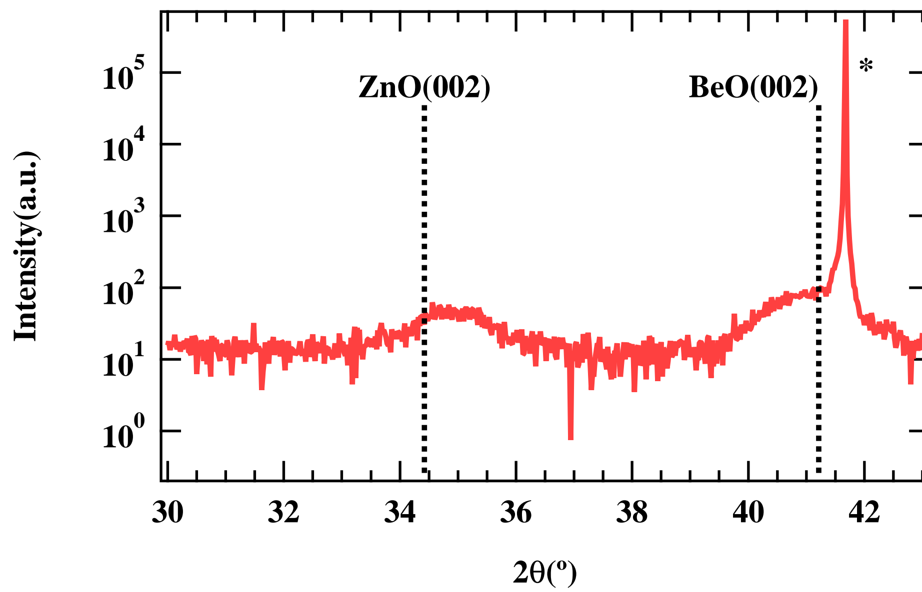

Figure 4.5: An XRD pattern of an alloy film deposited by temperature-modulated PLD $300°$/$900°$ at 1 mTorr for an expected concentration of $x = 19.1\%$. (*) marks the sapphire (006) peak.

The reasons for the stabilization of the two end compositions is still under question. Indeed, for the Zn-rich side, the alloying seems to follows the expectation of the Vegard's law. This behavior is expected for low compositions. The deficiency of beryllium atoms in the range $6-8\%$ could be explains by the filling of the interstitial sites. Indeed, the small size of beryllium should favor the formation of interstitial defects, leading to a loss of beryllium from the wurtzite cation site. However, it is difficult to probe the cause of the decrease of the lattice parameter in the $6-8\%$ Be range. For the jump of compositions from Zn-rich to Be-rich, the excess Zn atoms appear to occupy interstitial sites.

The size of the cell volume is greatly influenced by the bond length of Be-O and Zn-O. The Be-O and Zn-O bond lengths are, 1.64Åand 1.95Å, respectively.[51] Based on a comparison of formation energies, BeO (-142 kcal/mol) is more stable than ZnO(-83kcal/mol).[52] Therefore, the substitution of Be at the Zn site should be more favorable and the cell parameter should shrink.

A first-principles calculation has considered two types of substitutions and two types of interstitial sites.[53] As expected, the substitution of Zn atoms by Be leads to a decrease of the cell volume due to the decrease of both in-plane and out-of-plane parameters. The two interstitial sites are energetically favorable and decreases the cell volume (the a-axis shrinks and the c-axis expands). A similar results has been obtained for BeO doped by Zn [54]. In this case, Zn^{+2} substitution in BeO has been shown to be more favorable (-20.83eV) than the formation of Zn^{+2} interstitials (-17.59eV). However, Zn interstitials are favored for a lower Zn valence that may be induced by annealing. In this case the c-axis parameter is increased by the presence of Zn interstitials in BeO.[55] Figure 4.6 presents an overview of the possible occupancies for the different sites. This distribution is consistent with the observed variation of c parameter in the alloy films.

Figure 4.7 shows that there are systematic variations in the alloy phase XRD peak width in the low Be doping range between 6% and 8%. In this range, a loss of substitutional Beryllium atoms was observed at the Zn site. The plot shows that together with a negative deviation from Vegard's law, a region with higher crystallinity appears at around 7% Be doping. The reason for this crystallinity enhancement may be the filling of interstitial sites. The ionic radius of beryllium is smaller than that of zinc. Therefore, as the substitution increases, the density of the unit cell decreases. The filling of interstitial sites could be a good mechanism to counterbalance the instability of a less compact structure. The presence of metastable compositions for the $Be_xZn_{1-x}O$ was predicted by a direct first principles computation (Figure 4.8). A metastable structure is eased due to its lower formation enthalpy and it should be coupled with a crystal improvement in com-

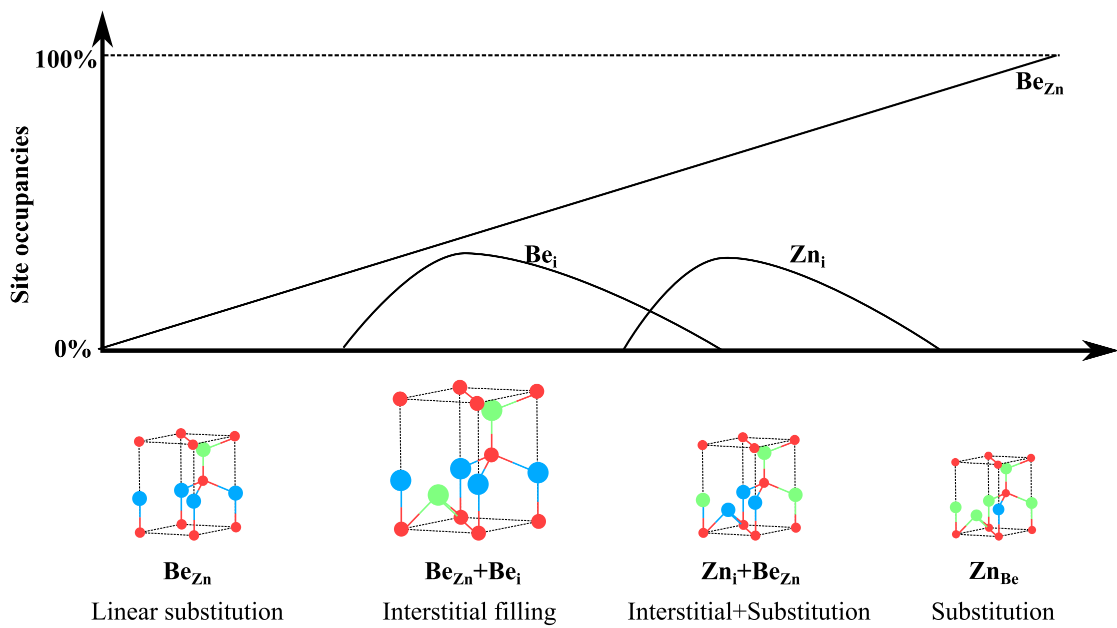

Figure 4.6: Evolution of substitutional and interstitial site occupancies and an illustration of the various defect sites.

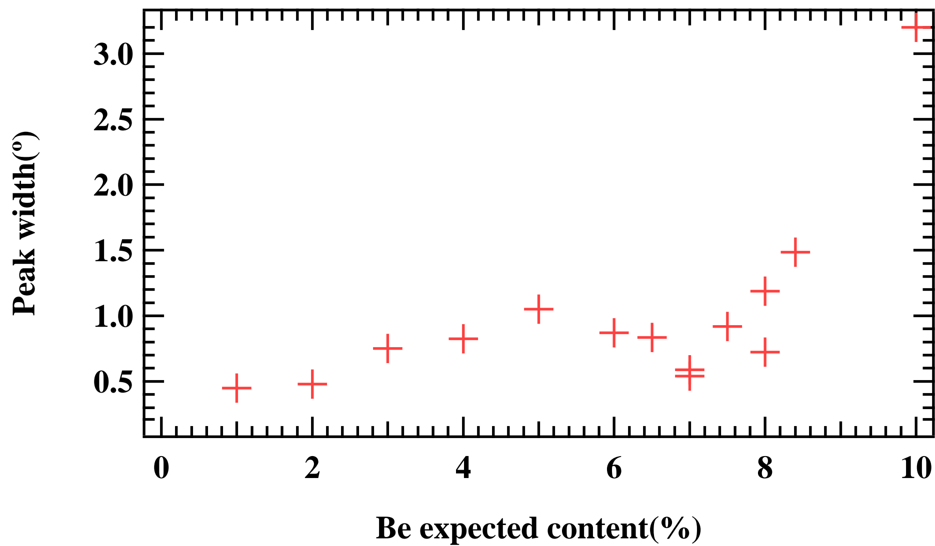

Figure 4.7: Width of the $Be_xZn_{1-x}O$ (002) peak as a function of the expected concentration, showing a possible stability region close to 7% Be doping.

parison with an less stable composition.

4.3 Morphology evolution

The evolution of film morphologies is illustrated b a set of AFM images in Figure 4.9 as a function of the alloy composition. For a composition close to pure ZnO, no visible grains can be observed. As the Be content increases, grains start to appears and once the Be content exceeds the solubility limit of about 20%, the grain size decreases again. Finally, the grain size increases again as the film composition approaches pure BeO, since the BeO phase can be stabilized on sapphire. For pure beryllia, the crystallite size is limited by the loss of long-range crystal matching.

The appearance and subsequent reduction of grain size is consistent with the instability of the intermediate compositions. Indeed, as stated previously, as the composition gets closer to the mid-range, the crystallinity decreases. A small grain sizes is an indication of poor crystallinity.

It may be possible to improve the crystallinity and the surface morphology of

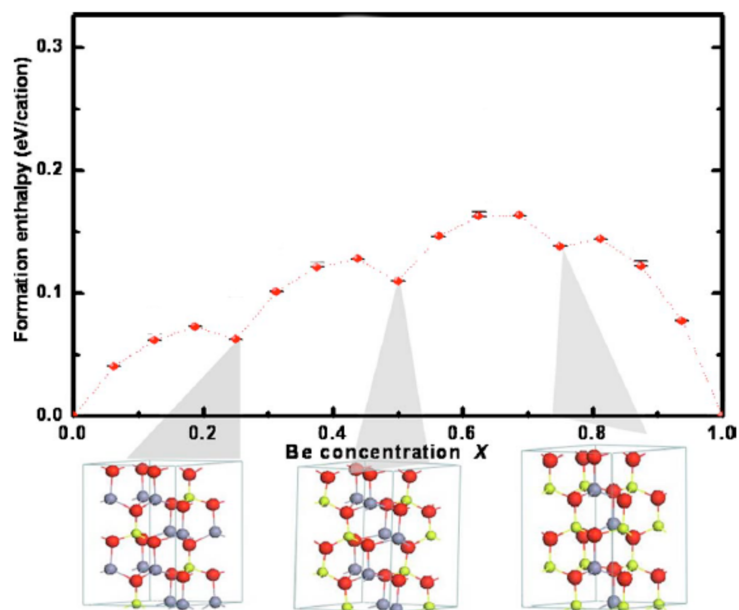

Figure 4.8: Formation enthalpy of $Be_xZn_{1-x}O$ as a function of the Be content x. The metastable $Be_xZn_{1-x}O$ structure are shown, corresponding to $x = 0.25$, $x = 0.50$ and $x = 0.75$ Be content.[20]

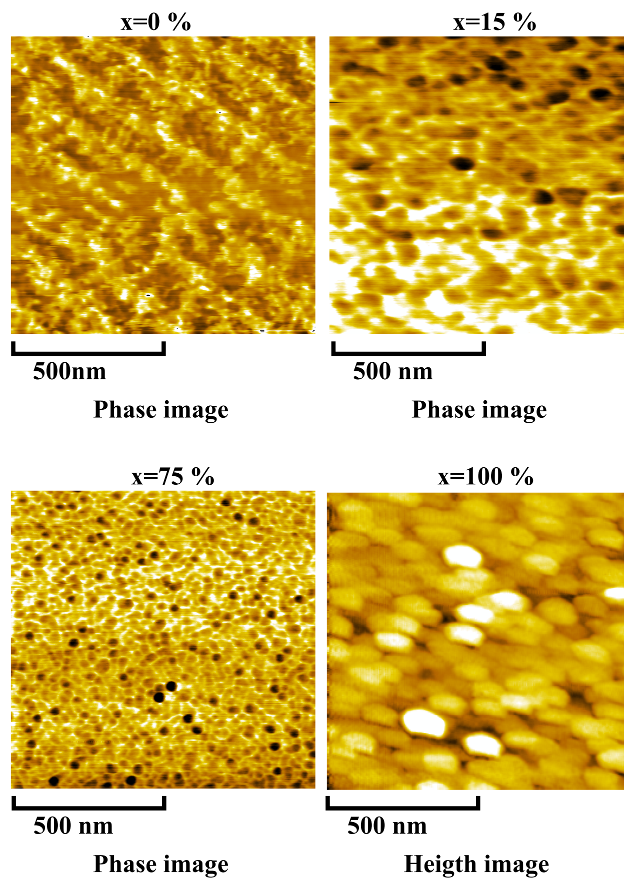

Figure 4.9: AFM images for different alloy film compositions.

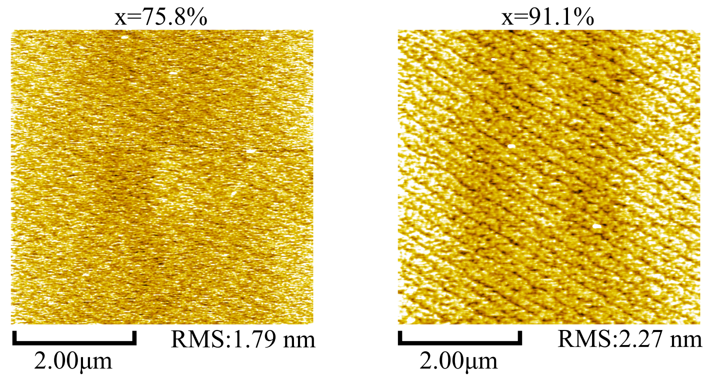

Figure 4.10: AFM images for thin films deposited using PLID. The root mean square roughness is shown. The thickness of both films is about 50 nm.

a film by using the temperature-modulation interval deposition technique, since in this deposition process, the surface is periodically heated and allowed to relax. The high-temperature period, usually lasting for a few minutes at 900°C, leads to longer surface diffusion length for adatoms. As shown by the AFM images in Figure 4.10, the experiment showed that the expectations are justified. The surface flatness is much better than for the film growth without temperature modulation. Indeed, a clean step-and-terrace surface morphology was observed. The terrace width is about 200 nm, which correspond to the sapphire terrace width. Grains are still observed on the terraces, but it appears that such surface islands are integrated into the bulk of the film, without inducing three-dimensional growth.

4.4 Band gap measurement

The transmission spectra of a ZnO film and $Be_{0.07}Zn_{0.93}O$ are shown in figure 4.11. A homogeneous and high crystal quality film was grown for ZnO film as a sharp transmission edge was observed. For the $Be_{0.07}Zn_{0.93}O$, a sharp transmission edge is observed between $T \approx 100\%$ and $T = 80\%$. After this edge, the transmission monotonically decreases to reach a value of $T \approx 60\%$ for a wavelength of 200 nm. The presence of a distribution of composition in the film may explain this broadening of the band edge.

Figure 4.12 shows the absorbance spectra for different Be content films plotted from a transmission measurement. A shift to higher band gap energy is observed

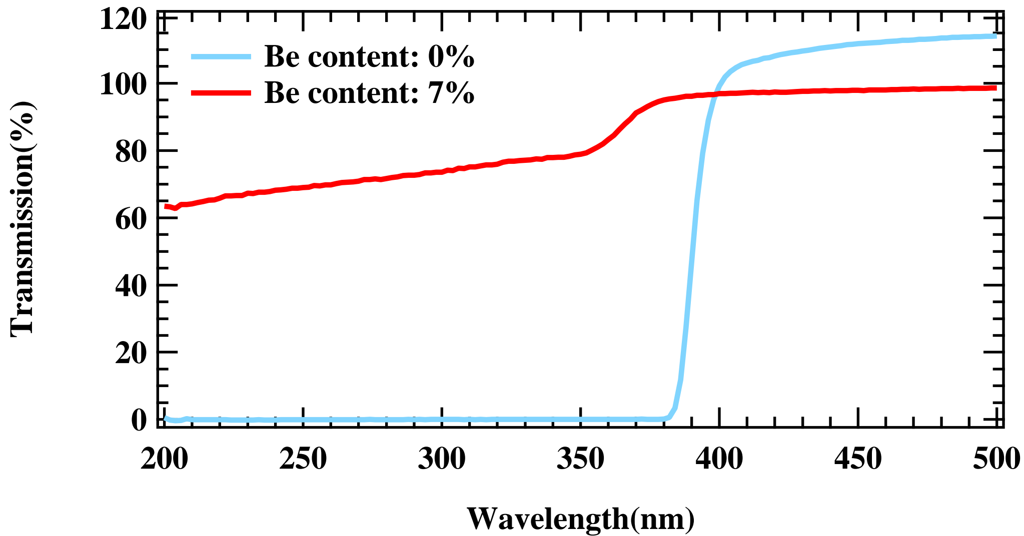

Figure 4.11: Transmission spectrum of a ZnO film and a $Be_{0.07}Zn_{0.93}O$ film.

as the Be concentration increases. As discussed in Section 2.4.2, the relation between $(\alpha h\nu)^2$ and energy is linear and the intersection with the horizontal axis at $y = 0$ gives the band gap energy. The linear relation is represented by the dark dashed lines. The transmission measurement was done for all the sample. However, for higher Be content the absorption edge developed multiple steps and broadened, making it impossible to obtain a reliable estimate for the band gap. The band edge for high Be content is located in the range $300 - 200$ nm. In this range, the high absorption of air makes the measurement even harder. Moreover, the film is acting as an anti-reflection coating for sapphire. The transmission signal is affected by all of these effects. The band-edge broadening appears to follow the loss of crystallinity in the highly-doped films. A distribution of band gap energies should appear if a distribution of c-axis parameters is observed by XRD.

Figure 4.13 shows the reflectivity behavior for three films with different Be content. The reflectivity maximum should occur close to the band gaps energy. Indeed, a systematic shift of the reflectivity maximum to higher energies does occur upon Be doping, as expected. However, a limitation appears for thin films. If the film is too thin, a substantial part of the measured intensity comes from the sapphire substrate. Therefore, it is necessary to grow thick enough films that absorb most of the incident light and eliminate the unwanted substrate reflection

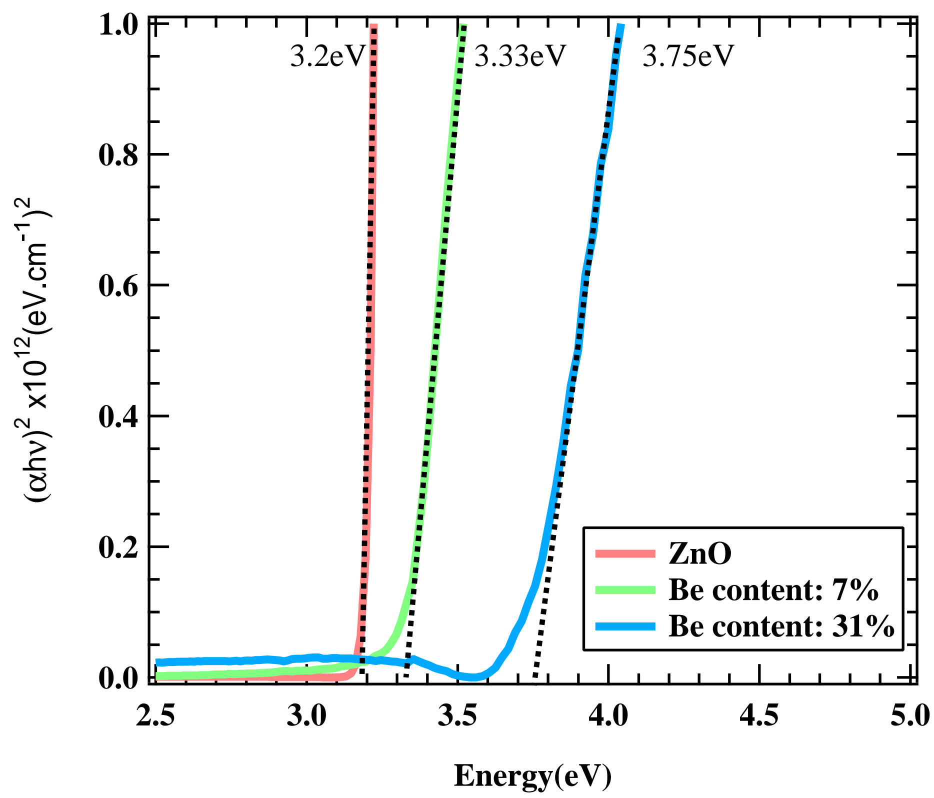

Figure 4.12: Graph of $(\alpha h\nu)^2$ versus the photon energy for several alloy films. The film thickness is about 15 nm.

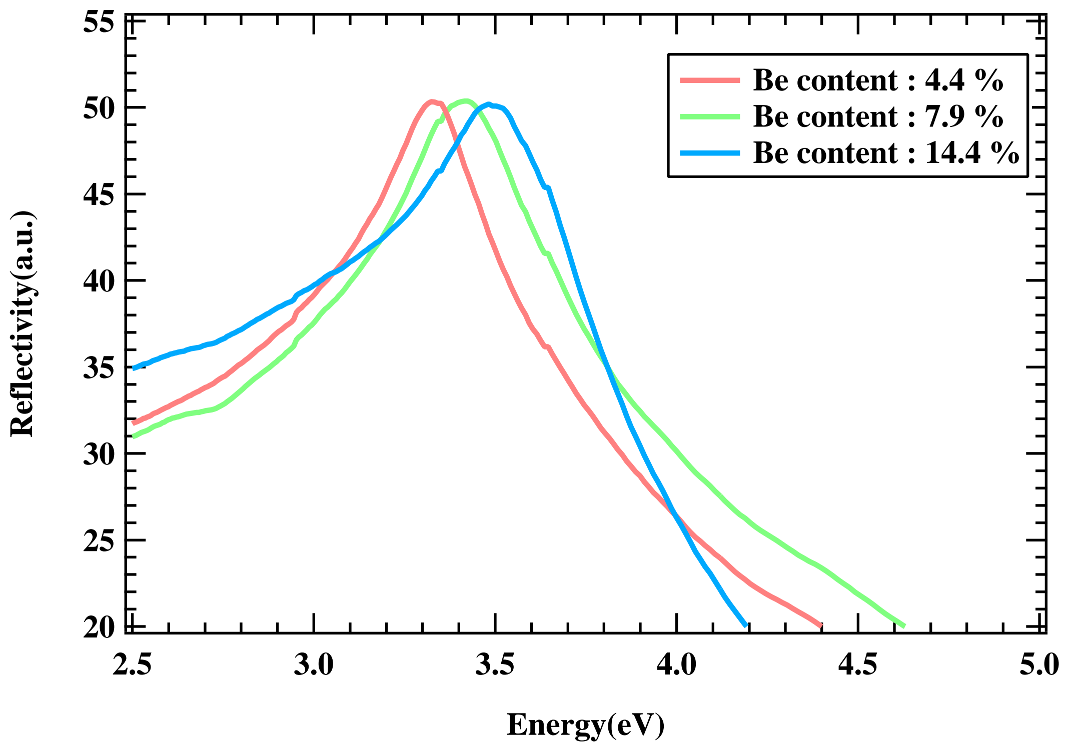

Figure 4.13: Plot of the BeZnO alloy film reflectivity as a function of photon energy for three different Be doping levels. A systematic bandgap shift to higher energies is observed with Be doping.

component.

An interesting point is to check the relation between the band gap energy found by the transmission measurement and the reflectivity measurement. Figure 4.14 presents the comparison between those two band gap energy determinations. The presence of a systematic shift was expected, but the deviation of the slope from unity was not. It indicates that the band gap calculations involve systematic errors on the order of 0.15 eV.

Figure 4.15 shows the evolution of the band gap energy determined from absorption measurements as a function of the Be content determined from the XRD peak positions. It show a constant increase of the band gap with the concentration. The Be doping dependence of the band gap width was fitted with a second-order polynomial. The bulk band gap value of 10.6 eV was used for pure BeO. It was

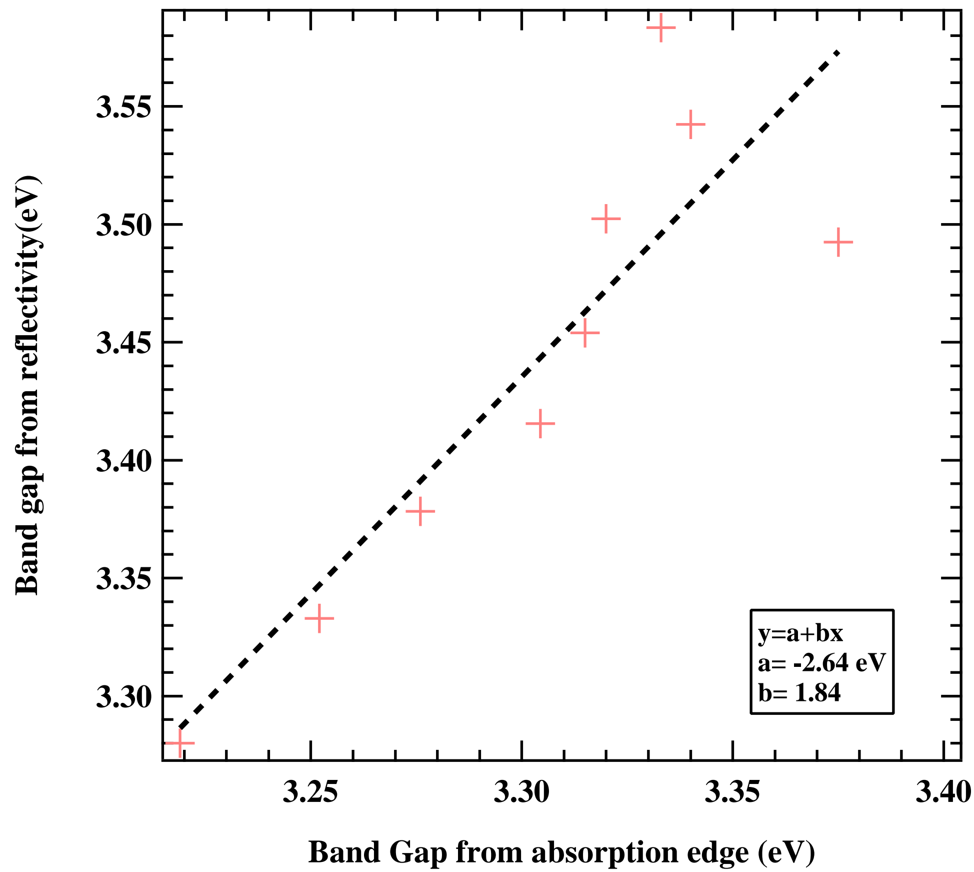

Figure 4.14: Comparison of band gaps determined from the reflectivity data versus transmission data. The dashed line is a linear fit.

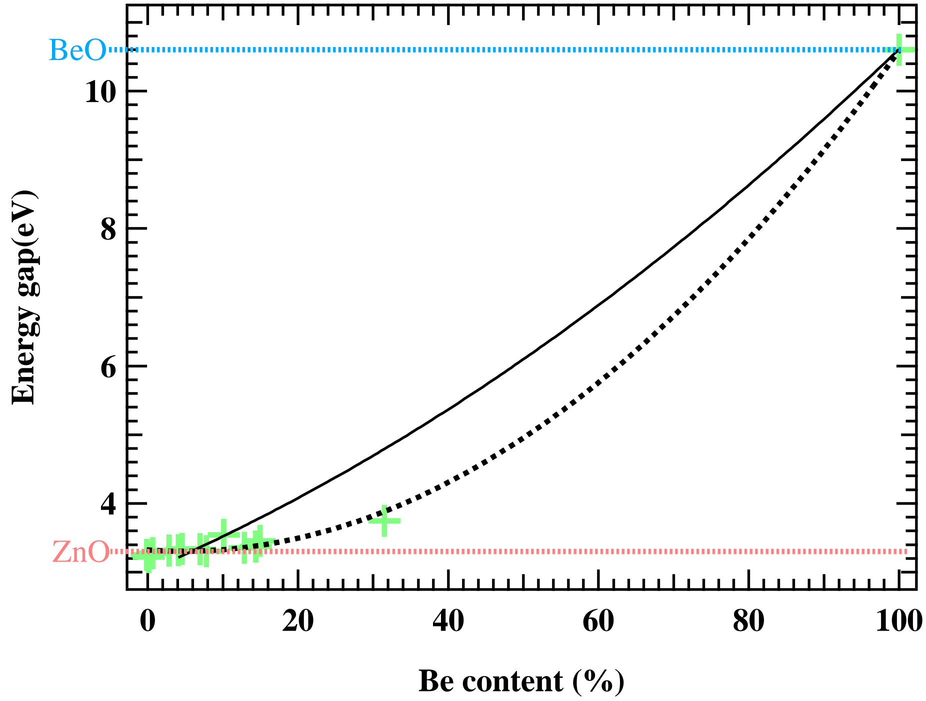

Figure 4.15: Plot of the band gaps calculated from the absorption spectra versus the Be content obtained from XRD peak positions. The quadratic fitting result is shown with a dashed line. The value of the pure BeO band gap is assumed to be 10.6 eV. The continuous line represents a fitting result obtained from the photocurrent data.

found that $E_{\mathrm{Be}_x\mathrm{Zn}_{1-x}\mathrm{O}} = E_{\mathrm{ZnO}}(1-x) + E_{\mathrm{BeO}}x + b(1-x)x$. The first two coefficients are the band gap energies of ZnO and BeO, respectively, while b is the bowing parameter. The fitting gave: $E_{\mathrm{ZnO}} = 3.32 \pm 0.04$, $E_{\mathrm{BeO}} = 10.6$, and $b = 8.01 \pm 0.39$. The bowing parameter value is larger than earlier published experimental reports[21] (4.5eV) and theoretical calculations[56] (5.6eV). However, the fitting from the band gap energy measured by photocurrent gives a different value. This error may rise from an uncertainty in the measurement of the Be content or the band gap energy.

Chapter 5

Band gap evolution and defects investigations

5.1 Introduction

The wavelength-dependent photoyield was measured for the BeZnO films. Strong photocurrent peaks were observed in comparison of the dark current for high Be content. The edge of the photoyield peaks was used to derived the energy of the band gap. The values were compared with reference data found in the literature. The response times of the BeZnO films were investigated and did not show strong variation with the Be content. The defect structure shows a distribution of defects between the Fermi level and the conduction band. Finally, thermally stimulated electron emission (TSEE) was observed in BeZnO thin films, similarly to the BeO films used in dosimeters.

5.2 Wavelength dependence of photocurrent

Figure 5.1 shows the photoyield for two $Be_xZn_{1-x}O$ samples with 7% and 14.4% Be content. The yields were normalized to the same maximum value. The transmission spectra of the two samples are also shown. A quantum efficiency increase is observed at a photon energy that corresponds to the band edge absorption. The absorbed photons generate enough photocarriers to be detected.

The photoyield is defined here as the number of electrons collected for one incident photon. The computed yield gives only a qualitative description of the behavior of the films as several geometric corrections were not taken into account. For instance, the incident photon flux is measured with a large-area photodiode from a low-intensity branch of the incident beam. The measured flux thus differs from the actual flux reaching the sample by a constant factor.

If the transit time of a photocarrier is assumed to be given by $T_R = L^2/V\mu$ where L is the distance between the electrodes, V the bias and μ the mobility of the photocarriers, the mobility of BeZnO can be estimated at about 6cm^{-2}/Vs.[23] Under a bias of 10 V, the minimum carrier lifetime detectable is about 1μs. If the lifetime is shorter than 1μs, the generated photocarriers recombine before being collected. It is probable that shorter lifetime carriers exist in the material.

Similarly to the results presented in Section 2.4.3, a maximum of the photocurrent was observed just above the absorption band edge. As the wavelength decreases, an increase of the recombination rate due to surface mechanisms reduces the photocurrent.

Figure 5.2 shows a shift of $\alpha \propto \ln((1 - I_{\text{photocurrent}})/I_{\text{max}})$. A shift to higher energy is observed for increasing Be content. A similar shift was observed in the

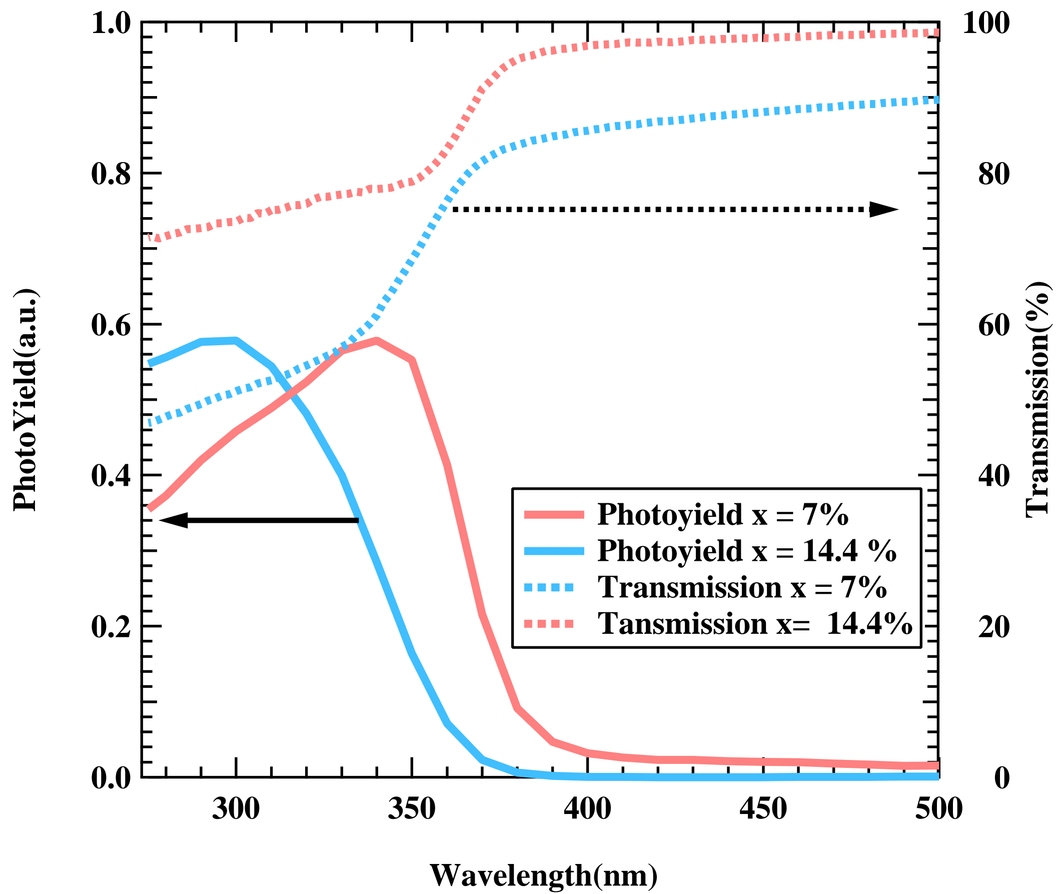

Figure 5.1: Photoyield as a function of wavelength for two alloy films. The absorption spectra of the same films are shown for comparison.

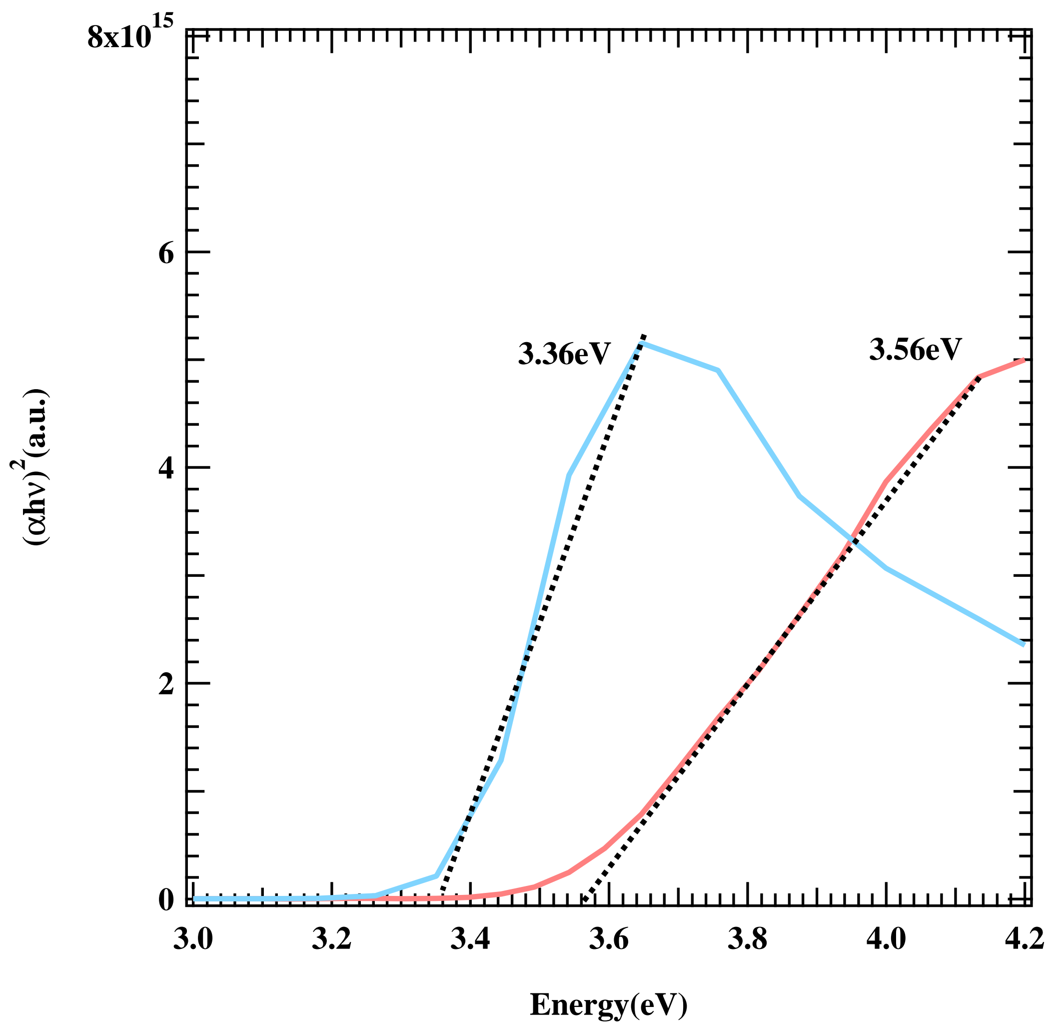

Figure 5.2: Absorbance estimated from the photocurrent as a function of the photon energy. The red curve is a 14% Be content thin film. The blue curve is a 7% Be content thin film. The dashed lines represents linear fits used to find the band gap energies.

transmission measurement. However, there is a discrepancy between the values.

Figure 5.3 shows the band gap energies determined from the photocurrent measurements. As before, the band gap of pure BeO was assumed to be 10.6 eV and the data was fitted with a quadratic function. The result of this analysis gave a smaller bowing parameter than the earlier absorption data analysis. A comparison of the bowing plots was shown in Figure 4.15. The bowing parameter b obtained from the photocurrent data was 2.86 ± 1 eV, which is smaller than the 8.01 eV obtained from the absorption data. The 2.86 eV bowing parameter is closer to the value usually observed in different alloy phases.[57]

In the case of BeO-ZnO alloys, strong bowing is expected because the bowing parameter should scale with the difference of the cell parameters of the two end compounds of an alloy.[58]. Several theories have been developed to predict the bowing parameters of alloy phases. Hill[59] has shown that the bowing parameter can be expressed as

$$b = \frac{Zer_{\text{BeZn}}}{4\pi\epsilon_0}(\frac{1}{R_{\text{Be}}} - \frac{1}{R_{\text{Zn}}})^2, \tag{5.1}$$

where Z is the valence number of the cations, e is the elementary charge, r_{BeZn} is the average covalent radius, and r_{Be} and r_{Zn} are the Pauling covalent radii. The valence number of the cations in wurtzite is about 2. In the case of BeZnO, the bowing calculated from this equation is 1.54 eV. The value is close to the experimental photoconductivity value.

The determination of the exact concentration of Be and an accurate measurement of the band gap are difficult. Table5.1 lists the large differences between reported values. The measurement of the band gap complicated mostly by the ambiguity in the definition of a bandgap in a system where the band edge overlaps with defect states. In such systems, the threshold energy for optical absorption differs from the threshold energy where macroscopic photocurrent is generated.

In the case of BeZnO, the actual substitutional Be content can be inaccurate due to the presence of interstitials or vacancies, strongly affecting the bowing value.

5.3 Defect distribution

5.3.1 Photocarrier lifetime

ZnO is a promising material for optoelectronic UV applications as it shows a strong photocurrent in the UV spectral range. The photocarrier density in ZnO

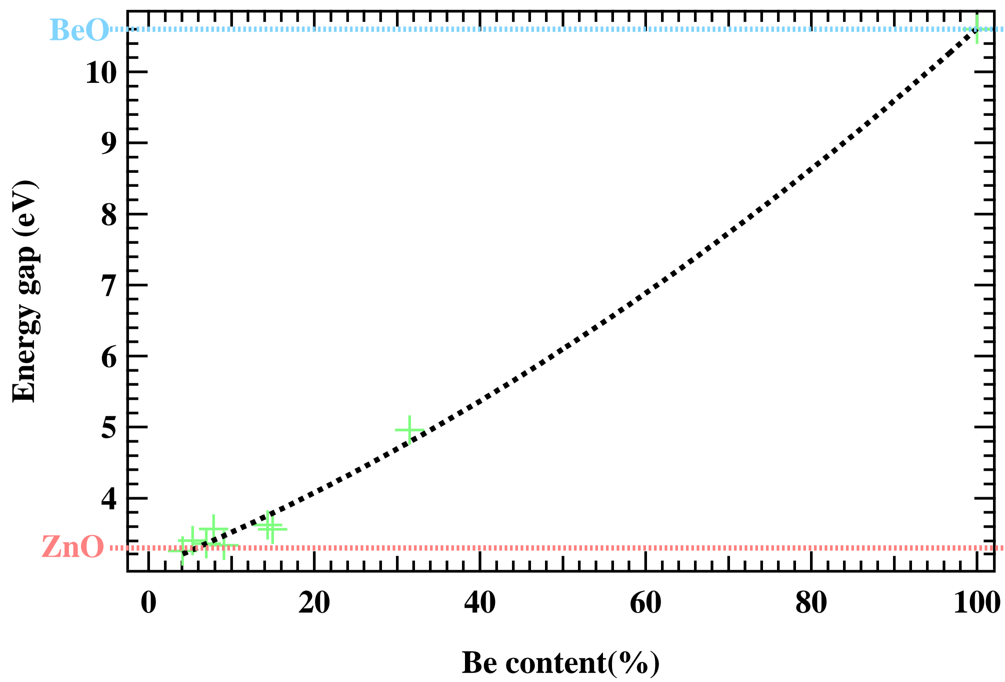

Figure 5.3: Band gap energies determined from photoconductivity data as a function of Be content. The BeO band gap value is assumed to be 10.6 eV. A quadratic bowing fit is shown with a black dotted line.

Bowing	Growth methods
3.98 [60]	Computation
4.5 [21]	RF co-sputtering
5.6 [56]	Computation
6.32 [17]	Hybrid Plasma-Assisted Molecular-Beam

Table 5.1: Reported bowing values for BeZnO and the growth technique.

is determined by several competing processes, each with a different characteristic response time. For example, a slow response component to light irradiation, on the scale of 100 seconds, has been reported for ZnO.[61] In dark conditions, the ZnO surface absorbs oxygen by trapping an electron: O_2(g) +e^- $\rightarrow$ $O_2^-(ad)$. If a hole-electron pair is generated by the absorption of a photon, the hole may be captured by the adsorbed oxygen resulting in oxygen desorption: h^+ + $O_2^-(ad) \rightarrow$ O_2(g). This slow process can also be observed in the BeZnO alloy films with a response time of several hundreds of seconds.

For UV light or particle detector applications, however, faster photocarrier relaxation processes are of prime interest. In ZnO the typical 'fast' photocarrier relaxation processes have characteristic times on the μs scale.[62]

The photocurrent observed in a $Be_{0.14}Zn_{0.86}O$ film is shown in Figure 5.4 as a function of the chopper frequency. The frequency dependence was measured at three different wavelengths to observe the change of recombination times in three different absorption regimes. For the 250 nm measurement, the photon energy is well above the band gap of the film, which means that most of the light is absorbed in a thin surface layer and the photocurrent is governed by surface recombination processes. At 340 nm, the system is insensitive to surface effects and the photocurent is dominated by volume recombination in the bulk of the film.

The frequency dependence curves were fitted with Equation 2.6 and two time constants were obtained. Table 5.2 presents the values of the time constants for the different wavelengths. The values of the time constants for 340 nm and 310 nm cases are similar. This indicates that the recombination process is still dominated by the volume of the film. However, for at 250 nm the two time constants start to show a slight increase, indicating that the surface mechanism is no longer negligible.

In comparison with ZnO, the response time were considerably slower. The response times can be expressed as: $t_{\text{Response}} \propto \frac{n_t}{n}\tau$ where n_t is the concentration of traps, n the concentration of photocarriers and τ is the lifetime of the photo-

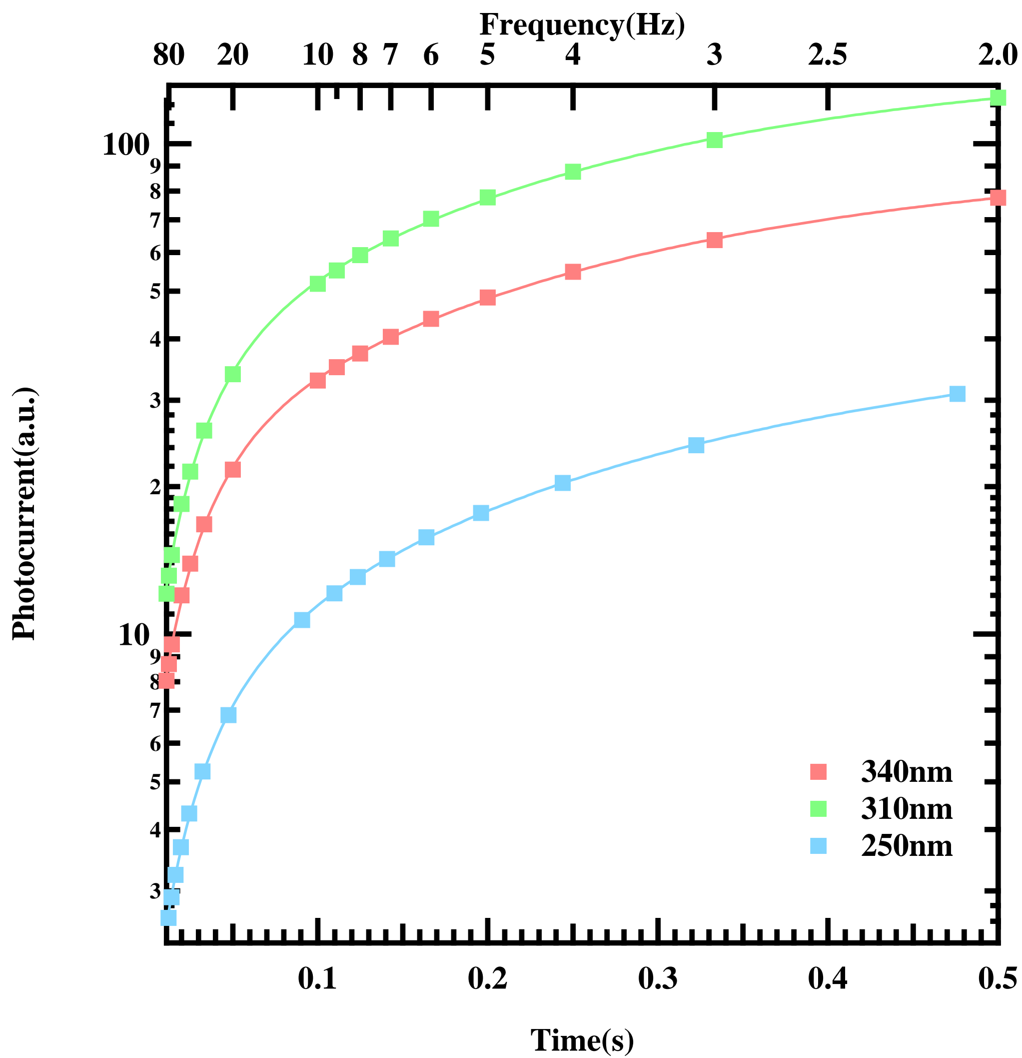

Figure 5.4: Plot of photocurrent as a function of the chopping frequency for a thin BeZnO film with a 14.4% Be content at three different measurement wavelengths.

Wavelength	τ_1	τ_1
340 nm	$14,8 \pm 1$ ms	121 ± 4 ms
310 nm	$14,7 \pm 1$ ms	117 ± 5 ms
250 nm	16.1 ± 1 ms	148 ± 5 ms

Table 5.2: Time constants for $Be_xZn_{1-x}O$ with $x = 14.4\%$

carriers. A longer photocarrier lifetime increases the response time. In the same way, an increase of trap concentration has a similar effect. It is difficult without measuring the concentration of the photocarriers to draw a conclusion. The carrier concentration and an effective photocarrier lifetime could be measured by a Hall-measurement under the light illumination and may give additional information.

No significant variation of the response was observed as a function of the Be-content. However, only the films with a Be-content under 30% were measurable with the available light source. A possible variation of the response time could appear in the Be-rich films.

5.3.2 Trap level distribution

Information regarding the distribution of trap levels in the band gap can be obtained from an analysis of the light intensity dependence of the photocurrent yield. A logarithmic plot of the photocurrent as a function of light attenuation is shown in Figure 5.5. By fitting this curve, it is possible to express the photocurrent as a function of light intensity $I \propto F^{\alpha}$ where F is the light intensity. The value of the exponential coefficient α was found to be 0.83 ± 0.02, corresponding to a sub-linear dependence. According to Rose,[35] this indicates that the in-gap recombination centers are filled with the majority photocarriers and implies the presence of an exponential distribution of defects between the Fermi level and the conduction band. A more detailed discussion was given in Section 2.4.3. From the model introduced earlier, a characteristic temperature can be derived: $T_1 = \alpha T/(1-\alpha)$, where T is the room temperature and α the exponential coefficient. It was found that for the BeZnO films, $T_1 = 1465$ K, which corresponds to an energy of 0.13 eV. It is commonly accepted [63] that in ZnO, Zn interstitials are shallow level donors. The observed trap energy scale appears to match the location of the shallow Zn interstitial defect level.

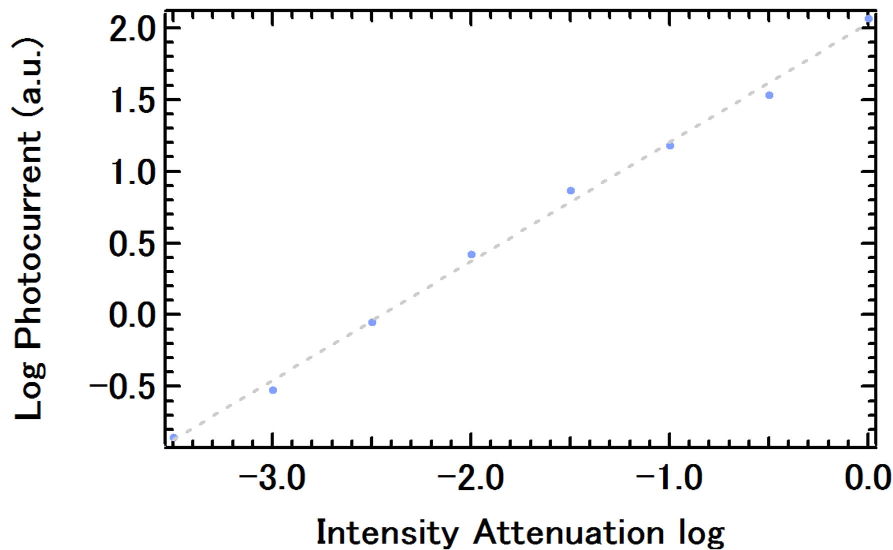

Figure 5.5: Plot of the logarithm of photocurrent as a function of the light attenuation for a BeZnO thin film with 14.4% Be content.

5.4 Temperature effect

The conductivity of a 4% Be-doped ZnO film was measured using the method described in Section 2.4.4. The room-temperature, before heating, the resistance of the film was about 10 MΩ. A current peak was observed at around $300°$C, followed by a strong decrease of current by several orders of magnitude. No recovery of conductivity was observed during cooling. Exposing the sample to short UV light at 248 nm did not recover the conductivity of the sample with the resistance remaining above 100 GΩ. The sample was exposed to a laboratory X-ray source, after which the high-temperature measurement was repeated. The X-ray exposure reduced the film resistance at room temperature to about 10 GΩ. The temperature dependence of the sample resistance was measured once again. Figure 5.6 shows the reappearance of the current peak at around $275°$C. During subsequent heating cycles, the peak was not observed, proving that the peak was caused by detrapping in a thermally-stimulated electron excitation process, demonstrating a basic dosimeter function in the BeZnO alloy films.

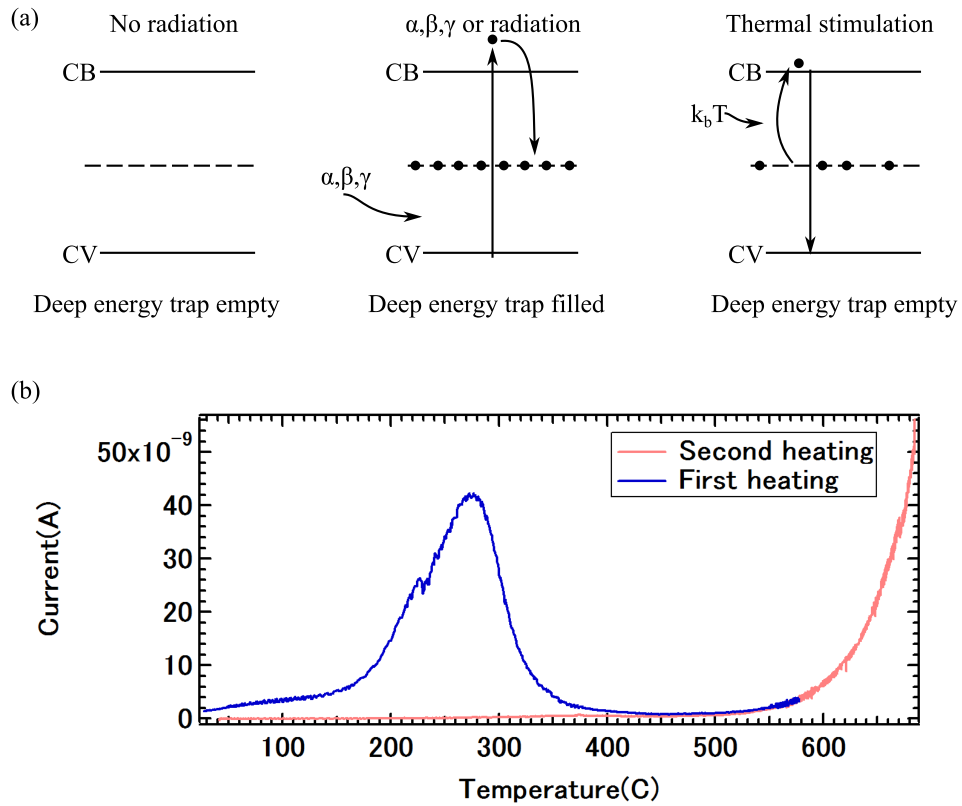

Figure 5.6: (a) Schematic of the electron trapping and TSEE. (b) The observed sample current under an applied bias of 15 V during two heating cycles after X-ray exposure.

Chapter 6

Conclusion

The possibility of deposition of BeO, a wide band gap semiconductor($E_g = 10.6$ eV), was demonstrated using Pulsed Laser Deposition. A phase diagram was drawn based on a set of film deposited in different oxygen pressures and substrate temperatures. A room-temperature crystalline phase, an amorphous phase, a high-quality crystal phase were observed. A bi-species ablation plume was measured by a time of flight measurement in the ablation plume. It shown the presence of Be metal, which may explained the absence of film growth at high temperature.

The alloying of BeO and ZnO was demonstrated on a substantial range of the composition. The relation between the expected Be content and the Be content determined by X-ray diffraction was discussed in relation with the crystal quality and the film morphology. The possibility band gap engineering has demonstrated for $Be_xZn_{1-x}O$ alloy films.

In the perspective of a detector application, the photoyield of $Be_xZn_{1-x}O$ was investigated.The photocurrent shown a wavelength dependence and sufficient intensity for device applications. Two time constants of about 10 ms and 100 ms for the photoyield were measured. The recombination process was attributed to the interstitial shallow donors close from the conduction band.

This master research was indisputably a step forward in the research of material for extreme conditions. It opens outstanding perspective for the application of beryllium based semiconductor and confirms the growing interest of using small size atoms for materials tuning.

Acknowledgment

I would like to express my deepest appreciation to all those who provided me the possibility to complete this Master's Degree. A special gratitude I give to my professor, Mr. Lippmaa, whose contribution in stimulating suggestions and encouragement, helped me to coordinate my research especially in writing this report. Furthermore, I am grateful to my parents and Michelle for their endless love and support. I would like to thank Dr. Matvejeff for his interesting suggestions. I would like to thank Dr. Takahashi for his help for the pyroelectric measurement. I am also grateful to Ms. Kawamura who helped me for the administrative part. I would also like to acknowledge with much appreciation the crucial role of the staff of ISSP, who gave the permission to use all required equipment and the necessary machines to complete my measurements. Last but not least, I would like to thank again my supervisor Professor Mikk Lippmaa for the support during my master's degree.

List of figures

List of Figures

1.1 Rate of energy loss 7
1.2 Structure of wurtzite BeO. Red atoms are oxygens. Beryllium atoms are shown in green. 9
1.3 Band gap structure and density of states of BeO.[13] 11
1.4 Band structure of ZnO.[14] 12
1.5 Schematic MOS structures with oxygen diffusion barriers.[15] . . 12
1.6 Evolution of the band gap as a function of beryllium content in $Be_xZn_{1-x}O$.[17] 14
1.7 Substitutional alloying of BeO and ZnO assuming that the wurtzite structure is maintained. 15

2.1 Schematic diagram of the micro-PLD chamber. 20
2.2 AFM image of an annealed sapphire 22
2.3 (a)Picture of the double target holder composed of one BeO part and one ZnO part. (b) Schematic view of the ablation for each target part. 24
2.4 Deposition methods 26
2.5 (a)Schematic view of the sample holder use for film growth. (b) Photo of the sample holder, showing the outer ring of the sample holder, the thermally isolate nickel block in the center, and a substrate crystal held in place with two stainless steel wires. . . . 27
2.6 Schematic view of 2θ scan 28
2.7 Schematic view of Dektak 30
2.8 Schematic view of an AFM measurement. 31
2.9 Time-of-flight plume analysis diagram. 32
2.10 Pyroelectric measurement set up: the film is periodically heated by a chopped laser beam. The current generated by the temperature step is measure between the Pd top electrode and the conducting substrate. 33

2.11 Transmission and absorption measurements. 37
2.12 Excitation of electrons in a semiconductor or an insulator. 38
2.13 Photocurrent evolution as a function of the photon energy. 39
2.14 Schematic view of the photocurrent measurement setup for wavelength dependence 40
2.15 Photon flux as a function of wavelength. 41
2.16 Defect distribution leading to a sublinear light intensity dependence. 43
2.17 Schematic view of the photocurrent measurement for chopping rate analysis. 44
2.18 Schematic view of the high-temperature probe and setup. 45
2.19 Resistance of a sapphire substrate as a function of temperature. . . 46

3.1 $\theta/2\theta$-scan of an optimal BeO film 50
3.2 $\theta/2\theta$ scan of a BeO film deposited at 10^{-6} Torr and room temperature. (*) indicates the sapphire (006) substrate peak. The dashed line marks the expected BeO bulk diffraction peak position. 51
3.3 Overview of BeO XRD-scan 52
3.4 Φ scan of a BeO thin film grown on sapphire. 53
3.5 Relative in-plane orientation of the BeO thin film on a sapphire surface. Oxygen atoms are shown in red, beryllium in green, and aluminum in blue. 54
3.6 Diffraction pattern of a BeO film deposited on a Nb:$SrTiO_3$ (111) substrate. The Nb:$SrTiO_3$ (111)reflection is marked by (*). 55
3.7 ϕ-scan of a BeO film deposited on a Nb:$SrTiO_3$(111) substrate. . . 56
3.8 Relative in-plane orientation of the BeO thin film on a $SrTiO_3$(111) surface. 57
3.9 Pole figure of a bare sapphire substrate for $2\theta = 84.4$. The assigned reflections of sapphire are shown. 58
3.10 AFM image of a BeO thin film. The image size is $3\mu m \times 3\mu m$. . . 59
3.11 Growth rate of BeO thin films as a function of temperature for growth on sapphire substrates at various ambient oxygen pressures. 60
3.12 Time-of-flight spectrum of the ionized species in the ablation plume of a BeO target. The inset shows the overlap between consecutive ablation spots on the target surface when the target x-y scanning speed is too low. 61
3.13 TOF measurement of selected laser shots fired on the same spot on the target 62

3.14 Ratio of Be and BeO species in the ablation plume for various ambient oxygen pressures. 63
3.15 Growth stability diagram of BeO thin film growth on sapphire. . . 65
3.16 Pyroelectric response measurement obtained at a laser chopping rate of 2 Hz. 67
3.17 A C-V curve of a BeO film and the loss tangent, measured at 600 Hz 68
3.18 IV curve of BeO film. 69

4.1 Correlation between the expected Be content calculated from the growth rates and the Be content obtained from Vegard's law analysis of the x-ray diffraction peak positions for two different growth methods. The inset shows an enlarged view of the low Be content range of up to 10%. Data for thin films grown by PLD without temperature modulation are marked with blue crosses. The red crosses correspond to films grown by the temperature modulation technique. The expected behavior is represented by the dashed lines. 74
4.2 XRD patterns for $Be_xZn_{1-x}O$. The peak positions of BeO(002) and ZnO(002) are shown for reference. 77
4.3 Contour plot of the XRD intensity of the $Be_xZn_{1-x}O$ (002) peak. The dashed line indicates the expected peak position according to Vegard's law. 78
4.4 Evolution of the $Be_xZn_{1-x}O$ (002) peak width with the Be content. The dashed lines are guides for the eye. PLD refers to films grown at a constant temperature. PLID refers to films grown by the temperature modulation technique. 79
4.5 An XRD pattern of an alloy film deposited by temperature-modulated PLD $300°$/$900°$ at 1 mTorr for an expected concentration of $x = 19.1\%$. (*) marks the sapphire (006) peak. 80
4.6 Evolution of substitutional and interstitial site occupancies and an illustration of the various defect sites. 82
4.7 Width of the $Be_xZn_{1-x}O$ (002) peak as a function of the expected concentration, showing a possible stability region close to 7% Be doping. 83
4.8 Formation enthalpy of $Be_xZn_{1-x}O$ as a function of the Be content x. The metastable $Be_xZn_{1-x}O$ structure are shown, corresponding to $x = 0.25$, $x = 0.50$ and $x = 0.75$ Be content.[20] 84
4.9 AFM images for different alloy film compositions. 85

4.10 AFM images for thin films deposited using PLID. The root mean square roughness is shown. The thickness of both films is about 50 nm. 86
4.11 Transmission spectrum of a ZnO film and a $Be_{0.07}Zn_{0.93}O$ film. . . 87
4.12 Graph of $(\alpha h\nu)^2$ versus the photon energy for several alloy films. The film thickness is about 15 nm. 88
4.13 Plot of the BeZnO alloy film reflectivity as a function of photon energy for three different Be doping levels. A systematic bandgap shift to higher energies is observed with Be doping. 89
4.14 Comparison of band gaps determined from the reflectivity data versus transmission data. The dashed line is a linear fit. 90
4.15 Plot of the band gaps calculated from the absorption spectra versus the Be content obtained from XRD peak positions. The quadratic fitting result is shown with a dashed line. The value of the pure BeO band gap is assumed to be 10.6 eV. The continuous line represents a fitting result obtained from the photocurrent data. 91

5.1 Photoyield as a function of wavelength for two alloy films. The absorption spectra of the same films are shown for comparison. . . 94
5.2 Absorbance estimated from the photocurrent as a function of the photon energy. The red curve is a 14% Be content thin film. The blue curve is a 7% Be content thin film. The dashed lines represents linear fits used to find the band gap energies. 95
5.3 Band gap energies determined from photoconductivity data as a function of Be content. The BeO band gap value is assumed to be 10.6 eV. A quadratic bowing fit is shown with a black dotted line. . 97
5.4 Plot of photocurrent as a function of the chopping frequency for a thin BeZnO film with a 14.4% Be content at three different measurement wavelengths. 99
5.5 Plot of the logarithm of photocurrent as a function of the light attenuation for a BeZnO thin film with 14.4% Be content. 101
5.6 (a) Schematic of the electron trapping and TSEE. (b) The observed sample current under an applied bias of 15 V during two heating cycles after X-ray exposure. 102

Bibliography

[1] H. Okumura. Present status and future prospect of wide gap semiconductor high-power devices. *Japanese Journal of Applied Physics*, 45:7565, 2006.

[2] W.H. McMaster, N. Kerr Del Grande, Mallett J.H., and J.H. Hubbell. *Compilation of X-ray cross sections*. Lawrence Livermore National Laboratory, 1969.

[3] C. Kittel. *Introduction to Soli State Physics*. Wiley, 1953.

[4] G. Lutz. *Semiconductor Radiation Detectors*. Springer, 1999.

[5] C.A. Klein. Bandgap dependence and related features of radiation ionization energies in semiconductors. *Journal of Applied physics*, 39:2029, 1968.

[6] R.D. Ryan. Precision measurements of the ionization energy and its temperature variation in high purity silicon radiation detectors. *Nuclear Science*, 20:473, 1973.

[7] M. Gabrysch. *Electronic Properties of Diamond*. PhD thesis, Uppsala university, 2008.

[8] Dirk Schalch, Arthur Scharmann, and Albrecht Weis. Characterization of reactively sputtered BeO films. *Thin Solid Films*, 124(3-4):351 – 358, 1985.

[9] Haruyuki Endo, Tetsuya Chiba, Kazuyuki Meguro, Kyo Takahashi, Mitsuru Fujisawa, Shigeaki Sugimura, Shinya Narita, Yasube Kashiwaba, and Eiichi Sato. Fabrication and characterization of a ZnO x-ray sensor using a high-resistivity ZnO single crystal grown by the hydrothermal method. *Nuclear Instruments and Methods in Physics Research Section A: Accelerators, Spectrometers, Detectors and Associated Equipment*, 665(0):15 – 18, 2011.

[10] D M Roessler and W C Walker. Electronic spectrum of crystalline beryllium oxide. *Journal of Physical Chemistry Solids*, 30:157–167, 1969.

[11] E O Wrasse and R J Baierle. First principles study of native defects in BeO. *Physics Procedia*, 28:79–83, 2012.

[12] G.G. Bentle. Elastic constants of single crystal BeO at room temperature. *Journal of the American Ceramic Society*, 49:125–128, 1966.

[13] S. Duman, A. Sutlu, S. Bagci, H. M. Tutuncu, and G. P. Srivastava. Structural, elastic, electronic, and phonon properties of zinc-blende and wurtzite BeO. *Journal of Applied Physics*, 105(3):033719, 2009.

[14] Paul Erhart, Karsten Albe, and Andreas Klein. First-principles study of intrinsic point defects in ZnO: Role of band structure, volume relaxation, and finite-size effects. *Phys. Rev. B*, 73:205203, May 2006.

[15] J H Yum, G Bersuker, and T Akyol. Epitaxial ALD BeO: Efficient oxygen diffusion barrier for EOT scaling and reliability improvement. *Transactions on Electron Devices*, 58(12):4384, 2011.

[16] J. C. PHILLIPS. Ionicity of the chemical bond in crystals. *Rev. Mod. Phys.*, 42:317–356, Jul 1970.

[17] T.S. Jeong, J.H. Kim kin, D.S. Park, J.H. Yu, T.S. Kim, and C.J. Youn. Bandgap modulation of BeZnO layers grown by using hybrid plasma-assisted molecular-beam epitaxy/electron-beam deposition. *Journal of the Korean Physical Society*, 55(6):2548–2551, 2009.

[18] Atsushi Tsukazaki, Masashi Kubota, Akira Ohtomo, Takeyoshi Onuma, Keita Ohtani, Hideo Ohno, Shigefusa F. Chichibu, and Masashi Kawasaki. Blue light-emitting diode based on ZnO. *Japanese Journal of Applied Physics*, 44(21):L643–L645, 2005.

[19] Y.R. Ryu, T.S. Lee Lee, and al. Wide-band gap oxide alloy: BeZnO. *Applied Physics Letters*, 88(5):052103, 2006.

[20] X. F. Fan, Z. Zhu, Y.S. Ong, Y. M. Lu, Z. X. Shen, and J.L. Kuo. A direct first principles study on the structure and electronic properties of $Be_xZn_{1-x}O$. *Applied Physics Letters*, 91(12):121121, 2007.

[21] J.H. Yu, D.S. Park, J.H. Kim, T.S. Jeong, C.J. Youn, and K.J. Hong. Post-growth annealing and wide bandgap modulation of BeZnO layers grown by RF co-sputtering of ZnO and Be targets. *Journal of Materials Science*, 45(1):130–135, 2010.

[22] J. M. Khoshman, D. C. Ingram, and M. E. Kordesch. Bandgap engineering in amorphous Be_xZn_yO thin films. *Applied Physics Letters*, 92(9):091902, 2008.

[23] Mingming Chen, Yuan Zhu, Longxing Su, Quanlin Zhang, Rong Xiang, Xuchun Gui, Tianzhun Wu, Xingzhong Cao, Peng Zhang, Baoyi Wang, and Zikang Tang. Suppression of oxygen vacancies in Be alloyed ZnO. *Journal of Alloys and Compounds*, 577(0):179 – 182, 2013.

[24] Young-Il Kim and Ram Seshadri. Optical properties of cation-substituted zinc oxide. *Inorganic Chemistry*, 47(19):8437–8443, 2008. PMID: 18821810.

[25] S. Strite and H. Morkoc. GaN, AlN, and InN: A review. *Journal of Vacuum Science and Technology B: Microelectronics and Nanometer Structures*, 10(4):1237–1266, 1992.

[26] D. G. Schlom and L. N. Pfeiffer. Oxide electronics: Upward mobility rocks! *Nature materials*, 9:881–883, 2010.

[27] William C. Johnson and C. S. Chiang. Phase equilibrium and stability of elastically stressed heteroepitaxial thin films. *Journal of Applied Physics*, 64(3):1155–1165, 1988.

[28] M. Yoshimoto, T. Maeda, T. Ohnishi, and al. Atomicscale formation of ultra-smooth surfaces on sapphire substrate for high quality thin film fabrication. *Applied Physics Letters*, 67:2615, 1995.

[29] P.Y. Yu and M. Cardona. *Fundamentals of semiconductors*. Springer, third edition edition, 2003.

[30] T. Feng. Anomalous photoelectronic in $SrTiO_3$. *Physical Review B*, 25:627, 1982.

[31] H.B. DeVore. Spectral distribution of photoconductivity. *Physical Review*, 102:86, 1956.

[32] S.M. Ryvkin. Ryvkin. *Soviet Physics*, 20:139, 1950.

[33] E. Lopez-Curz, J. Gonzalez-Hermandez, D.D. Allred, and W.P. Allre. Photoconductive characterization of $Zn_xCd_{1-x}Te(0 \leq x \leq 0.25)$ single crystal alloys. *Journal of Vacuum Science and Technology A*, 8:1934, 1990.

[34] D.D. Eley, S. Kinnear, and M.R. Willis. Lifetime of photogenerated carriers in TCNQ single crystals. *Physica Status Solidi B*, 108:1981, 1981.

[35] A. Rose. *Concepts in Photoconductivity and Allied Problems*. Interscience Publishers, 1963.

[36] Sumiaki Ibuki and Seiichi Yoshimatsu. Photoconductivity of stibnite (sb_2s_3). *Journal of the Physical Society of Japan*, 10(7):549–554, 1955.

[37] J. Lesz, A. Scharmann, and G. Holzapfel. TL Signals from BeO Thin-Film TSEE dosemeters. *Japanese Journal of Applied Physics*, 24S4(Supplement 24-4):254–256, 1985.

[38] A. Sasaki, W. Hara, and al. Buffer-enhanced room-temperature growthand characterization of epitaxial ZnO thin films. *Applied Physics Letters*, 86, 2005.

[39] J.P. hong, S.B. Lee, and al. Room temperature formation of half-metallic Fe_3O_4 thin films for the application of spintronic devices. *Applied Physics Letters*, 83:1590–1592, 2003.

[40] M. Tachiki, T. Hosomi, and Kobayashi T. Room-temperature heteroepitaxial growth of NiO thin films using pulsed laser deposition. *Japan Journal Applied Physics*, 39:1817–1820, 2000.

[41] Atsushi Kobayashi, Satoshi Kawano, Yuji Kawaguchi, Jitsuo Ohta, and Hiroshi Fujioka. Room temperature epitaxial growth of m-plane GaN on lattice-matched ZnO substrates. *Applied Physics Letters*, 90(4):041908, 2007.

[42] Toshinori Takagi, Kakuei Matsubara, and Hiroshi Takaoka. Optical and thermal properties of BeO thin films prepared by reactive ionized-cluster beam technique. *Journal of Applied Physics*, 51(10):5419–5424, 1980.

[43] L. Vegard. Die konstitution der mischkristalle und die raumfullung der atome. *Zeitschrift fur Physik*, 5, 1921.

[44] Masatomo Yashima, Nobuo Ishizawa, and Masahiro Yoshimura. Application of an ion-packing model based on defect clusters to zirconia solid solutions: II, applicability of vegard's law. *Journal of the American Ceramic Society*, 75(6):1550–1557, 1992.

[45] W Li, M. Pessa, and J. Likonen. Lattice parameter in GaNAs epilayers on gaas: Deviation from vegard's law. *Applied Physics Letters*, 78(19):2864–2866, 2001.

[46] H. Takagi, T. Ido, S. Ishibashi, M. Uota, S. Uchida, and Y. Tokura. Superconductor-to-nonsuperconductor transition in $(\mathrm{la}_{1-\mathrm{x}}\mathrm{sr}_{\mathrm{x}})_2\mathrm{cuo}_4$ as investigated by transport and magnetic measurements. *Phys. Rev. B*, 40:2254–2261, Aug 1989.

[47] Longxing Su, Yuan Zhu, Quanlin Zhang, Mingming Chen, Tianzhun Wu, Xuchun Gui, Bicai Pan, Rong Xiang, and Zikang Tang. Structure and optical properties of ternary alloy BeZnO and quaternary alloy BeMgZnO films growth by molecular beam epitaxy. *Applied Surface Science*, 274(0):341 – 344, 2013.

[48] K.A. Gschneidner and G.H. Vimeyard. Departures from vegard's law. *Journal of Applied Physics*, 33:3444, December 1962.

[49] G. Fournet. A study of vegard's law. *Journal de physique et le Radium*, 14:374, 1953.

[50] S. Mader. Metastable alloy films. *Journal of Vacuum Science and Technology*, 2(1):35–41, 1965.

[51] Tossell. Calculation of bond distances and heats of formations for BeO, MgO, SiO_2, TiO_2, FeO and ZnO using the ionic model. *American mineralogist*, 65:163 – 173, 1980.

[52] D.R. Stull and H. Prophet. *JANAF Thermochemical Tables*. NIST, 2nd edition, 1970.

[53] F.T. Kong and H.R. Gong. Influence of interstitial beryllium on properties of ZnO: A first-principle research. *Computational Materials Science*, 61(0):127 – 133, 2012.

[54] M. V. Yakushev, A. N. Varaksin, I. N. Ogorodnikov, and A. V. Kruzhalov. A rutherford backscattering spectrometry study of Zn implanted BeO single crystals. *Radiation Effects and Defects in Solids*, 150(1-4):157–160, 1999.

[55] Masahiro Sanmyo, Yasumasa Tomita, and Kenkichiro Kobayashi. Preparation of zinc oxide films containing Be and N atoms by radio frequency magnetron sputtering. *Thin Solid Films*, 472(1-2):189 – 194, 2005.

[56] S.F. Ding, G.H. Fan, S.T. Li, K. Chen, and B. Xiao. Theoretical study of alloys. *Physica B: Condensed Matter*, 394(1):127 – 131, 2007.

[57] I. Vurgaftman, J. R. Meyer, and L. R. Ram-Mohan. Band parameters for III–V compound semiconductors and their alloys. *Journal of Applied Physics*, 89(11):5815–5875, 2001.

[58] T.H. Glisson, J.R. Hauser, M.A. Littlejohn, and C.K. Williams. Energy bandgap and lattice constant contours of III-V quaternary alloys. *Journal of Electronic Materials*, 7(1):1–16, 1978.

[59] R Hill. Energy-gap variations in semiconductor alloys. *Journal of Physics C: Solid State Physics*, 7(3):521, 1974.

[60] Yifeng Duan, Hongliang Shi, and Lixia Qin. Elasticity, band structure, and piezoelectricity of $Be_xZn_{1-x}O$ alloys. *Physics Letters A*, 372(16):2930 – 2933, 2008.

[61] Yasutaka Takahashi, Masaaki Kanamori, Akiko Kondoh, Hideki Minoura, and Yutaka Ohya. Photoconductivity of ultrathin zinc oxide films. *Japanese Journal of Applied Physics*, 33(Part 1, No. 12A):6611–6615, 1994.

[62] Y. Liu, C.R. Gorla, S. Liang, N. Emanetoglu, Y. Lu, H. Shen, and M. Wraback. Ultraviolet detectors based on epitaxial ZnO films grown by MOCVD. *Journal of Electronic Materials*, 29(1):69–74, 2000.

[63] F. Oba, M. Choi, A. Togo, and I. Tanaka. Point defects in zno: an approach from first principles. *Science and Technology of Advanced Materials*, 12, 2011.